



FEDERAL UNIVERSITY OF RIO GRANDE DO NORTE  
TECHNOLOGY CENTER  
GRADUATE PROGRAM IN ELECTRICAL AND COMPUTER  
ENGINEERING



# Wavelet-based Protection Assessment of the Doubly-fed Induction Generator

**Max Rodrigues Marques**

Advisor: Prof. Dr. Flavio Bezerra Costa

**M.Sc Dissertation** presented to the Graduate Program in Electrical and Computer Engineering at UFRN (area of concentration: Automation and Systems) as part of the requirements for obtain the Master of Science degree.

Serial number PPgEEC: M547  
Natal, RN, January 28th, 2019

Universidade Federal do Rio Grande do Norte - UFRN  
Sistemas de Bibliotecas - SISBI  
Catalogação de publicação na fonte. UFRN - Biblioteca Central Zila Mamede

Marques, Max Rodrigues.

Wavelet-based protection assessment of the doubly-fed induction generator /  
Max Rodrigues Marques. - 2019.  
108 f.: il.

Dissertação (mestrado) - Universidade Federal do Rio Grande do Norte, Centro de Tecnologia, Programa de Pós-Graduação em Engenharia Elétrica e de Computação. Natal, RN, 2019.

Orientador: Prof. Dr. Flavio Bezerra Costa

1. Doubly-fed induction machine - Dissertação. 2. Generator protections - Dissertação. 3. Wavelet transform - Dissertação. I. Costa, Flavio Bezerra II. Título.

RN/UF/BCZM

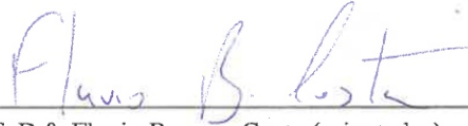
CDU 621.313.332

Elaborado por Ana Cristina Cavalcanti Tinôco - CRB-15/262

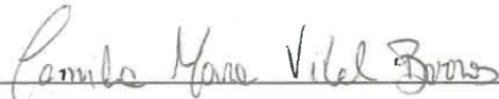
# Wavelet-based Protection Assessment of the Doubly-fed Induction Generator

**Max Rodrigues Marques**

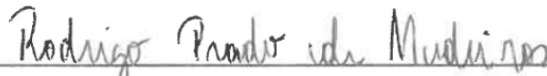
Master dissertation approved on January 28, 2019, by the examining board composed of the following members: pelos seguintes membros:



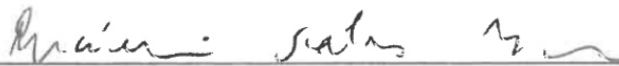
Prof. Dr<sup>o</sup>. Flavio Bezerra Costa (orientador) ..... UFRN



Prof. Dr<sup>a</sup>. Camila Mara Vital Barros ..... UFPB



Prof. Dr<sup>o</sup>. Rodrigo Prado de Medeiros ..... UFRSA



Prof<sup>a</sup> Dr<sup>o</sup>. Luciano Sales Barros ..... UFRN



Prof<sup>a</sup> Dr<sup>o</sup>. Thiago de Oliveira Alves Rocha ..... UFRN

*'Life is like riding a bicycle. To keep  
your balance, you must keep  
moving.'*  
*(Albert Einstein)*

---

# Acknowledgment

---

To God in the first place for this opportunity.

To my parents, Solange Rodrigues and Valdecy Marques, who give me all the support to keep on forward.

To my advisor professor Dr. Flavio Bezerra Costa for the guidance, advising and support in the making of this dissertation.

To my colleagues of the ProRedes research group, Marcos Sérgio, Mônica Leal, Jéssika Fonseca, Frankelene Pinheiro, Rafael Lucas, and Igor Prado for all the assistance provided for this dissertation construction, and to all my friends and girlfriend which stayed with me during all this process giving me the necessary support.

To the Coordination for the Improvement of Higher Education Personnel (CAPES) and the National Council for Scientific and Technological Development (CNPq) due to the financial support.

---

# Resumo

---

Com o aumento da globalização e da demanda energética mundial, tem-se buscado garantir a sustentabilidade devido à crescente preocupação de preservar o planeta para gerações futuras. Portanto, investimentos em fontes de energia limpas e renováveis, como a geração eólica, ganharam espaço nos grupos de pesquisas e na indústria em busca de superar as desvantagens e aprimorar os benefícios. O gerador de indução duplamente alimentado (DFIG) é o predominante no mercado da energia eólica. Contudo, considerando as falhas elétricas inerentes a este tipo de gerador e as existentes no sistema elétrico de potência (SEP), a proteção de seus elementos é um tópico importante para o qual ainda não existem estudos abrangentes. Nesta dissertação são analisados e avaliados sinais elétricos do DFIG em caso de faltas nos seus terminais utilizando a transformada *wavelet* estacionária com borda em tempo real (BSWT-RT) devido ser uma ferramenta com grande potencial para identificar falhas elétricas. Além disso, estudos qualitativos referentes às proteções de sobrecorrente *wavelet*, subtensão *wavelet*, direcional *wavelet* e diferencial *wavelet* são realizados com o intuito de avaliar essas novas tendências de proteção aplicadas a sistemas de conversão de energia eólica (SCEE). Portanto, é verificado se essas proteções funcionam corretamente quando aplicadas a um DFIG. As análises dessas proteções aplicadas a sinais reais, coletados em uma bancada de testes experimentais com DFIG, evidenciam que as ferramentas matemáticas utilizadas obtiveram um bom desempenho para proteção contra faltas elétricas no ponto de conexão comum (PCC).

**Palavras-chave:** Gerador de Indução Duplamente Alimentado, Proteção de geradores, Transformada *wavelet*.

---

# Abstract

---

With the globalization and the rapidly increasing global energy demand, it has been seeking the sustainability guarantee because the growing concern to preserve the planet for future generations. Therefore, investments in clean and renewable energy sources, such as wind power generation, have gained space in research groups in order to overcome their drawbacks and improve the benefits. The doubly fed induction generator (DFIG) is the predominant one in the market of the wind energy. Nevertheless, considering the electrical failures inherent to this generator type and the ones in the power system (PS), the protection of its elements is an important topic that still does not have comprehensive studies. This dissertation DFIG electrical signals in case of machine terminal faults are analyzed and evaluated using the real-time stationary wavelet transform with boundary effect (RT-BSWT). Furthermore, qualitative studies on wavelet overcurrent, wavelet under-voltage, directional, and differential protections will be introduced in order to assess these new protection trends applied to wind energy conversion systems (WECS). Therefore, these protections are verified in order to analyze if they work correctly when applied to a DFIG. Furthermore, analysis applying these protections to real signals, collected by an experimental test-bench with DFIG, demonstrated which the used mathematical tools had good performances for protection against electrical faults at the common connection point (PCC).

**Keywords:** Doubly-fed Induction Machine, Generator protections, wavelet Transform.

---

# Contents

---

<b>Summary</b>	<b>i</b>
<b>List of Figures</b>	<b>iv</b>
<b>List of Tables</b>	<b>vi</b>
<b>List of Symbols</b>	<b>vii</b>
<b>List of Abbreviations</b>	<b>x</b>
<b>1 Introduction</b>	<b>1</b>
1.1 Motivation . . . . .	4
1.2 Objectives . . . . .	4
1.3 Contributions . . . . .	4
1.4 Methodology . . . . .	4
1.5 Work Structure . . . . .	5
<b>2 State-of-The-Art</b>	<b>7</b>
2.1 Protection and Detection Methods Against Internal Faults . . . . .	8
2.2 Methods to Protect the DFIG Against External Faults and Enhance the LVRT . . . . .	11
2.3 Summary of Literature Review . . . . .	13
<b>3 Wind Energy Conversion System</b>	<b>15</b>
3.1 Wind Turbine Components . . . . .	15
3.2 Main Wind Generator Topologies . . . . .	16
3.2.1 Fixed Speed Wind Generator . . . . .	17
3.2.2 Variable-speed turbines with partial-scale power converter . . . . .	17
3.2.3 Variable-speed turbines with full-scale power converter . . . . .	18
3.3 DFIG Electrical System Model . . . . .	19
3.4 Electric Power Converter . . . . .	22
3.4.1 Grid Side Converter (GSC) . . . . .	22
3.4.2 Rotor Side Converter (RSC) . . . . .	24
3.5 Protection Challenges . . . . .	26
3.5.1 Protections Against External Faults and LVRT Enhancement . . . . .	27
3.5.2 Internal Protections . . . . .	30
3.6 Summary . . . . .	32



<b>4</b>	<b>Mathematical Fundamentals</b>	<b>33</b>
4.1	Fourier Transform . . . . .	33
4.2	Wavelet Transform . . . . .	34
4.2.1	Discrete Wavelet Transform . . . . .	35
4.2.2	Stationary Wavelet Transform (SWT) . . . . .	36
4.2.3	Real-Time Boundary Stationary Wavelet Transform . . . . .	37
4.2.4	Scaling and wavelet filters . . . . .	37
4.2.5	Energy of the Scaling and Wavelet Coefficients with Boundary Effect. . . . .	39
4.3	Summary . . . . .	41
<b>5</b>	<b>Fundamentals of Protection Systems</b>	<b>42</b>
5.1	Overcurrent Protection . . . . .	42
5.1.1	Conventional Overcurrent Protection . . . . .	42
5.1.2	Wavelet-Based Overcurrent Protection . . . . .	45
5.2	Undervoltage Protection . . . . .	47
5.3	Directional Protection . . . . .	48
5.4	Differential Protection . . . . .	50
5.5	Summary . . . . .	51
<b>6</b>	<b>Methodology</b>	<b>52</b>
6.1	Protection Applied in DFIG . . . . .	52
6.2	Implementation of the Overcurrent Protection . . . . .	53
6.3	Implementation of the Directional Protection . . . . .	54
6.4	Implementation of the Differential Protection . . . . .	56
6.5	Implementation of the Undervoltage Protection . . . . .	57
6.6	Summary . . . . .	58
<b>7</b>	<b>Protection and Signal Analysis</b>	<b>59</b>
7.1	Experimental Analysis . . . . .	59
7.1.1	Single-Line-to-Neutral Fault . . . . .	60
7.1.2	Line-to-Line-to-Neutral Fault . . . . .	60
7.2	Analysis of the Overcurrent Protection . . . . .	63
7.2.1	Single Line-to-Neutral Fault Analyses . . . . .	63
7.2.2	Line-to-Line Fault Analysis . . . . .	66
7.3	Analysis of the Directional Protection . . . . .	67
7.3.1	Forward Fault Analyses . . . . .	68
7.3.2	Backward Fault Analyses . . . . .	70
7.4	Analysis of the Differential Protection . . . . .	73
7.4.1	Internal Fault Analyses . . . . .	73
7.4.2	External Fault Analyses . . . . .	74
7.5	Analysis of the Undervoltage Protection . . . . .	76
7.5.1	Voltage Sag Analyses . . . . .	76
7.6	Discussion . . . . .	77
7.7	Summary . . . . .	78

<b>8</b>	<b>Conclusion</b>	<b>79</b>
8.1	General Conclusions . . . . .	79
8.2	Future Works . . . . .	80
8.3	Publications . . . . .	80
	<b>Bibliography</b>	<b>81</b>
<b>A</b>	<b>Experimental Test-bench</b>	<b>87</b>
A.1	The Experimental Test-Bench . . . . .	87

---

# List of Figures

---

3.1	Wind Turbine Topology - Horizontal Axis. . . . .	16
3.2	Squirrel Cage Induction Generator (adapted from Taveiros (2014)). . . . .	17
3.3	Doubly-fed Induction Generator (adapted from Taveiros (2014)). . . . .	18
3.4	Permanent Magnet Synchronous Generator (adapted from Taveiros (2014)).	19
3.5	Diagram of the DFIG electrical model in abc (adapted from Taveiros (2014)). . . . .	20
3.6	Single-phase equivalent model - grid side. . . . .	23
3.7	Single-phase equivalent model in dq - rotor side. . . . .	25
3.8	LVRT requirements in different countries (adapted from Comech et al. (2011)). . . . .	27
3.9	DFIG internal faults types - Winding faults types. . . . .	31
3.10	DFIG internal faults location. . . . .	31
4.1	Block diagram depicting the two first decomposition levels of DWT. . . . .	35
4.2	Block diagram depicting the two first decomposition levels of SWT. . . . .	36
4.3	Real-time computation of the wavelet coefficients: (a) original signal, (b) wavelet coefficients of the recursive MODWT, (c) wavelet coefficients of the MODWT pyramid algorithm related to the signal sliding window (adapted from Costa (2014)). . . . .	38
4.4	Comparisons between SWT and BSWT: (a) Original signal, (b) Scaling coefficients energy, (c) Wavelet coefficients energy. . . . .	40
5.1	Characteristic inverse-time curve (adapted from Costa et al. (2017)). . . . .	43
5.2	Characteristic inverse-time curve in the wavelet domain (adapted from Costa et al. (2017)). . . . .	47
5.3	Characteristic time defined curve. . . . .	48
5.4	DFIG differential protection scheme. . . . .	50
6.1	Simplified relay-based protections scheme. . . . .	52
6.2	Measuring instruments location in a DFIG. . . . .	53
6.3	Overcurrent protection steps. . . . .	54
6.4	Directional protection steps. . . . .	55
6.5	Differential protection steps. . . . .	56
6.6	Undervoltage protection steps. . . . .	57
7.1	Fault location. . . . .	59

7.2	Experimental test-bench signals with a one-phase fault to neutral point: (a) Grid voltage in pu; (b) Stator currents; (c) Rotor currents; (d) Stator flux referring to phase A; (e) Machine slip; (f) Rotor speed. . . . .	61
7.3	Experimental test-bench signals with a line-to-line fault to neutral point: (a) Grid voltage in pu; (b) Stator currents; (c) Rotor currents; (d) Stator flux referring to phase C; (e) Machine slip; (f) Rotor speed. . . . .	62
7.4	Overcurrent Protection Analyses: (a) Real signal; (b) Trigger wavelet; (c) phase units - conventional versus wavelet-based. . . . .	64
7.5	Overcurrent Protection Analyses: (a) Overcurrent protection negative sequence unit; (b) Overcurrent protection neutral sequence unit. . . . .	65
7.6	Overcurrent Protection Analyses: (a) Real signal; (b) Trigger wavelet; (c) Phase unit B; (e) Phase unit C; (f) Negative-sequence unit. . . . .	67
7.7	Directional protection phase unit - Forward fault: (a) Wavelet-based directional protection, (b) Fourier-based directional protection. . . . .	68
7.8	Directional protection components sequence units: (a) Directional negative sequence unit; (b) Directional zero sequence unit. . . . .	69
7.9	Directional protection components sequence units: (a) Directional negative sequence unit; (b) Directional zero sequence unit. . . . .	70
7.10	Directional protection phase unit - Backward fault: (a) Wavelet-based directional protection, (b) Fourier-based directional protection. . . . .	71
7.11	Directional protection sequence components unit - Backward fault: (a) Negative sequence unit, (b) Zero sequence unit. . . . .	72
7.12	Directional protection Zero sequence unit - Fourier algorithm. . . . .	72
7.13	Differential protection: (a) wavelet-based; (b) Fourier-based. . . . .	74
7.14	Differential graphic - Internal fault: a) Fourier method b) Wavelet method (normalized). . . . .	75
7.15	Differential protection - External fault: (a) wavelet-based; (b) Fourier-based. . . . .	75
7.16	Differential graphic - External fault: a) Fourier method b) Wavelet method. . . . .	76
7.17	Undervoltage protection: (a) wavelet-based; (b) Fourier-based. . . . .	77
A.1	Experimental test bench: (a) Front; (b) Back. . . . .	87
A.2	Experimental test bench: (a) CPU unit; (b) Electrical diagram (Adapted from Marques et al. (2018)). . . . .	89

---

# List of Tables

---

2.1	Summary of the literature review related to protection and detection methods against internal faults. . . . .	14
2.2	Summary of the literature review related to methods to protect the DFIG against external faults and enhance the LVRT. . . . .	14
3.1	DFIG protection against external faults and LVRT enhancement strategies (adapted from Justo et al.(2015)). . . . .	28
5.1	Instantaneous overcurrent units . . . . .	43
5.2	Curve types and their constants according to IEEE Standard Inverse-Time Characteristic Equations for Overcurrent Relays, 1996. . . . .	44
5.3	Time-delay overcurrent units . . . . .	44
5.4	Wavelet-based instantaneous overcurrent units . . . . .	45
5.5	Wavelet-based time-delay overcurrent units . . . . .	46
5.6	Interconnection system response to abnormal voltages (Adapted from IEEE (2003)) . . . . .	48
5.7	Interconnection system response to abnormal voltages (Adapted from IEEE (2003) and de Cavalcante Paiva (2015)) . . . . .	48
5.8	Conventional directional protection units . . . . .	49
5.9	The wavelet-based operation and polarization quantities (Adapted from Leal et al. (2019)). . . . .	49
7.1	Relay Operating Time for Different Fault Inception Angles. . . . .	65
7.2	Relay Operating Time for Different Fault Inception Angles. . . . .	66
7.3	Directional protection comparison - Forward faults. . . . .	70
7.4	Directional protection comparison - Backward faults. . . . .	73
8.1	Papers resulted from the development of this work. . . . .	80
A.1	Experimental DFIG Parameters. . . . .	88

---

# List of Symbols

---

$L_s, L_r$	Stator and rotor inductance, respectively
$R_s, R_r$	Stator and rotor resistance, respectively
$\Omega_m$	Rotor mechanical speed
$\theta_m$	Rotor mechanic angle
$i_{as}, i_{bs}, i_{cs}$	Stator current in phase a, b, c, respectively
$i_{ar}, i_{br}, i_{cr}$	Rotor current in phase a, b, c, respectively
$v_{as}, v_{bs}, v_{cs}$	Stator voltage in phase a, b, c, respectively
$v_{ar}, v_{br}, v_{cr}$	Rotor voltage in phase a, b, c, respectively
$\lambda_{as}, \lambda_{bs}, \lambda_{cs}$	Stator flux in phase a, b, c, respectively
$\lambda_{ar}, \lambda_{br}, \lambda_{cr}$	Rotor flux in phase a, b, c, respectively
$\omega_s$	Synchronous angular speed
$\omega_r$	Angular frequency of rotor variables
$\omega_m$	Angular frequency of the rotor
$P$	Pole pairs
$\theta_r$	Rotor electrical angular displacement
$s_i$	Slip machine
$f_r, f_{sS}$	Rotor and stator frequency
$L_{sr,abc}$	Mutual inductance matix
$L_{\sigma s}$	Stator leakage inductance
$L_{\sigma r}$	Rotor leakage inductance
$M_{sr}$	Mutual inductance
$T_{em}$	Electromagnetic torque
$P_s, Q_s$	Instantaneous active and reactive power, respectively
$v_f$	Converter output voltage
$v_g$	Grid voltage
$i_g$	Converter output current
$L_f$	Filter inductance
$R_f$	Filter resistance
$v_{df}, v_{qf}$	Converter output voltage d, q, respectively
$i_{dg}, i_{qg}$	Converter output current d, q, respectively
$v_{dg}, v_{qg}$	Grid voltage in d, q, respectively
$L_m$	Magnetizing inductance
$v_{dr}, v_{qr}$	Rotor voltage in d, q, respectively
$i_{dr}, i_{qr}$	Rotor current in d, q, respectively
$\lambda_{dr}, \lambda_{qr}$	Rotor flux in d, q, respectively
$\lambda_{ds}, \lambda_{qs}$	Stator flux in d, q, respectively

$t$	Time domain
$\omega$	Frequency domain
$f(t)$	Time domain signal
$F(\omega)$	Frequency domain signal
$X_r, X_i$	Real and imaginary phasor component, respectively
$\Delta k$	Total number of samples
$f_s$	Sampling frequency
$f_c$	Cut frequency
$f$	System fundamental frequency
$x$	Original signal
$k$	Discrete time domain
$ X $	Original signal module
$\angle X$	Original signal angle
$s$	Scaling coefficient
$w$	Wavelet coefficient
$j$	Decomposition level
$h_\phi$	Low-pass filter
$h_\psi$	High-pass filter
$N$	Total sample number
$L$	Filter coefficient
$p$	Integer number
$\Delta k$	Total sample numbers of a sliding window
$\varepsilon$	Original signal energy
$z$	Boundary level
$\varepsilon^s, \varepsilon^w$	Scaling and wavelet coefficients energy, respectively
$\varepsilon^{sa}, \varepsilon^{wa}$	Scaling and wavelet coefficient energy with boundary
$\varepsilon^{sb}, \varepsilon^{wb}$	Scaling and wavelet coefficient energy without boundary, respectively
$r_f$	Fault resistance
$i$	Current signal
$I$	Absolute current
$I_1, I_2, I_0$	Absolute current of the positive, negative and zero sequences, respectively
$I_s$	Starting current
$I_A, I_B, I_C$	Absolute current in phase a,b,c, respectively
$I_{50}, I_{50N}, I_{50P}, I_{50Q}$	Pick-up current of unit 50, unit 50N, unit 50P, unit 50Q, respectively
$N_{50}, N_{50N}, N_{50P}, N_{50Q}$	Multiplicative constant of unit 50, unit 50N, unit 50P, unit 50Q, respectively
$I_{51}, I_{51N}, I_{51P}, I_{51Q}$	Pick-up current of unit 51, unit 51N, unit 51NP, unit 51Q, respectively
$N_{51}, N_{51N}, N_{51P}, N_{51Q}$	Multiplicative constant of unit 51, unit 51N, unit 51P, unit 51Q, respectively
$I_r$	Load current in normal operation

$I_N$	Neutral current
$T_{at}$	Relay trip time
$TDS$	Time deal setting
$M$	Operating current multiple
$i_{rms}$	RMS current
$E$	Spectral energy
$E_{50}^s, E_{50N}^s, E_{50P}^s, E_{50Q}^s$	Instantaneous phase, neutral, positive and negative pickup energy, respectively
$\mathcal{E}_i^s$	Boundary scaling coefficient energy in steady-state
$\epsilon_i^s, \epsilon_{iN}^s, \epsilon_{iP}^s, \epsilon_{iQ}^s$	Scaling coefficient energy of phase, neutral, positive and negative currents, respectively
$E_{51}^s, E_{51N}^s, E_{51P}^s, E_{51Q}^s$	Time delay phase, neutral, positive and negative pickup energy, respectively
$M^s$	Operating energy multiple
$T_{atw}$	Relay operating time in wavelet
$\Delta k_{\alpha}, \Delta k_{\alpha^2}$	120° and 240° delays, respectively
$V$	System voltage
$V_{27}$	Pickup voltage of the protection function 27
$E_{27W}^s$	Undervoltage pickup energy
$V_{pol}$	Polarizing voltage
$I_{op}$	Operating current
$T, T_1, T_2, T_0$	Phase, positive, negative and zero torque, respectively
$V_1, V_2$	Absolute voltage of the positive and negative sequences, respectively
$Z_{L1}, Z_{L0}$	Positive and zero sequence impedances of the system, respectively
$T^s$	Scaling torque
$S_{Vpol}$	Polarizing voltage scaling coefficients
$S_{iop}$	Operating current scaling coefficients
$\epsilon_{vpol}^s(n)$	Polarizing voltage scaling coefficients energy
$\epsilon_{iop}^s(n)$	Operating current scaling coefficients energy
$\Delta k_{\alpha}, \Delta k_{\alpha^2}$	120° and 240° displacement, respectively
$\Delta k_{Z1}, \Delta k_{Z0}$	Positive and zero sequence line impedances, respectively
$i_1, i_2$	Rotor and stator measured currents, respectively
$I_{op}^d, I_{res}^d$	Differential operating and restrain currents, respectively
$K$	Relay sensitivity factor
$\epsilon_D, \epsilon_R$	Wavelet coefficients energy of the differential operating and restrain currents, respectively
$K_w$	Characteristic curve slope
$E_D$	Differential protection threshold
$\epsilon_D^{wb}$	Wavelet coefficients energy of the operating current with no border effect





---

# List of Abbreviations

---

ANFIS	Adaptative neuro-fuzzy inference system
AWRF	Asymmetrical winding resistive fault
BESS	Battery energy storage system
CSC	Current source converter
CWT	Continuous wavelet transform
CT	Current transformer
DG	Distributed generation
DFIG	Doubly-fed induction generator
DSP	Digital signal processor
DVR	Dynamic voltage restorer
DWT	Discrete wavelet transform
db	Daubechis
EESG	Electrically excited synchronous generator
EPVA	Extended Park's vector approach
FCL	Fault current limiter
FFT	Fast Fourier Transform
FPGA	Field Programmable Gate Array
FRT	Fault-ride through
GSC	Grid side converter
HIL	Hardware-in-the-loop
IGBT	Insulated gate bipolar transistor
ITSC	Inter-turn short circuits
LVRT	Low-voltage ride through
MCSA	Machine current signature analysis
MODWT	Maximal overlap discrete wavelet transform
MPPT	Maximum power point tracking
PCC	Common connection point
PIC	Parallel interleaved converted
PMSG	Permanent magnet synchronous generator
PPgEEC	Graduate program in Electrical and Computing Engineering
PT	Potential transformer
PWM	Pulse Width Modulation
RES	Renewable energy source
RSC	Rotor side converter
RT-BSWT	Real time - Stationary wavelet transform with boundary
RT-SWT	Real-time stationary wavelet transform
SCIG	Squirrel-cage induction generator

SDBR	Series dynamic braking resistor
SDR	Series dynamic resistor
SFCL	Superconducting fault current limiter
SLG	Single line-to-ground
SMES	Superconducting magnetic energy storage
SVC	Static var compensator
STATCOM	Static synchronous compensator
SWT	Stationary wavelet transform
TDS	Time deal setting
UFRN	Federal University of Rio Grande do Norte
VSC	Voltage source converter
WECS	Wind energy conversion systems
WT	Wind turbine

---

# Chapter 1

## Introduction

---

The wind energy conversion systems (WECS) have been inserted in the electrical grid as one of the most promising renewable energy source (RES) to reduce the use of fossil fuels. However, the large insertion of this type of generation in the grid must be based on researches which prove its efficiency and feasibility. Consequently, the generators will obtain a better efficiency in the conversion of wind kinetic energy into electrical energy.

In 2017, the global annual installed capacity was 52,573 MW, achieving 539,581 MW in cumulative installed wind capacity according to the global wind energy council (GWS 2017). In Brazil, this growth is expressive too. For instance, in 2005 there were 27.1 MW of installed capacity and jumped to 14,561.3 MW in 2018, representing 8.1% of the Brazilian electric matrix. Furthermore, there is a growth forecast to 17,880.0 MW until 2023 according to the Brazilian wind energy association (BAGE 2017). This highlights the great importance of researches about this type of generation nowadays.

In worldwide, the most commonly used WECS topologies are the permanent magnet synchronous generator (PMSG) and the doubly-fed induction generator (DFIG) (Li and Chen 2008). However, the DFIG topology is the dominant generator in wind power plants (Mansouri et al. 2016), and its advantage over another types of generators is the low cost of converters because the power converters have a maximum power rate of 30% of the generator power, and it does not have the drawback of the rotor demagnetizing due to a machine overheating.

With the large growth of WECS and the variety of existing generators, the system operators have been imposing high requirements on grid codes for these types of generation plants. Hence, the requirements need to be achieved, such as control of reactive power, control of active power, protective devices and power quality monitoring (Comech et al. 2011). Moreover, achieving the grid requirements is fundamental to enhance the capacity of load flow controlling and keep working properly the interconnected electrical system. Furthermore, another requirement which needs to achieve is the electrical grid and power generators protection against faults and disturbances.

The electrical protection to the DFIG is a challenge because this topology is sensitive to any abrupt drop of the grid voltage since the stator windings are directly connected to the grid. For instance, faults cause oscillations in the stator currents and may generate an electromagnetic torque pulsation. In addition, the DFIG can insert harmonic distortion in the electrical grid due to the presence of the power electronic converters used to control the active and reactive power injection and the DC-link voltage amplitude as well.

There are other elements that increase this challenge, such as (Mansouri et al. 2016):

- Generator speed can oscillate between the sub-synchronous to the super-synchronous operation modes.
- The direction of the rotor power flow can be positive or negative depending on the machine operation mode.
- There is magnetic coupling between rotor and stator winding variables.
- Measured electric signals of the rotor and stator have different frequencies.
- Rotor winding frequency is low and variable.
- Wind farm's intermittency which increases and decreases the steady-state current.
- Disturbances on the electrical grid.

Protection schemes have been used to guarantee the low-voltage ride through (LVRT) by using some LVRT categories, because the DFIG operates considering that the most fault types are transient which last for a short period of time. Together with the LVRT categories are used conventional protection-based methods such as overcurrent, overvoltage, phase-loss, and undervoltage to detect and protect against grid disturbances and electrical faults on the point of common coupling (PCC), which is characterized as a DFIG external fault, avoiding the wind turbine disconnection.

The LVRT is a requirement imposed by grid codes which is the capability of generators remain connected to the electrical grid in case of voltage sag, which is usually associated to a fault in the grid. When a voltage sag occurs the wind turbines need to provide support to the grid. For instance, in Germany, when a voltage drops to zero (which could be due to a fault near the generator) the generators need to remain connected for 150 ms. To achieve the LVRT objectives there are in general three categories of solution (Zou et al. 2016) that are based on control strategies; hardware modification like reactive power injecting devices or protective circuits; and the application of superconducting fault current limiter (SFCL). In addition, there is a category which is a unity between the elements of the first category with the second one. The LVRT categories are triggered in case of temporary external faults and voltage sags at PCC by the protection-based methods or others strategies.

In case of an internal or external permanent fault, the protection applied on the DFIG topology is able to disconnect the turbine in order to prevent the system becoming unstable due to the fault as also protect the generator. Therefore, the protections should be used to monitor individually each element that composes the DFIG assembly against internal faults, such as: the transformer, the power converters, the DC-link coupling. Moreover, the conventional protections must also be used to protect the turbine against internal faults at the electric machine windings as also monitoring and protect against external faults at the PCC.

Many reasons explain the emergence of internal faults in the electric machine, some of them are announced by Abadi et al. (2014):

- Insulation degradation between the individual coil.
- Insulation degradation between different coils.
- Electromechanical induced vibration.

- Thermal overload or contamination.
- High ratio  $dv/dt$  due to power electronic converter feeding the rotor windings.

There are several types of internal faults in electric machines, such as the coil-to-coil, turn-to-turn and open-circuit. In addition, in the rotor terminals, there are faults involving the brushes. Furthermore, there are faults involving the stator and rotor terminal connection points. The most recent researches seek to identify which kinds of these faults occurred. Identification of faults inside generators on initial stages is plenty welcome to enable emergency operation and reduce damage risks (Stojčić et al. 2014). Notwithstanding, faults on the DFIG topology elements beyond the machine windings and connections are also considered internal faults, such as, faults on its power converters.

A mandatory assignment of the protection applied in DFIGs is to distinguish whether the electrical fault is internal or external. Therefore, the monitoring system needs to be uninterrupted and accurate to detect all faults inside the DFIG and at the PCC. Therefore, identifying and differentiating the fault types are essential because each type of failure needs a different procedure to be adopted. In the case of a temporary external fault, the LVRT categories need to be triggered as aforementioned, whereas in the case of internal faults the wind turbine needs to be disconnected.

The overcurrent, overvoltage or undervoltage protections are ineffective to identify if the fault is external or internal. However, the differential protection, which is extensively applied in power transformers (Medeiros and Costa 2018) and transmission lines (Dambhare et al. 2009), would be suitable to distinguish if the fault was internal or not. Nevertheless, this protection is not usual in DFIGs, only in recent works this protection type was applied to this generator type (Mansouri et al. 2016) - (Zarei et al. 2018). In addition, the directional protection can also be used for this purpose because it is able to identify the direction of the power flow, in consequence, the fault direction.

The conventional directional protection is based on measuring of electrical signals, using the Fourier transform, which uses phasor estimation. Fast signal processing tools, such as the real-time stationary wavelet transform with boundary effect (RT-BSWT) proposed by Costa and Driesen (2013), can provide faster fault detection (Costa 2014). Therefore, a protection and detection method based on the RT-BSWT can provide a fast relay sensitization which it is essential to ensure the rapid activation of the LVRT categories in case of external faults at the PCC, and to protect against internal faults inside the DFIG topology.

In this context, the protection and detection systems must properly actuate for each type of fault. Therefore, the development of protection and detection methods based on modern signal processing tools, such as the wavelet transform, is of high priority. Moreover, the methods need to be capable of detecting if the fault occurred at the PCC or inside the DFIG assembly, such as faults in the stator and rotor terminal connection points, this is of great importance for choosing the correct protection action for each fault type. Furthermore, assess and validate new protection trends, for instance, the overcurrent, the differential, the directional and the undervoltage wavelet-based protections, is important to prove that these new methods work properly in a system with the aforementioned characteristics.

## 1.1 Motivation

Nowadays, there is no standardization of protections and fault detection methods applied to DFIG topology. However, this type of wind turbine is the most used today in onshore wind farms. Some recent publications have approached the theme of protection and fault detection methods, highlighting their challenges and the implementation difficulties. Notwithstanding, most of the studies only address the impact of these generation types on the grid code requirements in order to guarantee these specifications, instead of developing an efficient and reliable fault detection method for the wind generators capable to distinguish whether the fault occurred externally, at the PCC, or internally, inside the DFIG assembly, due to each fault type to need a different decision-making.

## 1.2 Objectives

The goal of this work is to verify if wavelet-based protections and fault detection methods to distinguish between internal and external faults can be properly used in a DFIG.

To achieve the expected results, the following specific objectives have been defined:

- To verify if the wavelet-based overcurrent protection is feasible in a DFIG topology.
- To verify if the wavelet-based undervoltage protection is feasible in a DFIG topology.
- To verify if the wavelet-based directional protection is feasible in a DFIG topology.
- To verify if the wavelet-based differential protection is feasible in a DFIG topology.
- To analyze DFIG signals in case of faults in the machine terminal connections using RT-BSWT and real experimental data.

## 1.3 Contributions

The main contributions are:

- Obtaining reliable analyzes of the DFIG in case of electrical faults using the RT-BSWT.
- Confirmation which it is possible to apply the wavelet-based overcurrent and undervoltage protections in a DFIG topology.
- Confirmation which it is possible to apply the wavelet-based directional and differential protections in a DFIG topology.

## 1.4 Methodology

Among the scientific method typologies, this work is anchored in the hypothetical-deductive method, which provides all operational resources to the development of the

research processes, since the problem delimitation until the final results, in order to reach the goals of this dissertation.

It was reviewed the state-of-the-art of the protection types and detection methods applied in a DFIG topology nowadays, and verified which protection schemes are used to detect and protect against faults inside DFIG assembly and which strategies are used to enhance the LVRT in case of external faults or grid disturbances at the PCC.

Some theoretical studies about the DFIG, the wavelet transform and the relay-based protections were done in order to acquire the necessary knowledge to validate an internal protection to the DFIG and a detection method capable to identify if a fault occurred inside or outside the DFIG topology.

Concerning about the exposed, it was validated protection algorithms capable to detect if the electrical fault occurred inside the DFIG topology, such as in the power converters, in the machine, and in the connections, as also capable to detect if the fault occurred outside, externally, to the DFIG assembly such as at the PCC. Furthermore, it was carried studies about wavelet-based protections, for instance, overcurrent, differential, directional and undervoltage protection, applied in a DFIG.

For finish, off-line analysis with real experimental data, obtained in a DFIG test bench, was used to the assessment in order to provide more accurate and realistic analysis to the validated methods.

## 1.5 Work Structure

This dissertation is organized in eight chapters:

- Chapter 1, that presented an introduction about the growth of WECS insertion in the electrical grid, specifying the most used topologies and problems occasioned in the electrical power systems protection due to this insertion. In addition, the solutions adopted to solve these problems are depicted.
- Chapter 2, that illustrates the current state-of-the-art of the protections applied to DFIG. However, this review is made in two different perspectives, the first one is about internal protections and detection methods used to protect the DFIG assembly, whereas, the second one is about protections applied against external faults to protect the DFIG elements and enhance the LVRT requirements.
- Chapter 3, that discusses about the WECS fundamental theory in order to introduce the main topologies applied in wind farms, as well as the electrical model of a DFIG. In addition, it is presented an introduction about the electrical protection applied into DFIG and their challenges.
- Chapter 4, that introduces the theoretical basis of the Fourier transform. Furthermore, the wavelet transform is introduced with focus on different versions of this transform.
- Chapter 5, that presents the theoretical basis of the wavelet-based overcurrent, undervoltage, directional and differential protections.
- Chapter 6, that illustrates the evaluation of the DFIG experimental data variables, such as the stator and rotor currents, the voltages, and slip machine as well as the



rotor speed.

- Chapter 7, that illustrates the evaluation of all the results obtained through the use of the proposed methodology with a critical point of view.
- Chapter 8, that presents the conclusions obtained in the development of this work, as well as proposals topics for future work.

---

# Chapter 2

## State-of-The-Art

---

The DFIG has been gained prominence in the global scenario due to its application in wind farms, a fact of no more than 40 years. However, one of the first scientific studies present in the literature about this type of electric machine is dated from 1941, wherein Lishwitsch (1941) focused about the mathematical development of this machine, specifically about the damping and synchronizing torque. In the next year, Concordia et al. (1942) developed some analysis showing transients characteristics and the machine equivalent circuit. Notwithstanding, until the eighties, the academical investigation about this theme was restricted to a few scientific papers.

After this period, the researches about DFIG grew exponentially due to the emergence of wind power generation. Therefore, it was required to develop studies which circumvented the problems of this application type, for instance, control strategies (Ioannidou and Tegopoulos 1987), efficiency (Ioannides and Tegopoulos 1988), active and reactive power control (Pena et al. 1996, Muller et al. 2002) and system stability (Rahim 1988).

In the 2000s, the researches applied to the DFIG topology aimed to achieve the requirements imposed by the grid operators, mainly the LVRT, due to the increasing number of WECS installed in the electrical grid. Therefore, the studies focus became the protective devices applied during transient-state; reactive power injecting devices during transient-state; and control structures applied in steady- and transient-state (Justo et al. 2015). This research area keeps until today as the main one when it comes to DFIG topology. Moreover, this field is important because achieve the grid codes and protect the DFIG elements against overcurrent and undervoltage in case of voltage sag or faults at the PCC, which is considered as external faults.

In recent years, appeared an interest in protecting the DFIG topology against internal faults, both in the machine windings and in the other elements that compose the set. This research field interest is in order to prevent against high economic losses and protect the electrical system, avoiding wind parks disconnection and high generator damages.

This chapter provides a state-of-the-art survey of protection and detection methods against internal faults in DFIG topology. Furthermore, a review about methods to protect the DFIG against external faults and enhance the LVRT is also introduced because external faults at the PCC can cause overcurrent and undervoltage inside the DFIG assembly. The strengths and weaknesses of these two types of fault prevention are presented.

## 2.1 Protection and Detection Methods Against Internal Faults

A condition monitoring system of wind generators using machine current signature analysis (MCSA) is presented by Popa et al. (2003). The purpose of this research is to adapt a fault detection technique applied in induction machines to a DFIG with a monitoring system. It is done an experimental system with a wind turbine model and a generator model system used to validate the analysis. The AD Card - ICS 645 is used to measure the signals and the software Matlab is used as a processing unit. Three different analysis were presented to validate the system, the first was a stator phase unbalance, the second was a rotor phase unbalance, whereas the third one was a turn-to-turn fault. In relation to the presented, the results indicated that the monitoring system correctly works for all cases in accordance with the theory. However, even with good results, this article does not present an innovative method for detecting faults. Nevertheless, it explains in detail how to implement a complete monitoring system.

Douglas et al. (2005) presented an inter-turn stator fault detection method for DFIG using the DWT and the extended Park vector approach (EPVA). It is demonstrated that steady-state techniques are not effective when applied during transient conditions. Experimental simulations of a generation system model with a 2.2 kW DFIG were performed using the ds1104 R&D controller card to validate the proposed method. In addition, the recorded data were processed in the Matlab software. The proposed is to decompose the nonstationary EPVA signal into the scaling and wavelet coefficients using Haar as mother wavelet. Furthermore, a Gaussian distribution is used to determine with occurred or not an internal fault, where a bimodal shape indicates a turn fault. However, grid faults were not validated, thus this behavior may be reproduced and an equivocal detection can happen.

The employment of fast Fourier transform (FFT) to analyze the spectrum of rotor modulating signals to detect incipient electrical faults in DFIG was proposed by Stefani et al. (2008). The proposed method analyzed the rotor modulating signal spectrum in case of internal electrical faults, as well as for comparative criteria make the same study to the stator and rotor current spectrum. The first one demonstrated the best effectiveness and accuracy to detect faults. Simulations made on Matlab/Simulink software and experimental analyzes with the control implemented on dSPACE were used to evaluate the performance of the method. Therefore, it was obtained promise results in both validation strategies. However, the type of faults applied to validate the method was the asymmetrical winding resistive fault (AWRF) whereas inter-turn faults were not studied in this research. Thus, only one kind of fault was validated missing another study to analyze inter-turns faults.

Kang et al. (2009) developed a protection algorithm based on the 'dq' equivalent circuit in the time domain. The algorithm estimates the induced voltages in the machine windings using the stator and rotor currents and voltages at the stationary reference frame. It is obtained two fault detectors, one refers to the d-axis and another to the q-axis if the detectors values exceed 5% sixteen times the trip signal is activated. To verify the protection, a generation system was developed in the PSCAD/EMTDC, two different fault types were implemented, a turn-to-turn fault and a three-phase external fault. Simulation

results with satisfactory performance were presented to validate this method. However, it was not performed analysis considering Gaussian noise.

Shah et al. (2009) proposed a novel stator fault detection scheme for DFIG using the rotor current and search-coil voltage. This method is simple and provides a reliable fault detection, which does not confound with the grid imbalances. The evaluation of this scheme was performed using six simulated cases beginning since electrical grid imbalances until internal faults in the stator windings. In addition, It was made an experimental test bench to confirm the obtained results by simulations. The proposed method uses rotor current harmonics theory in case of the stator winding faults and the power spectral density to determine with occurs an internal fault or not. However, through the information supplied by this scheme, the fault detection is not possible for rotor windings faults.

Junqing et al. (2013) presented an inter-turn detection method for the rotor windings based on negative sequence component. However, the fault identification is difficult when there is a grid imbalance together with an inter-turn fault. Therefore, they also used harmonic analyses to discriminate between these cases. Furthermore, it was noticed that the negative sequence increases and the third and fifth harmonic appear in case of an internal fault. The validation of the method was performed using ANSOFT MAXWELL software to simulate the machine model. However, the limitations of this work are the few cases analyzed, in which did not investigate the signals in case of huge grid disturbances or asymmetries, because in these situations harmonic components and negative sequence also appear which it is difficult the correct fault detection.

Kia et al. (2013) proposed a novel DFIG model with inter-turn stator faults, and the machine proposed model is a hybrid between the 'ABC/dq' variables, because of machine models in 'ABC' reference frame have a time-varying inductance matrix, whereas machine models in 'dq' reference frame cannot eliminate time dependency when using asymmetric matrices. However, the proposed modified model is able to obtain constant matrices in case of an internal fault. In addition, a detection method using discrete wavelet transform (DWT) with Daubechis with four coefficients (db 4) as mother wavelet was presented, and the analyzed signals were the stator currents. The method consists of extract the energy of the measured signals and obtains an index to work as a threshold. The actuation occurs when the analyzed energy signal passes the threshold, which means that an internal fault was identified. However, this method did not analyze the signals in case of wind variation and grid disturbances which may increase the stator current energy and give a false positive. In addition, the validation was made only by simulation on Matlab software in an m-file, wherein the control system used to control the power converters that fed the rotor windings was substituted by a rotor proportional voltage according to the slip machine, which is a relation between the synchronous speed and the rotor speed, neglecting factors such as wind characteristics and converter switching. Furthermore, through the information supplied by this scheme, faults on the rotor side is not supported.

Jun-qing et al. (2013) presented a method for the rotor winding inter-turn fault detection. The machine model is implemented using a multi-loop theory of the AC machine and a rotor fault was modeled too. In relation of the proposed method, a FFT was used for analyzing the current signal spectrum. This work affirms that the use of the stator current signal is a better choice than the rotor current signal to detect faults, because in the stator

current signal appears only the third harmonic in fault case, making easier the detection. However, only one situation was analyzed, thus it was a weak validation. Furthermore, no experimental verification was performed to prove the detection method effectiveness in order to ensure that the method would not confound grid disturbance with inter-turn faults.

A detection method for stator and rotor inter-turn faults with an automatic diagnostic system with remote data collection was proposed by Abadi et al. (2014) using the FFT. The stator voltages and currents are required to estimate the instantaneous reactive power for fault diagnostic purposes. Furthermore, the method is developed according to the proposition that in case of stator faults, a component with twice the grid frequency will appear on the signal spectrum and in case of rotor faults the same thing will happen multiplied by the machine slip. However, this phenomenon occurs in cases of grid imbalance too. Therefore, it is not correct to use this information as the main one to detect an internal fault. Experimental verification was made and the control scheme was implemented in a dSPACE. In the test rig many analyses with the machine operating in healthy, in stator fault, and in rotor fault conditions were accomplished. However, in case the machine operates close to the synchronous speed the method does not work properly.

Stojčić et al. (2014) developed a scheme to detect stator and rotor winding asymmetries for a DFIG. This method applies short voltage pulses on machine terminals by inverter switching and measures the current reaction from each phase to get the transient leakage inductance to estimate a denoted asymmetry phasor. The estimated phasor passes through a digital processing using FFT to analyze in its spectrum if there was any winding asymmetry. In addition, the asymmetries can be detected in position and in severity. Furthermore, all validation process was made by an experimental procedure. Besides that, to guarantee a reliable investigation of the method, different fault scenarios were applied for the method verification, such as symmetrical, one turn phase, two turns phase, five turns phase and complete phase faults.

Roshanfekar and Jalilian (2016) proposed a new fault diagnostic index using the normalized energy calculation from the DWT. Two types of faults were investigated, the first one was inter-turn short-circuit fault and the second one was winding resistive asymmetrical fault. The fault is detected when the rotor-voltage energy goes through a threshold determined by the energy of the DFIG when in healthy operation. The db(10) mother wavelet was used with a sampling frequency of 10KHz. A performance verification of this scheme was executed using the Matlab/Simulink software and satisfactory results were obtained. However, the diagnostic method failed under minor windings asymmetry in the stator asymmetrical winding faults. Nevertheless, the fault detection method demonstrated awesome performance for the detected fault types.

Abdelemam et al. (2017) presented a based DWT scheme in which any internal faults at the stator windings is detected. There is a fault detection unit responsible to detect and analyze the faults cases using the wavelet energy magnitude. The validation of the method was performed using an EMTP-ATP model and the proposed technique was applied using the LabVIEW software. The limitations of this work are the unique fault type used in the simulation which was a three-phase fault in the stator terminals, consequently, limited the proposed, and the absence of inter-turn fault considerations. To protect the machine a trip

signal is sent in case of the wavelet energy pass a threshold.

A novel differential protection method applied to DFIG using Park transformation was proposed by Zarei et al. (2018). The stator and rotor currents in the synchronous reference frame are compared to obtain the differential currents in 'dq' at the time domain, in case of these differential currents pass a threshold the machine will trip. A simulated verification, using the software Matlab/Simulink, was executed, in which four different fault types were implemented, being two internal faults and two external faults. However, were not considered in the analyses faults in the machine windings. The presented results demonstrated the proper operation of the method with a good behavior of the protection. However, the noise influence was not evaluated and the threshold values were based on a fixed value in which the differential restrain current was not used.

## **2.2 Methods to Protect the DFIG Against External Faults and Enhance the LVRT**

Okedu et al. (2012) presented two control schemes which work in combination with a braking resistor and a DC-link chopper. The first scheme is a control strategy based on supplementary rotor current and the second one uses a series dynamic braking resistor (SDBR) connected to the stator windings. The simulated results were obtained through the software PSCAD/EMTDC wherein a three-phase fault was applied to the analysis. In addition, the proposed strategy was applied to a multi-machine system including wind farms. The second scheme was better in performance than the first one because the second scheme is able to give better responses of the DC-link voltages and limits the stator overcurrent. The limitations of this work are the absence of analysis of other fault cases by simulations and experimental examination.

Vrionis et al. (2014) explored the possibility of using a fuzzy controller tuned by a genetic algorithm to improve the LVRT capability. A control modification on the conventional rotor side converter (RSC) controller was made, wherein a block called 'fault detection & confrontation system' was inserted. However, this new block is activated only in case of the grid voltage suffers a deviation higher than 10%. To validate the effectiveness of the proposed method simulation with a three-phase fault was applied at the PCC using the software Matlab/Simulink. The simulation results confirm the feasibility of the method and the DC-link fluctuations were attenuated. In addition, a new analysis under 85% voltage dip was done to prove that the proposed method works properly in this scenario. In spite of this, the quantity of data used for performance evaluation was low to validate this method.

Shen et al. (2015) explored the possibility of using an energy storage device connected to the DFIG to support the voltage transient capabilities and enhance the LVRT. In a transient period, the DFIG is reconfigured in which the energy storage device is connected in the DC-link and the GSC is disconnected from the grid and connected in parallel with the RSC to enhance the grid voltage support and injecting more reactive currents. In addition, it was made a control modification to act during the transient state and to validate the proposed scheme was performed three different cases studies, by simulations, to analyze the

system reliability, the first one was applied symmetrical and asymmetrical faults with high wind speed, the second was a similar case with a low wind speed, whereas the last one was compared the LVRT behavior with different control strategies. The simulation results confirm the feasibility of energy storage device to support transient voltage capabilities.

Zou et al. (2016) proposed a novel protection scheme for DFIG-WT using a resistive type of SFCL, which is defined as one of the three categories to enhance the LVRT capability. The superconducting fault current limiter (SFCL) is connected in series with the rotor windings, and to evaluate the proposed material it was made comparative studies with the conventional crowbar-based scheme. The validation of this scheme was performed using simulation, in which two different fault types were used, the first one was a three-phase fault and the second one was a line to line fault wherein both of them were applied on the grid. In all analyzed cases the proposed structure obtained a better performance than the crowbar-based scheme. However, this structure has a high implementation cost, due to use an expensive superconducting material, which until today is economically inviable.

Guo et al. (2016) presented a fault current limiter-battery energy storage system (FCL-BESS) that enhances the LVRT ability of DFIG. The proposed assembly combines the fault current limiter and energy storage functions using a superconducting material, wherein the FCL is used to protect the DFIG topology whereas the BESS is used to stabilizing the DC-link voltage. The FCL-BESS topology is connected in series with stator windings and in parallel with DC-link. This scheme was explained since the steady-state operation until a transient state using an experimental prototype under symmetrical, asymmetrical fault conditions and in normal operation. The proposed method solve two difficult problems. However, it is too expensive to be implemented due to use a superconducting coil to limit the current. The scheme performance was evaluated using a DSP to the processing unit and demonstrated accurate results for all investigated cases.

The employment of parallel interleaved converted (PIC) and SDBR to enhancing the DFIG stability in a three-phase fault situation was proposed by Okedu (2016). The proposed strategies need two back-to-back converters connected on rotor windings and an SDBR connected in series with stator windings. Simulations were used to evaluate the performance of the topology using the PSCAD/EMTDC software. However, only a few cases were analyzed let it open the accuracy and reliability for different operating condition. In spite of that, the scheme improves the DFIG performance during transient conditions for the analyzed case. However, it is expensive and complex to be implemented because needs two back-to-back power converters connected in parallel and a SDBR as hardware additions.

An adaptative neuro-fuzzy inference system (ANFIS) crowbar protection for detecting grid faults in DFIG-WT systems is proposed by Noureldeen and Hamdan (2017). The ANFIS proposed is used as a fault detector to activate and deactivate the crowbar-based protection. Besides that, two different structures were proposed, called ANFIS inner crowbar technique and ANFIS outer crowbar protection technique. In the first one, the crowbar was put in series with rotor windings whereas in the second one the crowbar was put in parallel with the PCC. Based on these assemblies, a three-phase fault at the wind turbine terminals was simulated using the software Matlab/Simulink to observe the system

behavior. A comparison with a system without crowbar was also performed. Therefore, the outer crowbar protection was better in performance with a better time detection and the generator remained connected to the grid during the fault occurrence. However, this paper was focused only on the analysis in a simulated environment without experimental tests and only use a crowbar circuit as a protection, which is old-fashioned. Because in the case of inner crowbar technique the rotor circuit is disconnected during grid fault making the turbine loose active and reactive power control, whereas in the case of outer crowbar method the resistors are connected in series which increase the energy losses.

Xiao et al. (2018) developed a scheme to reduce overcurrent on stator windings and enhance transient power stability of the DFIG by a superconducting magnetic energy storage - FCL (SMES-FCL). In comparison with other proposes that use superconducting materials this one has a low operating cost. This assembly needs only to connect a DC-DC converter in series with the stator windings and in parallel with the DC-link. In addition, a new control is proposed to propitiate a fast current recovery in case of fault. At first, the superconducting coil parameters are estimated, after that, it is applied to the system. To validate the proposed method, simulation was made in different scenarios, where the first one was with random varying wind speed and the second one were three-phase, line-to-line, and single-line faults. In addition, an evaluation under different initial fault current angles was made. However, the accuracy of this method is highly dependent on a careful study of the correct parameter estimation, which hampers its adaptation in systems with different characteristics.

A SFCL-magnetic energy storage system (SFCL - MES) is proposed by Guo et al. (2018). The method presented is able to ensure the LVRT requirement and solve the power fluctuation problem. A superconducting coil is used as a energy storage device and a fault current limiter. Furthermore, there is a power condition system responsible to control the power dynamic. This scheme withstands the effects of wind speed variation and limiter the current in case of a fault at the PCC. In order to validate the proposed, it was implemented with real physical elements and installed in a DFIG presented in a wind farm near Yumen city. However, the SFCL-MES implementation has the problem of occupying a large space and using superconducting elements that make the implementation expensive.

## 2.3 Summary of Literature Review

Based on the literature reviewed, many different strategies were used to protect the DFIG topology and detect faults. However, the proposed methods are not able to determine if the fault occurred externally, at the PCC, or internally, inside the DFIG elements precisely. Therefore, it is needed to develop an protection method fast in response and reliable to indicate the correct fault location to protect the generator against external and internal faults and give the correct procedure for each fault type. Therefore, an alternative to overcome this drawback is using the directional and differential protection principles to be used in a protection scheme and in a detection method applying the RT-BSWT.

Table 2.1 summarizes, in chronological order, the main publications related to protection and detection methods against internal faults, whereas Table 2.2 presents a summary



of the literature review related to methods to protect the DFIG against external faults and enhance the LVRT. The employed technique, the evaluated signals, and the validation method, if via simulations and/or experiments, are highlighted.

Table 2.1: Summary of the literature review related to protection and detection methods against internal faults.

Reference	Employed Technique	Signal Processing	Validation	
			Sim.	Exper.
Popa et al. (2003)	MCSA	Stator and Rotor Currents	–	✓
Douglas et al. (2005)	DWT & EPVA	Stator current	–	✓
Stefani et al. (2008)	FFT	Rotor Modulating	✓	✓
Kang et al. (2009)	Park Transformation	Voltages and currents	✓	–
Shah et al. (2009)	Harmonic Theory	Rotor current	✓	✓
Junqing et al. (2013)	Negative Seq. Component	Rotor Current	✓	–
Kia et al. (2013)	DWT	Stator Current	✓	–
Jun-qing et al. (2013)	FFT	Stator Current	✓	–
Abadi et al. (2014)	FFT	Reactive Power	–	✓
Stojčić et al. (2014)	FFT	Rotor Current	–	✓
Roshanfekar and Jalilian (2016)	DWT	Rotor Voltage	✓	–
Abdelemam et al. (2017)	DWT	Stator Current	✓	–
Zarei et al. (2018)	Differential Protection	Stator and Rotor Currents	✓	–

Table 2.2: Summary of the literature review related to methods to protect the DFIG against external faults and enhance the LVRT.

Reference	Employed Technique	Hardware Addition Location	Validation	
			Sim.	Exper.
Okedu et al. (2012)	SBDR & SRC	Stator and Rotor Windings	✓	–
Vrionis et al. (2014)	GA & Fuzzy	No Hardware Addition	✓	–
Shen et al. (2015)	Control modification	Energy Storage Device	✓	–
Zou et al. (2016)	SFCL	Rotor Windings	✓	–
Guo et al. (2016)	FCL-BESS	Stator Windings and DC-link	–	✓
Okedu (2016)	PIC & SDBR	Stator Windings and Converter	✓	–
Noureldeen and Hamdan (2017)	ANFIS	Stator or Rotor Windings	✓	–
Xiao et al. (2018)	SMES-FCL	Stator Windings and DC-link	✓	–
Guo et al. (2018)	SFCL - MES	Stator Windings	–	✓

---

# Chapter 3

## Wind Energy Conversion System

---

This chapter presents an introduction to wind conversion systems explaining about the major mechanical components that compose a typical wind generator assembly and the main topologies applied commercially, the DFIG electrical model in "abc" and "dq", a brief explanation about grid side converter (GSC) and the rotor side converter (RSC). Furthermore, it is addressed a discussion about LVRT, internal protections and its challenges.

### 3.1 Wind Turbine Components

Figure 3.1 depicts a typical structure of a horizontal axis wind turbine which is composed by a tower, a nacelle and a rotor, in what way this is the mostly used wind turbine type nowadays (Ackermann 2005). However, there are wind turbines in vertical axis, for instance the Darrieus and Savonius. Notwithstanding, the researches and developments of this types of wind turbine were practically interrupted after the decade of 1980 (Ackermann 2005) because of some drawbacks caused by these kind of topologies, such as low efficiency and high mechanical stress.

Horizontal wind turbines generate energy when a wind force attains on turbine blades which provoke an emergence of a torque, that makes the turbine rotate. The turbine rotation triggers the low speed shaft, inside of nacelle, which transfers kinetic energy to the gearbox which operates by rotating the high-speed shaft with an increased rotational speed until a nominal generator rotational speed that converts mechanical energy into electrical energy.

Depending on the system power, a transformer should be used to connect the generator to the electrical grid, which can be of two or three windings. The transformer is essential, in some cases, because the output voltages of the generator are low. A rotor brake is equipped in the high-speed shaft to protect the system from mechanical wear when exposed to severe winds. Moreover, there is a compartment with the electric power converters, which are present in the case of variable speed wind turbines, and the control system to regulate the output power. In addition, there are different sensor types which include the wind vane, the anemometer, speed or position sensors, as well as voltage and current sensors.

There is the wind turbine tower that was not depicted on Figure 3.1. The tower is

connected to the ground by means of a concrete foundation and there are inside on it the power transformer, the transmission cables and a ladder giving access to the nacelle.

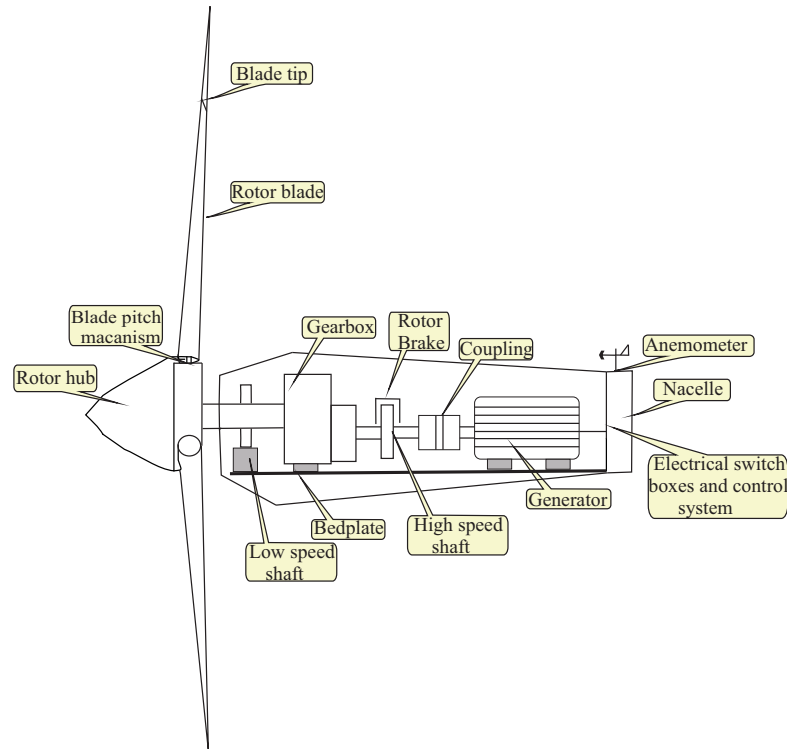


Figure 3.1: Wind Turbine Topology - Horizontal Axis.

## 3.2 Main Wind Generator Topologies

As aforementioned, the most commonly used WECS topologies in the market are the PMSG, the SCIG and the DFIG. Notwithstanding, there are many others types of wind generators, for instance, the electrically excited synchronous generator (EESG) which is more usual in low-speed machine, the brushless DFIG which is a vary of DFIG and the wound rotor induction generator which is a common type machine (Li and Chen 2008).

Referring to generators applied to wind turbines the development of technologies started 1970s (Li and Chen 2008). Among the different classification types of these generators, the most common is related to the rotation speed which are fixed speed, limited variable speed, and variable speed. These characteristics combined with mechanical control mechanisms and aerodynamics design become possible to develop models with desired typical features, such as lower project costs, power control, and generation stability.

### 3.2.1 Fixed Speed Wind Generator

The fixed speed wind turbine cannot be regulated automatically and the generator tends to work at almost in constant speed, varying according to the grid frequency, gearbox ratio, machine slip and characteristic of the electric generator independently of wind speed, because the generator is connected directly to the grid (Wu et al. 2011).

The SCIG is the first and simplest topology used in this type of generator, and it was created reusing electrical and mechanical components existing in the market (Abad et al. 2011), which is illustrated in Figure 3.2. A transformer is needed to couple the grid voltage to the electric machine voltage.

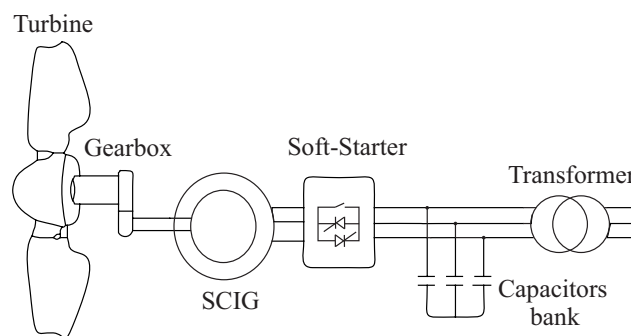


Figure 3.2: Squirrel Cage Induction Generator (adapted from Taveiros (2014)).

There are some advantages to use SCIG, for instance, this machine type has a well-known and tested technology because it has been widely used in the industry for years; reduced and simple maintenance, hence robustness; and a low manufacturing cost. Nonetheless, there are some drawbacks, such as, no speed control; low aerodynamic efficiency; and there is no fault ride-through capability according to Serrano-González and Lacal-Arángeui (2016). Furthermore, there is no reactive power control (Taveiros 2014) and it is susceptible to cause voltage instability. Therefore, this turbine can decrease the power quality indexes at the PCC depending on the electrical grid. Moreover, this generator needs additional equipment, e.g., soft starter, a bank of capacitors and key protection to work properly when connected to the electrical grid when compared to the DFIG.

### 3.2.2 Variable-speed turbines with partial-scale power converter

The wind turbine generator with variable speed became the main technology applied in wind power plants because they have an ability to adapt the wind turbine speed to the wind speed, greater efficiency of the wind system, reduction of mechanical stress imposed on wind unit components when occurs wind gusts and improvement of the energy quality when compared to the fixed speed wind generator.

The DFIG topology, illustrated in Figure 3.3, is a variable-speed turbine with a partial-scale power converter. Furthermore, its speed is controlled by a power converter, wherein the stator windings are connected to the electrical grid, whereas the rotor windings are connected to a back-to-back converter.

The back-to-back converter controls the rotor frequency by control strategies, varying this frequency in a specific range, and the frequency control makes possible to control the wind turbine rotor speed. Wherein, this speed is enabled to vary in a range of  $-40\%$  to  $30\%$  of the synchronous speed (Ackermann 2005). This assembly has a partial power control and it is independent of active and reactive power exchanged with the grid (Abad et al. 2011). In addition, this topology has a smaller line-filter than the full-scale power converter turbine category.

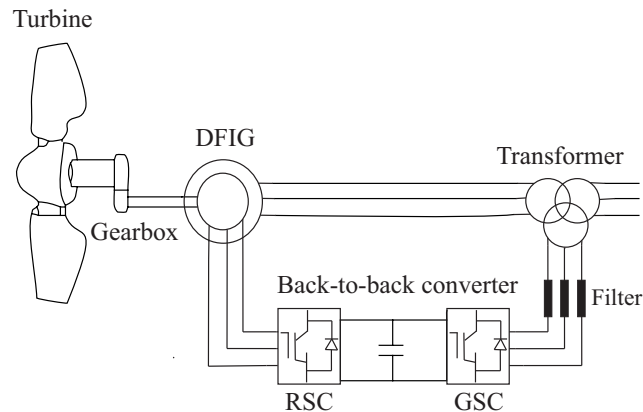


Figure 3.3: Doubly-fed Induction Generator (adapted from Taveiros (2014)).

The generated power can be delivered to grid through stator and rotor circuits. Notwithstanding, the rotor circuit can also absorb power from the grid depending on the machine rotation speed in relation to the synchronous speed. Among the DFIG drawbacks, it is highlighted the rotor circuit connection with converter, which is done through collector rings and brushes with a service life in a range of 6 to 12 months only, requiring periodic maintenance (Yaramasu et al. 2015), limited speed variation range compared to a full-scale topology, and requires higher maintenance than SCIG (Serrano-González and Lacal-Arántegui 2016).

### 3.2.3 Variable-speed turbines with full-scale power converter

The variable-speed turbine with a full-scale power converter is illustrated in Figure 3.4. The most used machine type for this turbine category is the PMSG and the SCIG. Some advantages of this assembly is that it does not need rings and brushes connected on rotor circuit, which reduce maintenance cost.

Others benefits are the ability of full control of active and reactive power, reactive power compensation capacity, increase immunity against electrical power system failure and wind gusts, the mechanical decoupling between machine and grid, which allows the generator to produce electrical power at any speed and the frequency of the generator which can vary according to the wind speed, while the frequency at the output of the inverter remains unchanged and equal to the electrical system.

Among the disadvantages, it is mentioned by Serrano-González and Lacal-Arántegui (2016) is that the power converter has the same power of generator which makes it expen-

sive. Moreover, another drawback is that the generator is heavier than the aforementioned generators when used in bigger wind turbines. In addition, the line filter, which is responsible to attenuate the harmonics injected into the grid introduced by the converter and control the power flow, is bigger than the DFIG line filter.

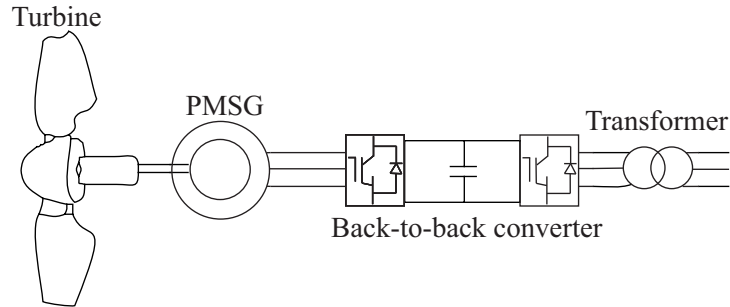


Figure 3.4: Permanent Magnet Synchronous Generator (adapted from Taveiros (2014)).

The generator of this turbine model is able to be connected to the turbine without to use a gearbox. However, this connection type needs a machine with multipoles (Yaramasu et al. 2015) increasing the generator diameter, hence, increases the installation costs.

### 3.3 DFIG Electrical System Model

The DFIG machine model on the stationary frame (abc) is represented by three stator windings and three rotor windings as depicted in Figure 3.5. The stator windings are identical wherein  $L_s$  is the stator self-inductance and  $R_s$  is the stator resistance. In the rotor side, there are identical windings too, in which  $L_r$  is the rotor self-inductance and  $R_r$  is the rotor resistance. The rotor mechanical speed is  $\Omega_m$  and  $\theta_m$  is the angular displacement between the rotor phase ‘a’ relative to the stator phase ‘a’.

According to Abad et al. (2011) some propositions should be adopted to simplify the machine equation model development. For instance, the stator and the rotor windings are connected in the wye configuration. In addition, the stator windings are supplied at a constant and balanced three-phase AC voltage amplitude and frequency delivered by the electric grid and the rotor is supplied at a constant and balanced AC voltage amplitude and frequency delivered by a power converter, independent from the stator. Furthermore, it is ignored the non-linear magnetic saturation effects. Therefore, the stator and rotor instantaneous voltages are expressed by:

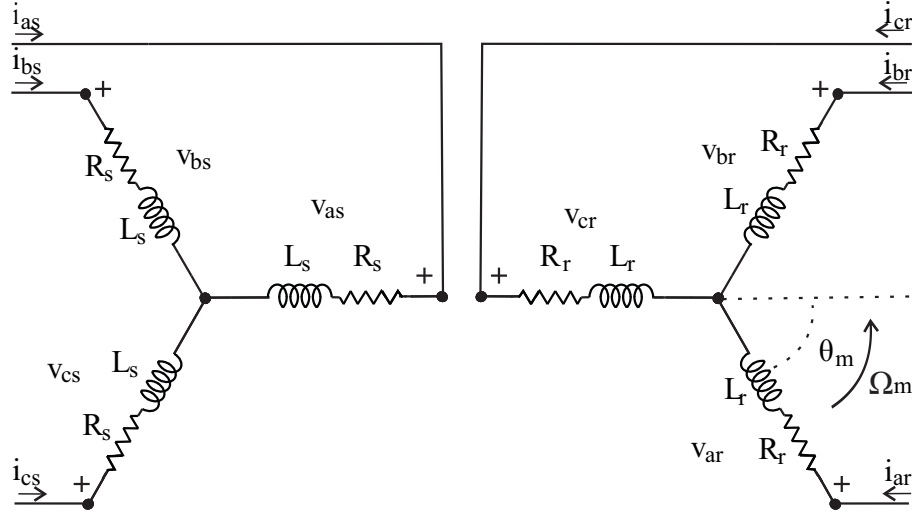


Figure 3.5: Diagram of the DFIG electrical model in abc (adapted from Taveiros (2014)).

$$v_{as} = R_s i_{as}(t) + \frac{d\lambda_{as}(t)}{dt}, \quad (3.1)$$

$$v_{bs} = R_s i_{bs}(t) + \frac{d\lambda_{bs}(t)}{dt}, \quad (3.2)$$

$$v_{cs} = R_s i_{cs}(t) + \frac{d\lambda_{cs}(t)}{dt}, \quad (3.3)$$

$$v_{ar} = R_r i_{ar}(t) + \frac{d\lambda_{ar}(t)}{dt}, \quad (3.4)$$

$$v_{br} = R_r i_{br}(t) + \frac{d\lambda_{br}(t)}{dt}, \quad (3.5)$$

$$v_{cr} = R_r i_{cr}(t) + \frac{d\lambda_{cr}(t)}{dt}, \quad (3.6)$$

in which  $i_{as}$ ,  $i_{bs}$ ,  $i_{cs}$  are stator currents respectively in phases a, b, c, and  $\lambda_{as}$ ,  $\lambda_{bs}$ ,  $\lambda_{cs}$  are stator fluxes in phases a, b, c, respectively. Furthermore,  $i_{ar}$ ,  $i_{br}$ ,  $i_{cr}$  are rotor currents respectively in phases a, b, c, and  $\lambda_{ar}$ ,  $\lambda_{br}$ ,  $\lambda_{cr}$  are rotor fluxes in phases a, b, c, respectively.

The stator variables have an synchronous angular speed  $\omega_s$  equivalent to the electrical grid frequency. However, the rotor and stator frequencies are different, wherein the rotor voltage and current have frequency dependent on the machine speed, as follows:

$$\omega_r = \omega_s - \omega_m, \quad (3.7)$$

where  $\omega_r$  is angular frequency of rotor variables and  $\omega_m$  is angular frequency of the rotor. The rotor angular frequency is obtained from a multiplication of pole pairs number ( $P$ ) versus the mechanical rotational speed at the rotor ( $\Omega_m$ ), as follow:

$$\omega_m = P\Omega_m, \quad (3.8)$$

by consequence the rotor electrical angular displacement  $\theta_r$  is given by:

$$\theta_r = P\theta_m. \quad (3.9)$$

In addition, the relationship between the synchronous angular speed and the rotor angular frequency is the machine slip ( $s_i$ ) which is obtained by:

$$s_i = \frac{\omega_s - \omega_m}{\omega_s}. \quad (3.10)$$

There is a relationship between the rotor variables angular frequency and stator angular frequency with the machine slip, which is obtained rearranging (3.7) and (3.10), as follow:

$$\omega_r = s_i\omega_s, \quad (3.11)$$

in which there is an equivalent expression relating the system frequencies:

$$f_r = s_i f_{ss}, \quad (3.12)$$

where  $f_r$  is rotor frequency and  $f_{ss}$  is stator frequency, both in hertz.

According to the machine slip, the DFIG is able to operate in three different modes, as mentioned by Abad et al. (2011):

$$\begin{aligned} \omega_m < \omega_s &\Rightarrow \omega_r > 0 \Rightarrow s_i > 0 \Rightarrow \text{Sub-synchronous operation,} \\ \omega_m > \omega_s &\Rightarrow \omega_r < 0 \Rightarrow s_i < 0 \Rightarrow \text{Super-synchronous operation,} \\ \omega_m = \omega_s &\Rightarrow \omega_r = 0 \Rightarrow s_i = 0 \Rightarrow \text{Synchronous operation.} \end{aligned}$$

The stator and rotor fluxes are given by:

$$\begin{bmatrix} \lambda_{s,abc} \\ \lambda_{r,abc} \end{bmatrix} = \begin{bmatrix} L_{s,abc} & L_{sr,abc} \\ (L_{sr,abc})^T & L_{r,abc} \end{bmatrix} \begin{bmatrix} i_{s,abc} \\ i_{r,abc} \end{bmatrix}, \quad (3.13)$$

in which  $L_{s,abc}$ ,  $L_{r,abc}$  are stator and rotor inductances to each phase a, b, c, respectively and  $L_{sr,abc}$  is the mutual inductance matrix. These matrices are defined as:

$$L_{s,abc} = \begin{bmatrix} L_{\sigma s} + M_{sr} & -\frac{1}{2}M_{sr} & -\frac{1}{2}M_{sr} \\ -\frac{1}{2}M_{sr} & L_{\sigma s} + M_{sr} & -\frac{1}{2}M_{sr} \\ -\frac{1}{2}M_{sr} & -\frac{1}{2}M_{sr} & L_{\sigma s} + M_{sr} \end{bmatrix}, \quad (3.14)$$

$$L_{r,abc} = \begin{bmatrix} L_{\sigma r} + M_{sr} & -\frac{1}{2}M_{sr} & -\frac{1}{2}M_{sr} \\ -\frac{1}{2}M_{sr} & L_{\sigma r} + M_{sr} & -\frac{1}{2}M_{sr} \\ -\frac{1}{2}M_{sr} & -\frac{1}{2}M_{sr} & L_{\sigma r} + M_{sr} \end{bmatrix}, \quad (3.15)$$



$$L_{sr,abc} = M_{sr} \begin{bmatrix} \cos(\theta_r) & \cos(\theta_r + \frac{2\pi}{3}) & \cos(\theta_r - \frac{2\pi}{3}) \\ \cos(\theta_r - \frac{2\pi}{3}) & \cos(\theta_r) & \cos(\theta_r + \frac{2\pi}{3}) \\ \cos(\theta_r + \frac{2\pi}{3}) & \cos(\theta_r - \frac{2\pi}{3}) & \cos(\theta_r) \end{bmatrix}, \quad (3.16)$$

where  $L_{\sigma_s}$ ,  $L_{\sigma_r}$  are the stator and rotor leakage inductance, respectively.  $M_{sr}$  is the mutual inductance.

The electromagnetic torque produced by the DFIG is defined as:

$$T_{em} = P \cdot i_{s,abc}^T \left[ \frac{dL_{sr,abc}}{d\theta_r} \right] i_{r,abc}, \quad (3.17)$$

and the instantaneous active power ( $P_s$ ) and the reactive power ( $Q_s$ ) which flow through stator windings are given by:

$$P_s = v_{as}i_{as} + v_{bs}i_{bs} + v_{cs}i_{cs}, \quad (3.18)$$

$$Q_s = \frac{1}{\sqrt{3}} [(v_{bs} - v_{cs})i_{as} + (v_{cs} - v_{as})i_{bs} + (v_{as} - v_{bs})i_{cs}]. \quad (3.19)$$

Furthermore, to reduce the complexity of the aforementioned model, the Park transformation is used to rearrange the model equations in a synchronous reference frame. It allows eliminating all time-varying inductances ( $L_{sr,abc}$ ) referring the stator and rotor variables to a new generic referential. This model is described in detail by Abad et al. (2011) and in subsection 3.4.2.

## 3.4 Electric Power Converter

Power converters in the back-to-back configuration are widely used in wind power generation systems. Wherein the voltage source converter (VSC), which uses a capacitor in parallel for energy storage, with two levels is the most applied topology (Yazdani and Iravani 2006) in this type of configuration. Therefore, the VSC topology with two levels is used for the development of this work. Nevertheless, there is the current source converter (CSC), which differently of VSC, uses a series inductor for energy storage.

These converters have a fundamental importance to DFIG topology because it makes an interface with the grid to ensure electric energy generation in accordance with the grid requirements. In the grid side, it is applied the GSC whereas on the rotor side it is applied the RSC, which is connected by a DC-link to GSC.

### 3.4.1 Grid Side Converter (GSC)

The GSC concerns about to maintain constant the DC-link voltage and providing a path for the rotor power as well as control the reactive and active power delivered to grid. Furthermore, this part of the back-to-back converter can be used as an active shunt filter to compensate harmonic components (Tremblay et al. 2006). In addition, it can enhance

the network power factor. Therefore, the development of a dynamic model is crucial for planning a control strategy.

Figure 3.6 illustrates a single-phase equivalent circuit of grid side in an ‘abc’ model, wherein the coupling between GSC and grid is done by an inductive filter that concerns to mitigate current oscillation.  $v_f$  is the converter output voltage,  $v_g$  is the grid voltage,  $i_g$  is the converter output current,  $L_f$  is the filter inductance on grid side, and  $R_f$  is the filter resistance on grid side.

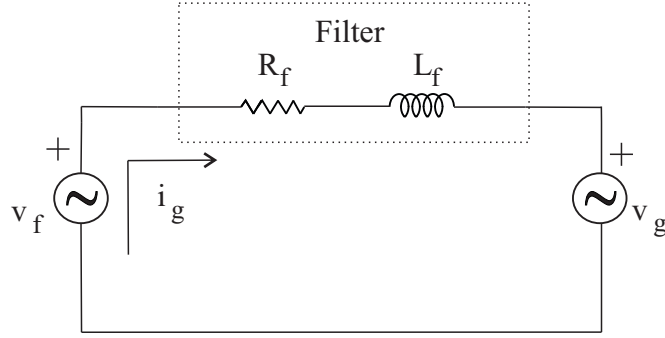


Figure 3.6: Single-phase equivalent model - grid side.

Applying Kirchhoff voltage law in Figure 3.6, it is obtained the GSC output voltage as follow:

$$v_f = R_f i_g + L_f \frac{di_g}{dt} + v_g, \quad (3.20)$$

where in a steady-state analysis the voltage  $v_f$  is equal for each system phase ‘abc’ separated to each other by a  $120^\circ$  phase displacement, thus it is assumed that (3.20) is for a three-phase system considering the phase displacement. Through Park transformation, (3.20) in ‘0dq’ plane is:

$$v_{df} = R_f i_{dg} + L_f \frac{di_{dg}}{dt} + v_{dg} - \omega_s L_f i_{qg}, \quad (3.21)$$

$$v_{qf} = R_f i_{qg} + L_f \frac{di_{qg}}{dt} + v_{qg} + \omega_s L_f i_{dg}, \quad (3.22)$$

where the zero sequence component did not appear because it was considered a balanced system as follow in Quéval and Ohsaki (2012). Moreover,  $v_{df}$  and  $v_{qf}$  are output converter voltage in  $d$  and  $q$  axis, respectively. As also,  $i_{dg}$  and  $i_{qg}$  are output converter current in ‘0dq’ plan, and  $v_{dg}$  and  $v_{qg}$  are grid voltage in  $d$  and  $q$  axis. Furthermore,  $L_f \omega_s i_{qg}$  and  $L_f \omega_s i_{dg}$  are cross elements.

For simplification criteria, it was aligned the grid voltage vector  $\vec{v}_g$  with  $d$  axis in ‘0dq’ plan, where:

$$v_{dg} = |\vec{v}_g^s|, \quad (3.23)$$

$$v_{qg} = 0, \quad (3.24)$$

in which the subscript  $s$  represents synchronous referential frame. Therefore, the simplified equations by (3.24) and (3.23) are defined as:

$$v_{df} = R_f i_{dg} + L_f \frac{di_{dg}}{dt} + v_{dg} - \omega_s L_f i_{qg}, \quad (3.25)$$

$$v_{qf} = R_f i_{qg} + L_f \frac{di_{qg}}{dt} + \omega_s L_f i_{dg}. \quad (3.26)$$

The active and reactive power delivered to grid, considering simplifications in (3.24) and (3.23), are given by:

$$P_s = \frac{3}{2} \text{Re}\{\vec{v}_g \vec{i}_g^*\} = \frac{3}{2} (v_{dg} i_{dg}), \quad (3.27)$$

$$Q_s = \frac{3}{2} \text{Im}\{\vec{v}_g \vec{i}_g^*\} = \frac{3}{2} (-v_{dg} i_{qg}), \quad (3.28)$$

where there is a current decoupling in dq components, which the current  $i_{dg}$  is used to calculate  $P_g$  and the current  $i_{qg}$  is used to calculate  $Q_g$ .

By the GSC equation model it is possible to develop control system strategies to control the DC-link voltage, active and reactive power injection. In this work it was implemented the cascade PI-based control which is found in details in (Abad et al. 2011), (Pena et al. 1996) and (Quéval and Ohsaki 2012).

### 3.4.2 Rotor Side Converter (RSC)

The RSC supplies the machine rotor and it connects with GSC by a DC-link. Furthermore, this element concerns about to control active and reactive power delivered to the electrical system from the generator, electromagnetic torque and adjusts voltage amplitude, phase, and frequency introduced into the rotor (Abad et al. 2011). In addition, RSC is able to control the rotor machine speed and eliminate significant harmonic current components (Boutoubat et al. 2017).

Figure 3.7 illustrates a single-phase equivalent circuit of DFIG in a 'dq' model with neglected stator resistances used to develop the control system. Therefore, the machine behavior will be known and will be possible to develop its control through RSC.  $L_m$  is the magnetizing inductance,  $v_{dr}$  and  $v_{qr}$  are rotor voltages in dq reference,  $i_{dr}$  and  $i_{qr}$  are rotor currents in dq reference,  $\lambda_{dr}$  and  $\lambda_{qr}$  are rotor fluxes in d and q reference frame, respectively. Finally  $\lambda_{ds}$  and  $\lambda_{qs}$  are stator fluxes in dq reference.

The stator flux is aligned with the d-coordinate in the reference frame 'dq' whereas the q coordinate is canceled, thus  $\lambda_{qs} = 0$ . In addition, stator voltage is aligned with q-coordinate, whereas  $v_{ds} = 0$  (Abad et al. 2011). Therefore, rotor voltage is given by:

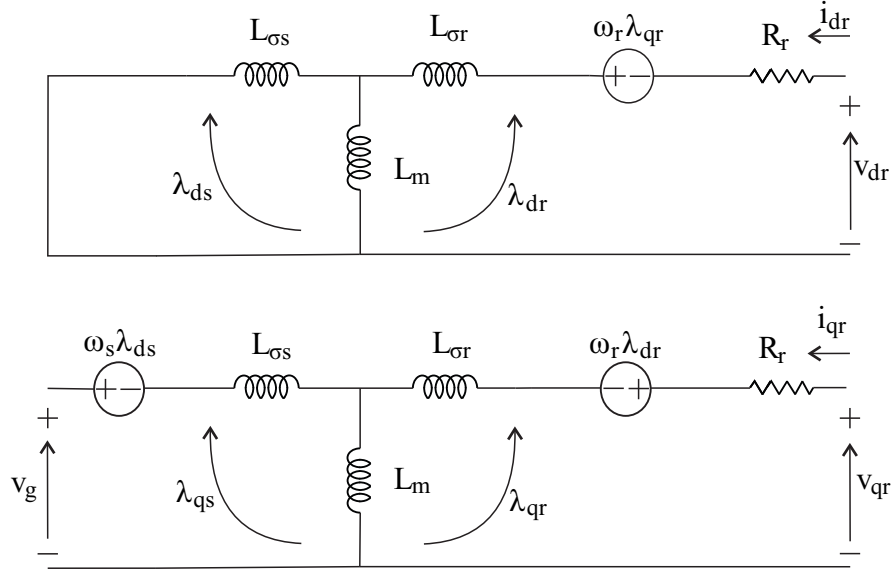


Figure 3.7: Single-phase equivalent model in dq - rotor side.

$$v_{dr} = R_r i_{dr} - \omega_r \lambda_{qr} + \frac{d\lambda_{dr}}{dt}, \quad (3.29)$$

$$v_{qr} = R_r i_{qr} + \omega_r \lambda_{dr} + \frac{d\lambda_{qr}}{dt}. \quad (3.30)$$

The relation between rotor current and magnetic flux is defined as follow:

$$\lambda_{dr} = \underbrace{\left( L_r - \frac{L_m^2}{L_s} \right)}_{\sigma L_r} i_{dr} + \frac{L_m}{L_s} \lambda_{ds}, \quad (3.31)$$

$$\lambda_{qr} = \underbrace{\left( L_r - \frac{L_m^2}{L_s} \right)}_{\sigma L_r} i_{qr}, \quad (3.32)$$

in which  $\sigma$  is leakage coefficient.

Rewriting (3.29) and (3.30), rotor voltage and current relations are obtained as follow:

$$v_{dr} = R_r i_{dr} - \omega_r \sigma L_r i_{qr} + \sigma L_r \frac{di_{dr}}{dt} + \frac{L_m}{L_s} \frac{d\lambda_{ds}}{dt}, \quad (3.33)$$

$$v_{qr} = R_r i_{qr} + \omega_r \sigma L_r i_{dr} + \sigma L_r \frac{di_{qr}}{dt} + \omega_r \frac{d\lambda_{ds}}{dt}. \quad (3.34)$$

According to Abad et al. (2011), the last term in (3.33) is neglected, whereas the last term in (3.34) is a system perturbation. Furthermore, such as appear in GSC model equation, there are cross terms  $-\omega_r \sigma L_r i_{qr}$  and  $\omega_r \sigma L_r i_{dr}$ .

The active and reactive power which is delivered to the grid is defined as:

$$P_s = \frac{3}{2} v_{qs} i_{qs}, \quad (3.35)$$

$$Q_s = \frac{3}{2} v_{qs} i_{ds}. \quad (3.36)$$

In addition, the electromagnetic torque is given by:

$$T_{em} = -\frac{3}{2} p \frac{L_m}{L_s} \frac{V_g}{\omega_s L_s} i_{qr}. \quad (3.37)$$

By (3.29) until (3.37) that represent the DFIG model in '0dq' reference frame is used to obtain the transfer functions applied to develop the control system strategies to control the active and reactive power injection, machine speed and electromagnetic torque by the RSC. In this work it was implemented the cascade PI-based control which is found in details in (Abad et al. 2011), (Pena et al. 1996) and (Quéval and Ohsaki 2012).

### 3.5 Protection Challenges

DFIG presents an intrinsic disadvantage due to its stator be directly connected to the grid: the sensitivity to any abrupt drop of the grid voltage, for instance, symmetrical or asymmetrical electrical fault or a voltage dip make the back electromotive force oscillate and generate an electromagnetic torque pulsation. Besides that aspect, rotor power flow direction can be positive or negative depending on the machine operation mode, machine speed can oscillate from the sub-synchronous to the super-synchronous, rotor and stator electric variables have different frequencies, rotor winding frequency is low and variable, and there is magnetic coupling between rotor and stator windings (Mansouri et al. 2016). Due to these characteristics, to develop and standardize electrical protections to the DFIG is a challenge.

The ongoing growth of the WECS insertion in the electrical grid and the grid code requirements imposed by system operators required modifications in the protection methods due to the peculiar characteristics of these systems, especially when it comes to DFIG. Moreover, some criteria such as voltage support, frequency maintenance, and continuity of connectivity in cases of stator voltage sags must be achieved for electrical grids with DFIG's such as applied to conventional synchronous power generators (Comech et al. 2011). Furthermore, achieve the grid requirements is fundamental to avoid grid blackout, and allow the capacity of load flow controlling and keep working properly the interconnected electrical system, because the grid code objectives should ensure a safe, reliable, and economical operation of the power system.

Currently, protection schemes are used to guarantee the LVRT. For instance, protections such as overcurrent and sub-voltage have been used to detect grid disturbances and

electrical faults on the PCC to trigger some LVRT categories. However, there is no standardization (Mansouri et al. 2016).

### 3.5.1 Protections Against External Faults and LVRT Enhancement

The LVRT, also known as fault-ride through (FRT), which is the support for the grid in case of faults and voltage sags, has been gaining a lot of attention in countries that started to use WECS more expressively as a source of energy. Then, the grid operators require that any generator to have the ability to remain connected during the whole fault duration, such as illustrated in Figure 3.8 (Comech et al. 2011) wherein depicts the voltage sag level supported by each grid code of different countries, as well as to offer support to the grid in order to attempt to restore the voltage level.

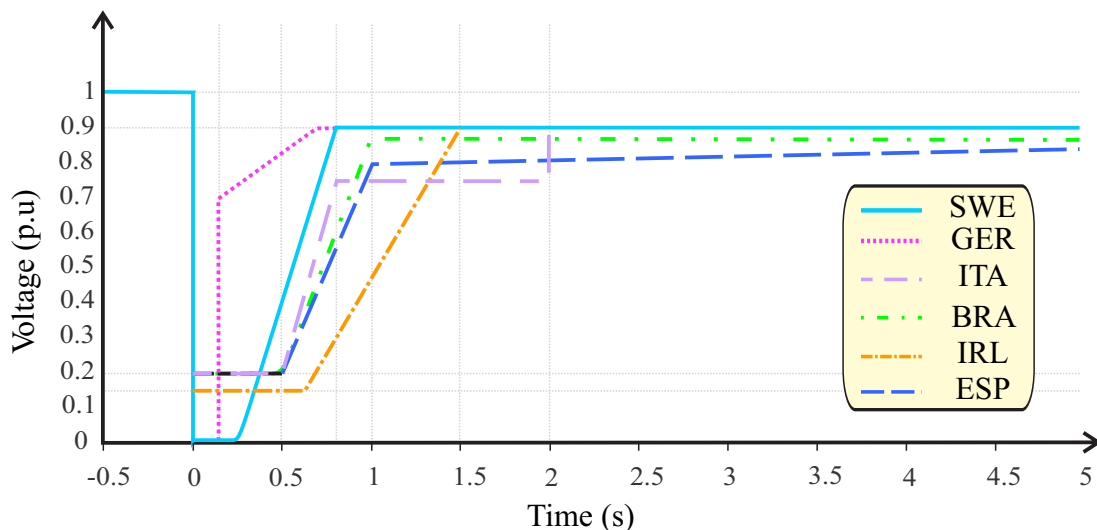


Figure 3.8: LVRT requirements in different countries (adapted from Comech et al. (2011)).

Some strategies were created to guarantee the LVRT and the protection of DFIG elements against overcurrent, overvoltage and undervoltage caused by external faults at the PCC. These strategies are subdivided into categories: hardware modification, superconducting fault current limiter and control improvement for DFIG converters (Zou et al. 2016). Therefore, the most used LVRT categories applied in wind farms are described in the remainder of this section, evidencing factors such as efficiency, economical cost, reliability, accuracy, and practical application.

When dealing with faults outside the generator, the most applied detection schemes are based on voltage monitoring, power flow direction, and current monitoring. Furthermore, these detection schemes are used to trigger some LVRT categories, and so to activate the protection circuit switches and to change the control strategy. Therefore, the overcurrents and overvoltages present in DFIG components caused by grid disturbances in the PCC will be decreased.

Table 3.1 illustrates a comparison among the LVRT categories present in the literature nowadays. In this comparison it is addressed the advantages and disadvantages of each category briefly. It was considered the aspects of whether the category is able or not to protect the generator against external faults and if it is needed a trigger to activate or deactivate the category in case of fault detection.

Table 3.1: DFIG protection against external faults and LVRT enhancement strategies (adapted from Justo et al.(2015)).

LVRT categories	Advantages	Diadvantages
<b>Hardware modification:</b>		
<ul style="list-style-type: none"> <li>• Protection circuits</li> </ul>	<ul style="list-style-type: none"> <li>• Easy to implement</li> <li>• Useful under deep voltage sags</li> <li>• Useful under symmetrical, asymmetrical grid faults</li> <li>• Protect the DFIG</li> <li>• Decrease overcurrent and torque oscilation</li> </ul>	<ul style="list-style-type: none"> <li>• Reduce the system reliability</li> <li>• Add extra hardware</li> <li>• Need a trigger</li> </ul>
<ul style="list-style-type: none"> <li>• Reactive power devices</li> </ul>	<ul style="list-style-type: none"> <li>• Decrease rotor current</li> <li>• Useful for all transient types</li> <li>• Voltage support</li> </ul>	<ul style="list-style-type: none"> <li>• Increase the complexity</li> <li>• Need a trigger</li> <li>• Do not protect the DFIG</li> </ul>
<b>Control strategies</b>		
	<ul style="list-style-type: none"> <li>• Do not require extra hardware</li> <li>• Do not increase the system cost</li> <li>• Partial DFIG protection</li> <li>• Decrease overcurrent</li> </ul>	<ul style="list-style-type: none"> <li>• Only useful under moderate voltage sags</li> <li>• Need a trigger</li> <li>• Difficult to implement</li> </ul>
<b>Superconducting materials:</b>		
<ul style="list-style-type: none"> <li>• Resistive type</li> <li>• Inductive type</li> </ul>	<ul style="list-style-type: none"> <li>• Do not need a trigger</li> <li>• Protect the DFIG</li> <li>• Smooth the unsteady output power (inductive type)</li> </ul>	<ul style="list-style-type: none"> <li>• High implementation costs</li> <li>• Difficult to design in practical applications</li> </ul>

### Hardware modification

Hardware modifications are used to protect DFIG elements, such as DC-link, power converters, rotor and stator windings, against electrical disturbances in the PCC. The faults which occur in this point can cause overcurrent in the rotor side, overvoltage in DC-link, mechanical pulsation and others losses which damaging DFIG assembly. Hence, many strategies to avoid these situations were created, among that, there are crowbar circuit, DC-link chopper, series dynamic resistor (SDR) and reactive power inject de-

vices (Justo et al. 2015). In addition, there are recent studies that uses superconducting materials and storage system to overcome these problems, such as (Zarei et al. 2018) and (Xiao et al. 2018).

The crowbar protection acting principle consists in power dissipation in moments of voltage sag in the electrical grid by rotor current deviation for the crowbar resistors protecting the RSC and the rotor windings against overcurrent. The crowbar topologies can be passive or active (Abad et al. 2011). The active topology is based on insulated gate bipolar transistor (IGBTs), controlled by pulse width modulation (PWM) or another control tactics making the resistors fully controllable with a better performance than the passive crowbar. In addition, this protection is able to be connected in series to the stator winding or in parallel to the rotor winding. However, the last one is the most used.

This protection actuation occurs in cases of overcurrent in the rotor, overvoltage in the DC link or voltage sags in the stator (Abad et al. 2011). Therefore, detection methods such as techniques based on genetic algorithm, logical fuzzy and neural networks are used to trigger the crowbar switches in case of a fault at PCC. Furthermore, detection methods based on some relay protections, for instance, overcurrent and undervoltage are used to do this detection.

There are other protective circuits applied on DFIG assembly, such as the DC-chopper (Justo et al. 2015) which is coupled in the DC link in case of an overvoltage detection. Furthermore, there are protective circuits with the crowbar associated with SDR and the crowbar associated with the DC-Chopper.

Another proposition is the reactive power injecting-device. The generator magnetization in the normal way is done over the rotor circuit by the rotor-side converter. However, in the case of an electrical fault, this magnetization is done by the stator in case of the rotor excitation to be disconnected. Therefore, the generator will consume reactive power from the electrical grid. Thus, this compensation is used for improving the voltage in PCC. Some devices which inject reactive power are the DVRs, the reactive power compensator such as the static synchronous compensator (STATCOM) or the static var compensator (SVC).

Installation of the aforementioned injecting-devices with a proper control strategy ensures the LVRT and minimizes the grid fault effects to the DFIG (Justo et al. 2015). However, another strategy is presented in Hansen et al. (2007) which the RSC is reconfigured in parallel with the GSC in the case of electrical fault occurrence, where the crowbar is activated too. On this assembly, both converters are responsible for supply the reactive compensation.

### **Control improvement for DFIG converters**

Nowadays many studies of new control schemes have been developed for assuring grid codes. Due to some drawbacks present in hardware modification, for instance, when a crowbar circuit is used the RSC is temporarily disabled which leads to a partial power control loss and when the fault is cleared appears huge transients (Vrionis et al. 2014). In addition, when a reactive power inject device is used the economical cost increase making it inapplicable in some situations. Therefore, control methods have appeared to strike these disadvantages.



There are many advanced control strategies proposed in the literature, some of them are based on negative sequence components of stator flux linkage, flux linkage tracking-based control, virtual resistance in combination with demagnetization control (Vrionis et al. 2014). Furthermore, adaptive controls, controls with optimal adjustments for the controller's parameters, predictive controls and strategies based on resonant control were also proposed.

The main advantage of this category is the non-use of additional hardware which reduce economical costs and decrease torque oscillation and rotor overcurrent. Notwithstanding, this strategy is useful only under moderate voltage sags and in case of symmetrical faults. In addition, this category is hard to be implemented in practical applications (Justo et al. 2015).

### **Superconducting fault current limiter**

In some applications, superconducting materials are used in order to limit fault rotor current, dc-link voltage and torque pulsation in order to achieve grid codes requirements. Furthermore, the superconducting category has some advantages, such as do not need a trigger to activate the category insertion into the system because it is constantly connected in the DFIG system.

This category is subdivided in the resistive superconducting elements and the inductive superconducting elements. The second one is able to face two problems simultaneously, which are the protection of DFIG elements and to solve the output power instability, once this category is capable to store energy (Guo et al. 2016). However, the resistive type is able only to protect the DFIG topology. Notwithstanding, whether a battery is placed in association with this superconducting type it will be able to solve the DFIG system instability too.

There are some drawbacks in this category, for instance: high initial investment costs which will be recovered over the years, the current researches have been made only by simulation studies and the complex electrical topologies. Furthermore, in some cases it is hard to find the superconducting proposed material in market.

## **3.5.2 Internal Protections**

There is no standardization to protections applied to DFIG against internal faults (Mansouri et al. 2016). However, in recent studies, the current differential protection was proposed to be used in this wind generator topology. Mansouri et al. (2016) explain about a conventional phasor-based differential protection in which some adaptations were done considering the machine slip and the rotor angle. Furthermore, Zarei et al. (2018) proposed a time domain differential protection using the Park transformation. Despite this, the research field about protection methods applied to DFIG continues scarce.

A survey at Germany wind farms in 2009 detected that 23.5% of wind turbine downtime was because of generator failures (Abadi et al. 2014), whereas in another survey, the percentage of fault types are: 38% of stator fault, 10% of rotor fault, 40% bearing failures (Kia et al. 2013). Therefore, to develop protection and detection methods is important to prevent unplanned downtimes, detect incipient faults in a early stage in order

to minimize maintenance costs and provide maximum operation continuity. Figure 3.9 illustrates some stator and rotor winding fault types.

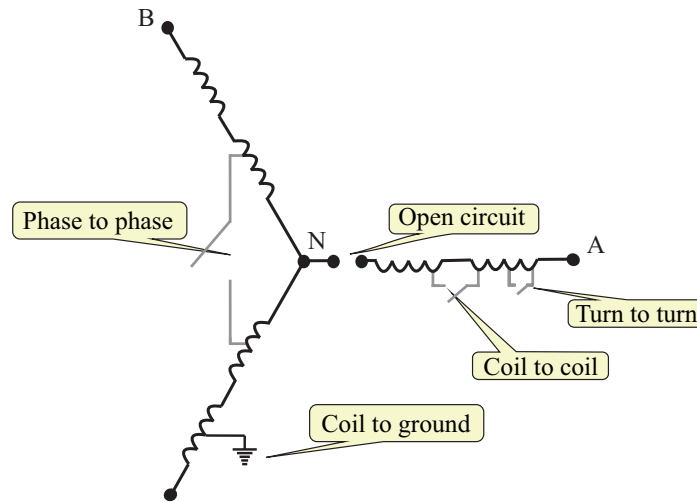


Figure 3.9: DFIG internal faults types - Winding faults types.

As illustrated in Figure 3.9, internal faults are open-circuit, phase-to-phase, coil-to-ground, coil-to-coil, and turn-to-turn faults, which are susceptible to occur in the rotor windings as well as in the stator windings. Furthermore, there are the winding resistive asymmetrical fault (WRAF) (Roshanfekar and Jalilian 2016) and faults involving the machine interconnection point, which is more commonly at the rotor side due to the brushes. Moreover, beyond these aforementioned faults internal to the DFIG topology, power converter faults are also considered as DFIG internal faults because they are inside the topology. Figure 3.10 summarizes all possible fault points present inside the DFIG set. Furthermore, in this work were analyzed faults which occurred in the DFIG feed point with the stator windings using real experimental data.

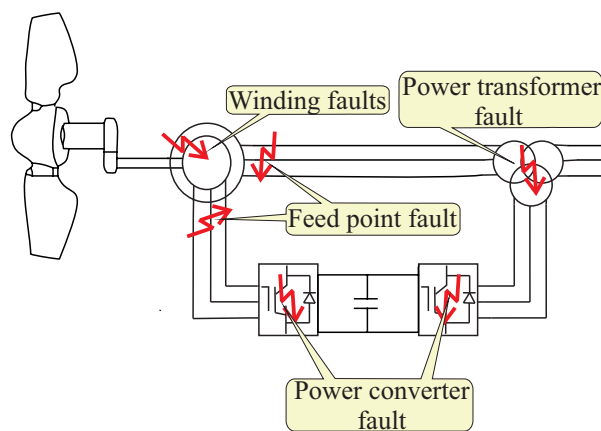


Figure 3.10: DFIG internal faults location.

The faults shown in Figure 3.9 occur by many reasons, some of them are abnormal connections, static and/or dynamic air-gap eccentricities (Kia et al. 2013), insulation degradation between the individual coil, insulation degradation between different coils, thermal overload which can cause demagnetization of permanent magnet in case of PMSG and electromechanical-induced vibration.

### **3.6 Summary**

In this chapter, the main characteristics of the WECS and the DFIG topology were discussed, addressing the essential components in the operation of these systems. The main protection challenges were described, as well as the aspects related to internal and external protection schemes, advantages and disadvantages.

---

# Chapter 4

## Mathematical Fundamentals

---

Developing signal processing in the time domain is complex and dense in mathematical processing. In this fashion, laying hands on mathematical tools which transform the signal to another domain is useful to analyze aspects which are not easily visible in the conventional domain. Therefore, introductory concepts about the Fourier transform and the wavelet transform will be addressed. In addition, different versions of the wavelet transform will be covered, such as the stationary wavelet transformer with boundary effects.

### 4.1 Fourier Transform

The integral Fourier transform, developed by Jean-Baptiste Joseph Fourier in the nineteenth century, decomposes a periodic temporal function into frequencies in a sinusoidal base (sine and cosine). Also, it is called representation in the frequency domain of a signal. The transform is defined as follow:

$$F(\omega) = \int_{-\infty}^{\infty} f(t)e^{-j\omega t} dt, \quad (4.1)$$

where  $t$  and  $\omega$  are time and frequency assignments, respectively;  $f(t)$  is the time-domain signal and  $F(\omega)$  is the frequency-domain signal. For many functions, it is possible to define a reversal operation, known as the inverse Fourier transform, defined as:

$$f(t) = \frac{1}{2\pi} \int_{-\infty}^{\infty} F(\omega)e^{-j\omega t} dt. \quad (4.2)$$

Fourier transform has a wide field of application, e.g. signal processing, statistics, and encryption. In the context of electrical power systems, the discrete Fourier transform was used by Arun G. Phadke (2008) to developed a real-time phasor estimation given by:

$$X_r(k) = \frac{2}{\Delta k} \sum_{n=k-\Delta k+1}^k x(k) \left\{ \cos \frac{2\pi n}{\Delta k} \right\}, \quad (4.3)$$

$$X_i(k) = \frac{2}{\Delta k} \sum_{n=k-\Delta k+1}^k x(k) \left\{ \sin \frac{2\pi n}{\Delta k} \right\}, \quad (4.4)$$

in which  $X_r$  and  $X_i$  is the real and imaginary phasor components, respectively;  $\Delta k = f_s/f$  is the total number of samples, wherein  $f_s$  is sampling frequency and  $f$  is the system fundamental frequency;  $x(k)$  is a sample of the original signal in time. The module ( $|X(k)|$ ) and the angle ( $\angle X(k)$ ) is defined as:

$$|X(k)| = \sqrt{X_r(k)^2 + X_i(k)^2}, \text{ and} \quad (4.5)$$

$$\angle X(k) = \tan^{-1} \left( \frac{X_i(k)}{X_r(k)} \right). \quad (4.6)$$

In order to reduce the computational effort, the recursive version of this algorithm is used in this work (Arun G. Phadke 2008), as follow:

$$X_r(k) = X_r(k-1) + (x(k) - x(k-\Delta k)) \left\{ \cos \frac{2\pi n}{\Delta k} \right\}, \quad (4.7)$$

$$X_i(k) = X_i(k-1) + (x(k) - x(k-\Delta k)) \left\{ \sin \frac{2\pi n}{\Delta k} \right\}. \quad (4.8)$$

Therefore, the calculation of the last phasor element ( $X_r$  and  $X_i$ ) is availed; after that, it is taken out the oldest calculated sample contribution ( $x(k-\Delta k)$ ). Finally, it is added the most recent calculated sample  $x(k)$ .

## 4.2 Wavelet Transform

The wavelet transform conceptualization is derived from the Haar transform (Haar 1910). However, only some decades later a mathematical definition of wavelet transform was developed, wherein Grossmann and Morlet (1984) defined a continuous wavelet transform (CWT) in which was stated that a signal is able to be transformed and recovered without loss of information. Thereafter, Mallat (1989) proposed a wavelet transform with the multi-resolution analysis, and Daubechies (1992) proposed the DWT concepts. The stationary wavelet transform (SWT) was also proposed, which is a variation of the DWT. Nowadays, the wavelet transform is used in different research fields, e.g. numbers theory, image processing and electric power systems. Furthermore, due to the wavelet transform is sensitive to high-frequency content, the application of this transform is suitable for analysis of transients present in electric machines during an electrical fault moment.

### 4.2.1 Discrete Wavelet Transform

From the multi-resolution analysis proposed by Mallat (1989) it is possible to decompose a discrete signal into scaling ( $s$ ) and wavelet ( $w$ ) coefficients, at different levels of decomposition, as follows:

$$s_j(k) = \sum_{n=-\infty}^{\infty} h_{\phi}(n-2k)s_{j-1}(n), \quad (4.9)$$

$$w_j(k) = \sum_{n=-\infty}^{\infty} h_{\psi}(n-2k)s_{j-1}(n), \quad (4.10)$$

in which  $j \geq 1$ ,  $h_{\phi}$  and  $h_{\psi}$  is the low-pass (scaling filter) and high-pass (wavelet filter) filters, respectively;  $s_j$  and  $w_j$  are the scaling and wavelet coefficients, respectively, at the  $j$ <sup>th</sup> decomposition level. The coefficients  $s_j$  and  $w_j$  are obtained by the convolution of the scaling coefficients  $s_{j-1}$ , of the decomposition level  $j-1$ , with the filters  $h_{\phi}$  and  $h_{\psi}$ , respectively. Thereafter, the coefficients are sub-sampled by two and the filters output have their frequency ranges equal to half of the original signal ( $s_{j-1}$ ) (Polikar 1996). In the first decomposition level  $j = 1$ , thus  $s_{j-1} = s_0$ , therefore,  $x = s_0$ , wherein  $x$  is the original signal.

Figure 4.1 depicts the decomposition process in two decomposition levels, wherein the symbol  $\downarrow 2$  represents the sub-sampling by two. The signal  $x$  is decomposed into the wavelet ( $w_1$ ) and scaling ( $s_1$ ) coefficients in the first decomposition level ( $j = 1$ ) by the high- and low-pass filters followed by a sub-sampling by 2. The coefficients  $w_1$  are related to high frequency components of the signal  $x$ , whereas the coefficients  $s_1$  are related to low frequency components.

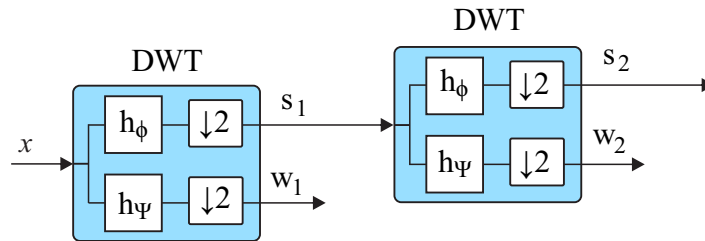


Figure 4.1: Block diagram depicting the two first decomposition levels of DWT.

In next decomposition level ( $j = 2$ ) the same process aforementioned is repeated. However, now the input signal is the first decomposition level scaling coefficient ( $s_1$ ), due to having approximated information of the original signal because it is the low-pass filter response. Therefore, for the next decomposition levels, the same process is repeated and repeated until the end of decomposition levels. Due to the sub-sampling process, the number of samples is halved each time that passes through a new decomposition level.

## 4.2.2 Stationary Wavelet Transform (SWT)

The name stationary refers to the fact that the SWT does not make the process of sub-sampling by two in the input signal samples, making the SWT invariant to the circular displacements in the samples in opposite to the DWT, which make this transform able to be applied for any samples number, since that  $N > L$ , in which  $N$  is total sample number and  $L$  is number of scaling and wavelet filter coefficients. Furthermore, SWT is the most appropriate version of the wavelet transform for real-time fault detection applications (Costa et al. 2010) because it can be applied in all samples. Due to this transform is time-invariant, always has the same number of samples, which provides significant gains in transient analysis, fault detection, and classification (Costa 2014), and it is non-orthogonal due to has different scales and to be shifted in time. Moreover, this transform is also known as maximal overlap discrete wavelet transform (MODWT).

Figure 4.2 depicts the SWT decomposition process in two decomposition levels. The signal  $x$  is decomposed into the wavelet ( $w_1$ ) and scaling ( $s_1$ ) coefficients in the first decomposition level ( $j = 1$ ) by the high- and low-pass filters. The coefficients  $w_1$  are related to high frequencies components of the signal  $x$ , whereas the coefficients  $s_1$  are related to low frequencies components.

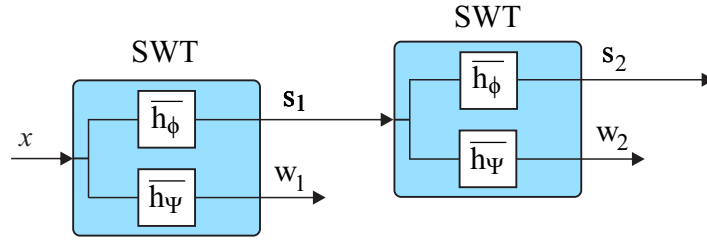


Figure 4.2: Block diagram depicting the two first decomposition levels of SWT.

The process repeats in whole follow levels ( $j = 2$ ) and so on. However, such as in DWT, the input signal for the next decomposition levels are the scaling coefficients of the previous one, which contains the low-frequency components, due to the scaling coefficients are an approximation of the original signal.

The input signal of each decomposition level with finite sample number ( $N$ ) is given by:

$$s_j = \{s_j(0), s_j(1), \dots, s_j(N)\}, \quad (4.11)$$

in which  $j \geq 0$  and  $N \geq L$ ; wherein the SWT scaling and wavelet coefficients are given by:

$$s_j(k) = \frac{1}{\sqrt{2}} \sum_{n=-\infty}^{\infty} h_\phi(n-k) s_{j-1}(n), \quad (4.12)$$

$$w_j(k) = \frac{1}{\sqrt{2}} \sum_{n=-\infty}^{\infty} h_\psi(n-k) s_{j-1}(n). \quad (4.13)$$

A periodic extension of the signal  $s_j$ , which makes a signal of finite duration in an infinite duration signal, is defined as follows:

$$\dot{s}_j(n + pN) = s_j(n), \quad (4.14)$$

in which  $0 \leq n \leq N$  and  $p$  is any number within the set of integers. Therefore, the discrete scaling and wavelet coefficients with finite duration is given by:

$$s_j(k) = \frac{1}{\sqrt{2}} \sum_{l=0}^{L-1} h_\varphi(l) \dot{s}_{j-1}(k+l), \quad (4.15)$$

$$w_j(k) = \frac{1}{\sqrt{2}} \sum_{l=0}^{L-1} h_\psi(l) \dot{s}_{j-1}(k+l), \quad (4.16)$$

where  $j \geq 1$ ;  $0 \leq k \leq N$ ;  $N \geq L$  and  $\dot{s}$  is the discrete input signal with periodic extension.

### 4.2.3 Real-Time Boundary Stationary Wavelet Transform

Figures 4.3(a) illustrates a signal with a sliding window  $\Delta k = 20$  samples, where is depicted the recursive wavelet coefficients calculus of SWT using Daubechies db(4). However, using the pyramidal algorithm, neither all wavelet coefficients corresponds to the coefficients of the sliding window signal, as depicted in Figure 4.3(c). The last  $\Delta k - L + 1$  coefficients of the wavelet sliding window (Figure 4.3(b)) and those calculated using the pyramidal algorithm (Figure 4.3 (c)) are exactly the same, whereas the first  $L - 1$  coefficients of the two windows are different.

For real-time implementation, it is necessary to add the  $(L - 1)$  coefficients with boundary effect. In this fashion, Costa (2014) proposed decomposition of a sliding window considering the  $(L - 1)$  coefficients with boundary effect.

The coefficients with boundary effect are calculated with the first and last  $L - 1$  samples of a signal sliding window, as follow:

$$s_j(z, k) = \frac{1}{\sqrt{2}} \sum_{l=0}^{L-1} h_\varphi(l) \dot{s}_{j-1}(k - L + l + z + 1), \quad (4.17)$$

$$w_j(z, k) = \frac{1}{\sqrt{2}} \sum_{l=0}^{L-1} h_\psi(l) \dot{s}_{j-1}(k - L + l + z + 1), \quad (4.18)$$

in which  $z$  corresponds to the boundary level, which vary according to  $0 \leq z < L - 1$ .  $L$  is the size of the filters;  $\Delta k \geq L$  is the size of the sliding window.

### 4.2.4 Scaling and wavelet filters

The filters are mirror-quadrature. Therefore,  $h_\varphi$  and  $h_\psi$  are defined as:



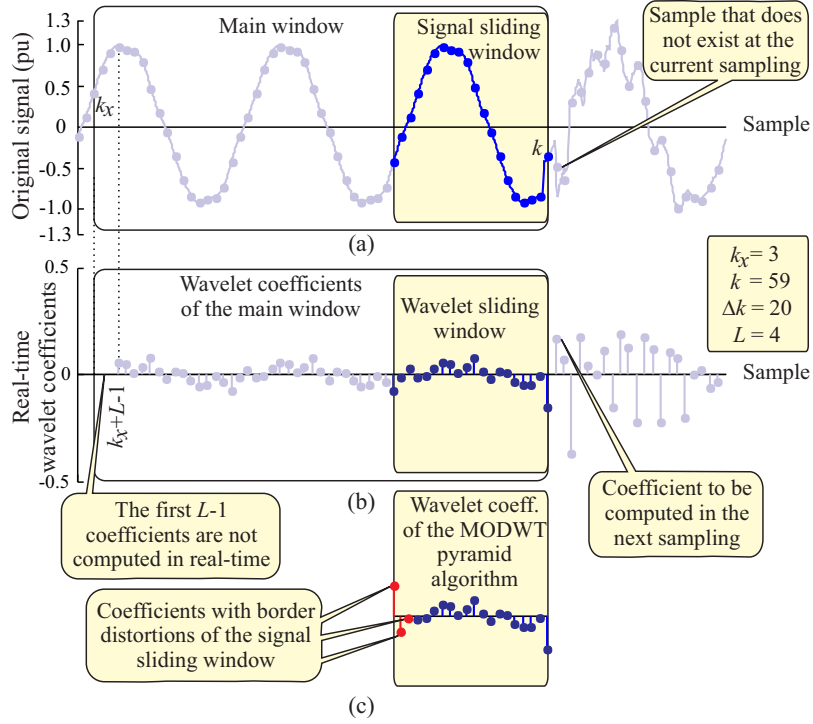


Figure 4.3: Real-time computation of the wavelet coefficients: (a) original signal, (b) wavelet coefficients of the recursive MODWT, (c) wavelet coefficients of the MODWT pyramid algorithm related to the signal sliding window (adapted from Costa (2014)).

$$h_{\varphi}(l) = h_{\varphi}(L-l-1), \quad (4.19)$$

$$h_{\psi}(l) = h_{\psi}(L-l-1), \quad (4.20)$$

in which:

$$h_{\varphi} = \{h_{\varphi}(0), h_{\varphi}(1), \dots, h_{\varphi}(L-2), h_{\varphi}(L-1)\} = \{-h_{\psi}(L-1), h_{\psi}(L-2), \dots, -h_{\psi}(1), h_{\psi}(0)\},$$

$$h_{\psi} = \{h_{\psi}(0), h_{\psi}(1), \dots, h_{\psi}(L-2), h_{\psi}(L-1)\} = \{h_{\varphi}(L-1), h_{\varphi}(L-2), \dots, h_{\varphi}(1), -h_{\varphi}(0)\}.$$

According to Percival and Walden (2000), the filter coefficients have the following properties:

$$\sum_{l=0}^{L-1} [h_{\psi}(l)]^2 = 1 \rightarrow \sum_{l=0}^{L-1} [h_{\varphi}(l)]^2 = 1, \quad (4.21)$$

$$\sum_{l=0}^{L-1} h_{\psi}(l)h_{\psi}(l+2p) = 0 \rightarrow \sum_{l=0}^{L-1} h_{\varphi}(l)h_{\varphi}(l+2p) = 0, \quad (4.22)$$

$$\sum_{l=0}^{L-1} h_{\Psi}(l) = 0 \rightarrow \sum_{l=0}^{L-1} h_{\Phi}(l) = \sqrt{2}, \quad (4.23)$$

where  $l = 0, 1, \dots, L - 1$ .

The mother wavelet determines the wavelet and scaling filter coefficients. For instance, the filter coefficients used in this work are associated to the the mother wavelet Daubechies db (4), in which  $L = 4$ , given by:

$$h_{\Phi}(0) = \frac{1 + \sqrt{3}}{4\sqrt{2}}, \quad h_{\Phi}(1) = \frac{3 + \sqrt{3}}{4\sqrt{2}}, \quad h_{\Phi}(2) = \frac{3 - \sqrt{3}}{4\sqrt{2}}, \quad h_{\Phi}(3) = \frac{1 - \sqrt{3}}{4\sqrt{2}}, \quad (4.24)$$

$$h_{\Psi}(0) = \frac{1 - \sqrt{3}}{4\sqrt{2}}, \quad h_{\Psi}(1) = \frac{-3 + \sqrt{3}}{4\sqrt{2}}, \quad h_{\Psi}(2) = \frac{3 + \sqrt{3}}{4\sqrt{2}}, \quad h_{\Psi}(3) = \frac{-1 - \sqrt{3}}{4\sqrt{2}}. \quad (4.25)$$

#### 4.2.5 Energy of the Scaling and Wavelet Coefficients with Boundary Effect.

The spectral energy of a signal ( $\epsilon$ ) is able to be decomposed by the scaling ( $\epsilon^s$ ) and wavelet ( $\epsilon^w$ ) coefficient energy according to Costa (2014), as follow:

$$\epsilon(k) = \epsilon^s(k) + \epsilon^w(k), \quad (4.26)$$

in which  $\epsilon^s$  and  $\epsilon^w$  are given by:

$$\epsilon^s(k) = \epsilon^{sa}(k) + \epsilon^{sb}(k), \quad (4.27)$$

$$\epsilon^w(k) = \epsilon^{wa}(k) + \epsilon^{wb}(k), \quad (4.28)$$

for  $k > \Delta k - 1$ . The components  $\epsilon^{sa}$  and  $\epsilon^{wa}$  are due to the scaling and wavelet coefficients with boundary effect of the signal samples within the sliding window, as follows:

$$\epsilon^{sa}(k) = \sum_{l=1}^{L-1} s^2(l, k), \quad (4.29)$$

$$\epsilon^{wa}(k) = \sum_{l=1}^{L-1} w^2(l, k), \quad (4.30)$$

for  $k > \Delta k - 1$ . Finally,  $\epsilon^{sb}$  and  $\epsilon^{wb}$  components are due to the scaling and wavelet coefficients without boundary effect, given by:

$$\epsilon^{sb}(k) = \sum_{l=k-\Delta k+L}^k s^2(l, k), \quad (4.31)$$

$$\epsilon^{wb}(k) = \sum_{l=k-\Delta k+L}^k w^2(l, k). \quad (4.32)$$

According to Costa (2014), the energy  $\epsilon^{wb}$  is influenced by high-frequency noise and electromagnetic transients, whereas,  $\epsilon^w = \epsilon^{wa} + \epsilon^{wb}$  is also influenced by high-frequency noise and electromagnetic transients and the sliding window boundary effects. Therefore, the wavelet coefficient energy with boundary effect are higher than the wavelet coefficient energy without boundary effect. However, the scaling coefficient energy with and without boundary effects have a similar behavior. Nevertheless,  $\epsilon^s$  does not present time delay associated to the mother wavelet.

Figure 4.4 illustrates a comparison between the SWT and BSWT, in which the Figure 4.4(a) shows a current signal ( $i$ ) with a fault in the sample  $k = 680$ .

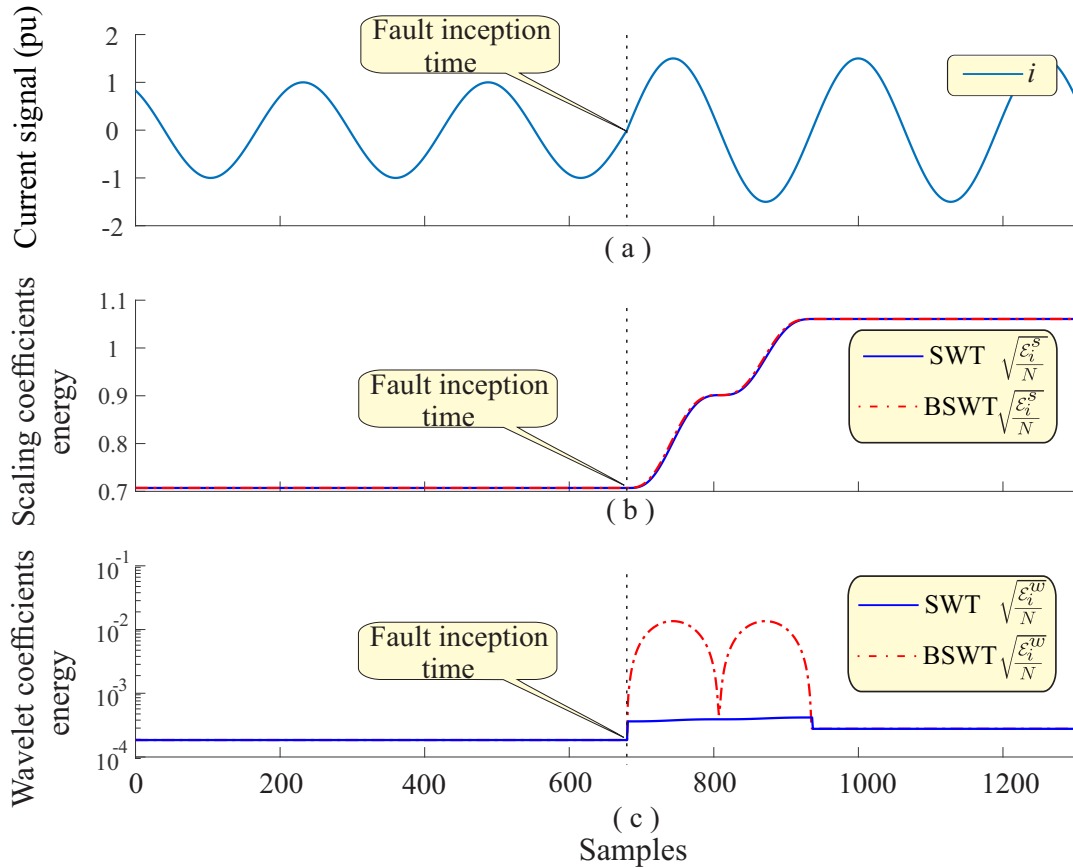


Figure 4.4: Comparisons between SWT and BSWT: (a) Original signal, (b) Scaling coefficients energy, (c) Wavelet coefficients energy.

Figure 4.4(b) depicts a comparison between the scaling coefficients energy of the SWT and the BSWT, whereas the Figure 4.4(c) depicts the same comparison with the wavelet coefficients energy. This comparisons were made using  $\text{db}(4)$  as mother wavelet, in a sampling frequency of  $f_s = 15.360$  Hz with a sliding window  $\Delta k = 256$  samples.

### 4.3 Summary

In this chapter, an overview of the Fourier transform and the different versions of the wavelet transform was presented. The energy calculations of the scaling and wavelet coefficients were also presented, along with a new energy calculation formulation that takes into account the boundary effects. These energies of the wavelet and scaling coefficients will be employed at the analysis presented in this work.

---

# Chapter 5

## Fundamentals of Protection Systems

---

This chapter presents theoretical concepts about the overcurrent, undervoltage, directional and differential protections applied in an electrical power system. Initially, the conventional protection is addressed, thereafter, the wavelet-based protection approach is presented. Focusing on a contextualization of these protection types applied in a scenario with DFIG.

Researches about protection systems aim to guarantee the people and animals maximum safety as well as electrical equipment and materials connected at power system. Notwithstanding, insertion of DFIGs into the electrical distribution system can lead to failures in the relays operation.

### 5.1 Overcurrent Protection

Overcurrents can happen by system overload and by electrical short-circuits (faults). Therefore, when the measured currents exceed a predefined threshold (pick-up current), the overcurrent relay is sensitized. Moreover, this relay is classified into two categories: instantaneous or time delay, whereas the last one can be with defined time or inverse time.

Distribution systems with DFIGs are challenging scenarios for the overcurrent protection due to the power flow redistribution, reduced fault overcurrent levels in the substation, and new coordination studies are required to the system. In addition, this barrier is higher when the short-circuit currents are associated with high resistance faults.

#### 5.1.1 Conventional Overcurrent Protection

Absolute current values are usually extracted from the Fourier transform in conventional overcurrent relay (Costa et al. 2017). Therefore, in an overcurrent occurrence the Fourier coefficients will increase. However, this is not an instantaneous growth, requiring a time interval to reach the new steady-state value due to transient components and the phasor estimation as well.

This protection is divided in two functions, which are the instantaneous and time-delay. Table 5.1 summarizes the instantaneous units, the pickup current and the sensitization condition to occur the relay trip. The instantaneous functions are enabled when the absolute value of the measured overcurrent, or the absolute value of the symmetrical components, exceeds a threshold, in which  $I_r$  is the load current in normal operation.

$N_{50}$ ,  $N_{50P}$ ,  $N_{50Q}$ ,  $N_{50N}$  are the variables used in the conventional protection to indicate how many times must multiply  $I_r$  to consider a fault occurrence. The zero sequence unit is similar to the  $50N$  unit.

Table 5.1: Instantaneous overcurrent units

Instantaneous Unit	Pickup current	Sensitization condition
Phase unit (50) $I(k) = I_A(k), I_C(k), I_B(k)$	$I_{50} = N_{50} \cdot I_r$	$I(k) > I_{50}$
Positive unit (50P) $I_1(k)$	$I_{50P} = N_{50P} \cdot I_r$	$I_1(k) > I_{50P}$
Negative unit (50Q) $I_2(k)$	$I_{50Q} = N_{50Q} \cdot I_r$	$I_2(k) > I_{50Q}$
Neutral unit (50N) $I_N(k) \approx 3 \cdot I_0(k)$	$I_{50N} = N_{50N} \cdot I_r$	$I_N(k) > I_{50N}$

### Characteristic Curves

The time characteristics of the time-delay overcurrent relays are given by time versus current ( $t(s)$  versus  $i(A)$ ) curves. Therefore, one of the curve types is the inverse time curves, in which the actuation time is inversely proportional to the overcurrent absolute value and the most commonly used curves are IEC 60255-3 and IEEE C37.112 standards. These curves are classified as inverse, very inverse, and extremely inverse such as illustrated in Figure 5.1 (Costa et al. 2017).

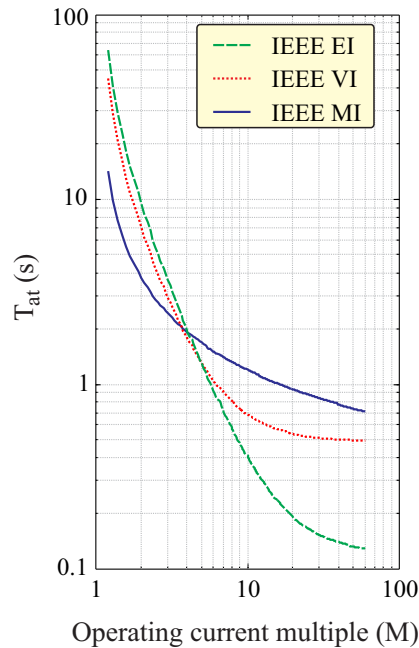


Figure 5.1: Characteristic inverse-time curve (adapted from Costa et al. (2017)).

The curve choice depends on the inherent characteristics of the electrical system; and according to the *IEEE Standard Inverse-Time Characteristic Equations for Overcurrent Relays* (1996), the curves are defined as follows:

$$T_{at} = \left( \frac{A}{M^P - 1} + B \right) \cdot TDS, \quad (5.1)$$

in which  $M = I(k)/I_s$ , wherein  $I(k)$  is the absolute value of the measured current and  $I_s$  is the start current, and the constants A, B, and P depend on the curve type, according to Table 5.2;  $T_{at}$  corresponds to the relay trip time;  $TDS$  is the time deal setting that allows the curves to be moved along the axis of the times and  $M$  corresponds to the multiple of the operating current.

Table 5.2: Curve types and their constants according to IEEE Standard Inverse-Time Characteristic Equations for Overcurrent Relays, 1996.

Curves type	A	B	P
Inverse	0.0515	0.1140	0.02
Very inverse	19.6100	0.4910	2.00
Extremely inverse	28.2000	0.1217	2.00

Table 5.3 shows the time-delay units, the pickup current and the sensitization condition to occur the relay trip. The time-delay functions are enabled when the absolute value, or the absolute value of the symmetrical components of the measured overcurrent is higher than a threshold.

Table 5.3: Time-delay overcurrent units

Time-delay Unit	Pickup current	Sensitization condition
Phase unit (51) $I(k) = I_A(k), I_C(k), I_B(k)$	$I_{51} = N_{51} \cdot I_r$	$I(k) > I_{51}$
Positive unit (51P) $I_1(k)$	$I_{51P} = N_{51P} \cdot I_r$	$I_1(k) > I_{51P}$
Negative unit (51Q) $I_2(k)$	$I_{51Q} = N_{51Q} \cdot I_r$	$I_2(k) > I_{51Q}$
Neutral unit (51N) $I_N(k) \approx 3 \cdot I_0(k)$	$I_{51N} = N_{51N} \cdot I_r$	$I_N(k) > I_{51N}$

$N_{51}$ ,  $N_{51P}$ ,  $N_{51Q}$ ,  $N_{51N}$  are the variables used in the conventional protection to indicate how many times must multiply  $I_r$  to have a fault. The relay will trip at time  $k_{Trip}/fs = k_{unit}/fs + T_{at}$ , where  $T_{at}$  can be obtained by the inverse-time characteristic curves and it is the actuation time,  $k_{unit}$  is the sample wherein the unit activation occurred and  $k_{Trip}$  is the sample wherein the relay operates.

### 5.1.2 Wavelet-Based Overcurrent Protection

By using the SWT with boundary effect, the true rms currents ( $i_{rms}$ ) can be associated with the spectral energy ( $E$ ) during the steady-state system operation, which can be approximated to the scaling coefficients energy as follows (Costa and Driesen 2013):

$$i_{rms}(k) = \sqrt{\frac{1}{\Delta k} E_i(k)} \approx \sqrt{\frac{1}{\Delta k} \epsilon_i^s(k)}. \quad (5.2)$$

where  $\Delta k$  is the window length;  $k \geq \Delta k$ .

The relationship between rms current and scaling coefficient energy enables the development of the wavelet-based overcurrent unit protection. (5.2) is used in order to compare the wavelet- and Fourier-based overcurrent protection methods. However, the wavelet-based overcurrent protection operates with the scaling coefficient energy, where it does not require square root and the division processing by  $\Delta k$  in a real-time computation (Costa et al. 2017).

Table 5.4 depicts the wavelet-based instantaneous units, the pickup energy and the sensitization condition to occur the relay trip. The instantaneous functions are enabled when the absolute value, or the absolute value of the symmetrical components of the measured energy exceeds a threshold.  $\mathcal{E}_i^s$  is the boundary scaling coefficient energy related to steady-state operation, taken as the reference energy.  $\epsilon_i^s$  is the measured phase energy, and  $\epsilon_{iP}^s$ ,  $\epsilon_{iQ}^s$  and  $\epsilon_{iN}^s$  are the positive, negative and zero current energy, respectively.

Table 5.4: Wavelet-based instantaneous overcurrent units

Instantaneous Unit	Pickup energy	Sensitization condition
Phase unit (50W) $\epsilon_i^s = \{\epsilon_{iA}^s, \epsilon_{iB}^s, \epsilon_{iC}^s\}$	$E_{50}^s = N_{50}^2 \mathcal{E}_i^s$	$\epsilon_i^s(k) > E_{50}^s$
Positive unit (50PW) $\epsilon_{iP}^s(k)$	$E_{50P}^s = N_{50P}^2 \mathcal{E}_i^s$	$\epsilon_{iP}^s(k) > E_{50P}^s$
Negative unit (50QW) $\epsilon_{iQ}^s(k)$	$E_{50Q}^s = N_{50Q}^2 \mathcal{E}_i^s$	$\epsilon_{iQ}^s(k) > E_{50Q}^s$
Neutral unit (50NW) $\epsilon_{iN}^s(k)$	$E_{50N}^s = N_{50N}^2 \mathcal{E}_i^s$	$\epsilon_{iN}^s(k) > E_{50N}^s$

Rewriting (5.2) as follow:

$$\epsilon^s(k) \approx i_{rms}^2(k) \Delta k. \quad (5.3)$$

There is a relationship between the absolute current estimation and the scaling coefficient energy, given by:

$$\epsilon^s(k) \approx \frac{I^2(k) \Delta k}{2}, \quad (5.4)$$

by (5.4) is possible to determine the wavelet-based overcurrent protection threshold with  $N_{50}^2$ ,  $N_{50P}^2$ ,  $N_{50Q}^2$  and  $N_{50N}^2$ .



Table 5.5 depicts the wavelet-based time-delay units, the pickup energy and the sensitization condition to occur the relay trip. The time-delay functions are enabled when the absolute value, or the absolute value of the symmetrical components of the measured energy exceeds a threshold.

Table 5.5: Wavelet-based time-delay overcurrent units

Time-delay Unit	Pickup energy	Sensitization condition
Phase unit (51W) $\epsilon_i^s = \{\epsilon_{iA}^s, \epsilon_{iB}^s, \epsilon_{iC}^s\}$	$E_{51}^s = N_{51}^2 \mathcal{E}_i^s$	$\epsilon_i^s(k) > E_{51}^s$
Positive unit (51PW) $\epsilon_{iP}^s(k)$	$E_{51P}^s = N_{51P}^2 \mathcal{E}_i^s$	$\epsilon_{iP}^s(k) > E_{51P}^s$
Negative unit (51QW) $\epsilon_{iQ}^s(k)$	$E_{51Q}^s = N_{51Q}^2 \mathcal{E}_i^s$	$\epsilon_{iQ}^s(k) > E_{51Q}^s$
Neutral unit (51NW) $\epsilon_{iN}^s(k)$	$E_{51N}^s = N_{51N}^2 \mathcal{E}_i^s$	$\epsilon_{iN}^s(k) > E_{51N}^s$

The relay will trip at time  $k_{TripW}/f_s = k_{51W}/f_s + T_{atw}$ , where  $T_{atw}$  is the relay operating time, which can be obtained by the inverse-time characteristic curves Figure 5.2.  $T_{atw}$  is mathematically defined as follows (de Cavalcante Paiva 2015):

$$T_{atw} = \left( \frac{A}{(M^s)^{\frac{p}{2}} - 1} + B \right) T_D, \quad (5.5)$$

in which  $M^s = \mathcal{E}_i^s(k)/E_{51W}^s$ .

The characteristic curves use to represent the inverse time in the wavelet-based protection are similar to the conventional one. However, the inverse time characteristics are given by time versus energy curves ( $t$  versus  $\epsilon$ ) as illustrated in Figure 5.2 (Costa et al. 2017). These curves are classified as inverse, very inverse and extremely inverse too.

The symmetrical components can be written in sample terms (Kasztenny et al. 2000). For instance, by using an ‘abc’ phase sequence system, the positive sequence current with phase A reference ( $i_{1A}$ ), phase B reference ( $i_{1B}$ ) and phase C reference ( $i_{1C}$ ) and negative sequence current with phase A reference ( $i_{2A}$ ), phase B reference ( $i_{2B}$ ) and phase C reference ( $i_{2C}$ ), are computed as follows:

$$\begin{aligned} i_{1A}(k) &= \frac{(i_A(k) + i_B(k - \Delta k_\alpha) + i_C(k - \Delta k_\alpha^2))}{3}, \\ i_{1B}(k) &= \frac{(i_C(k) + i_A(k - \Delta k_\alpha) + i_B(k - \Delta k_\alpha^2))}{3}, \\ i_{1C}(k) &= \frac{(i_B(k) + i_C(k - \Delta k_\alpha) + i_A(k - \Delta k_\alpha^2))}{3}, \end{aligned} \quad (5.6)$$

$$\begin{aligned} i_{2A}(k) &= \frac{(i_A(k) + i_B(k - \Delta k_\alpha^2) + i_C(k - \Delta k_\alpha))}{3}, \\ i_{2B}(k) &= \frac{(i_C(k) + i_A(k - \Delta k_\alpha^2) + i_B(k - \Delta k_\alpha))}{3}, \\ i_{2C}(k) &= \frac{(i_B(k) + i_C(k - \Delta k_\alpha^2) + i_A(k - \Delta k_\alpha))}{3}, \end{aligned} \quad (5.7)$$

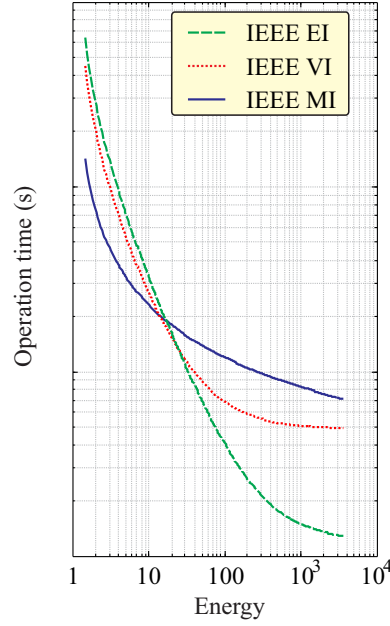


Figure 5.2: Characteristic inverse-time curve in the wavelet domain (adapted from Costa et al. (2017)).

where  $\Delta k_{\alpha} = \Delta k - \lceil \frac{2\Delta k}{3} \rceil$  and  $\Delta k_{\alpha 2} = \Delta k - \lfloor \frac{\Delta k}{3} \rfloor$  represent  $120^{\circ}$  and  $240^{\circ}$  equivalent delays, respectively. The operator  $\lceil \cdot \rceil$  is the ceiling function and  $\lfloor \cdot \rfloor$  is the floor function.

By using the negative sequence in terms of samples, the scaling and wavelet coefficients can be computed by (4.15) and (4.16), and the boundary scaling and wavelet coefficient energy can be computed by (4.27) and (4.28).

## 5.2 Undervoltage Protection

The undervoltage protection purpose is monitor the PCC to protect the DFIG, or generators in general, against voltage sags which can damage the machine elements. Furthermore, the main cause of this disturbance in transmission and distribution systems are electrical faults (Costa and Driesen 2013), as also the connection of large loads in the grid and excessive loading of feeder circuits according with de Cavalcante Paiva (2015).

According to IEEE (2003), it is considered a voltage sag a measured voltage under than 88% of the reference system voltage (V). Therefore, the conventional undervoltage protection function (27) is sensitized and act after a defined time as described in (IEEE 2003) and illustrated in Table 5.6.

As the overcurrent protection, the conventional undervoltage protection (function 27) is based on measured electrical variables which uses the Fourier algorithm of one-cycle to estimate the absolute value. However, this protection does not actuate instantly and it does not use the time-inverse curve. Therefore, the function (27) operates with a time-defined curve. Figure 5.3 depicts this curve characteristics, in which  $T_{at}$  is the actuation

Table 5.6: Interconnection system response to abnormal voltages (Adapted from IEEE (2003))

Pickup voltage	Sensitization condition	Clearing time (s)
$V_{27} = V \times 0.5$	$V < V_{27}$	0.16
$V_{27} = V \times 0.88$	$V < V_{27}$	2.00

time, wherein for any value above  $V_{MIN}$ , the system will trip.

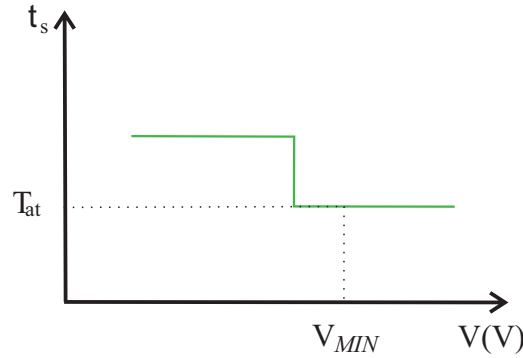


Figure 5.3: Characteristic time defined curve.

The wavelet-based undervoltage protection, proposed by de Cavalcante Paiva (2015) is similar to the wavelet-based overcurrent protection because this protection also use the scaling coefficient energy to estimate the variable amplitude value. Table 5.7 illustrates the sensitization conditions.

Table 5.7: Interconnection system response to abnormal voltages (Adapted from IEEE (2003) and de Cavalcante Paiva (2015))

Pickup voltage	Sensitization condition	Clearing time (s)
$E_{27W}^s = V_{27}^2 = 25\% \times V^2 \Delta k$	$V < E_{27W}^s$	0.16
$E_{27W}^s = V_{27}^2 = 77\% \times V^2 \Delta k$	$V < E_{27W}^s$	2.00

### 5.3 Directional Protection

The directional protection is used to obtain information about the fault direction. It is able to detect if the fault occurrence was to forward or backward in relation to the measuring point. There are four directional units which are: directional phase unit, directional positive sequence unit, directional negative sequence unit, and directional zero sequence unit, that operate relating the polarizing voltages ( $V_{pol}$ ) to the operating currents ( $I_{op}$ ). Table 5.8 depicts the conventional directional protection function (function 32) (Roberts and

Guzman 1994) with the respective torque equation of each units that compose this function. The subscripts 1, 2 and 0 refer to positive, negative and zero sequence, respectively. In addition,  $Z_{L1}$  and  $Z_{L0}$  are the positive and zero sequence impedances of the system. Table 5.8 illustrates the non-normalized torque equations. However, it is possible uses only the cosines values from the torque equations as a normalized directional torque.

Table 5.8: Conventional directionl protection units

Function unit	$V_{pol}$	$I_{op}$	Torque equation
Phase (32)	$V^*$	$I^*$	$T =  V^*  I^* \cos(\angle V_{pol} - \angle I_{op})$
Positive (32P)	$V_1(1\angle Z_1)$	$I_1$	$T_1 =  V_1  I_1 \cos(\angle 3V_1 - \angle 3I_1 - \angle Z_{L1})$
Negative (32Q)	$-V_2(1\angle Z_1)$	$I_2$	$T_2 =  V_2  I_2 \cos(\angle -3V_2 - \angle 3I_2 - \angle Z_{L1})$
Zero (32N)	$-V_0(1\angle Z_0)$	$I_0$	$T_0 =  V_0  I_0 \cos(\angle -3V_0 - \angle 3I_0 - \angle Z_{L0})$

$$V^* = \{V_{BC}, V_{CA}, V_{AB}\}, I^* = \{I_A, I_B, I_C\}.$$

As occurs in the overcurrent and undervoltage protections, the conventional directional protection operates with phasor estimation based on the Fourier transform. However, Leal et al. (2019) proposed a directional protection based on the wavelet transform (function 32W), which demonstrate a better accuracy and robustness than the Fourier-based one, for instance, the better time response with all units composition.

The scaling torque equation of the function 32W is given by (Leal et al. 2019):

$$T^s(k) = \frac{\sum_{n=k-\Delta k+1}^k s_{v_{pol}}(n)s_{i_{op}}(n)}{\sqrt{\epsilon_{v_{pol}}^s(n)\epsilon_{i_{op}}^s(n)}}, \quad (5.8)$$

in which the  $s_{v_{pol}}$  is the polarizing voltage scaling coefficients,  $s_{i_{op}}$  is the operating current scaling coefficients,  $\epsilon_{v_{pol}}^s(n)$  is the polarizing voltage scaling coefficient energy and  $\epsilon_{i_{op}}^s(n)$  is the operating current scaling coefficient energy. Table 5.9 depicts the operating current and polarizing voltages just units evolving phase A. However, as presented in (Leal et al. 2019), all traditional units could be recreated by using SWT.

Table 5.9: The wavelet-based operation and polarization quantities (Adapted from Leal et al. (2019)).

Function unit	$I_{op}$	$V_{pol}$
Phase A (32WA)	$i_A(k)$	$v_{BC}(k)$
Positive A (32PWA)	$i_{1A}(k)$	$v_A(k - \Delta k_{Z_1}) + v_B(k - \Delta k_{\alpha} - \Delta k_{Z_1}) + v_C(k - \Delta k_{\alpha^2} - \Delta k_{Z_1})$
Negative A (32QWA)	$i_{2A}(k)$	$v_A(k + \Delta k/2 - \Delta k_{Z_1}) + v_B(k - \Delta k_{\alpha^2} + \Delta k/2 - \Delta k_{Z_1}) + v_C(k - \Delta k_{\alpha} + \Delta k/2 - \Delta k_{Z_1})$
Zero (32NW)	$i_0(k)$	$v_A(k + \Delta k/2 - \Delta k_{Z_0}) + v_B(k + \Delta k/2 - \Delta k_{Z_0}) + v_C(k + \Delta k/2 - \Delta k_{Z_0})$

The  $\Delta k_{\alpha}$  and  $\Delta k_{\alpha^2}$  refer to  $120^\circ$  and  $240^\circ$ ;  $\Delta k_{Z_1}$  and  $\Delta k_{Z_0}$  are positive and zero sequence line impedances, respectively.

## 5.4 Differential Protection

The differential protection, function (87), is widely applied in power transformers, electrical machines and transmission lines. When related to the DFIG, few publications address about this theme, (Mansouri et al. 2016) and (Zarei et al. 2018). Figure 5.4 illustrates the DFIG in a differential configuration.

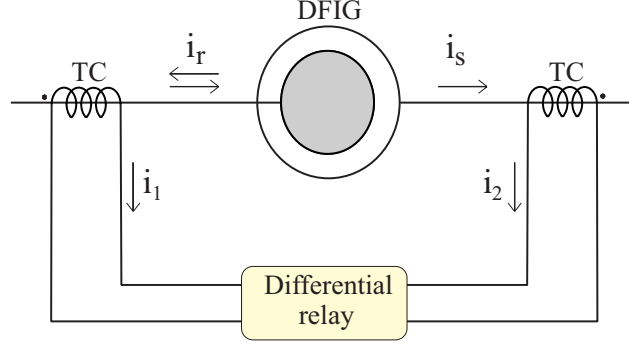


Figure 5.4: DFIG differential protection scheme.

The conventional current differential protection is based on phasor estimation, where the principle of this protection is a phasor comparison of the currents which pass through the windings in both sides, both stator windings and rotor windings. Therefore, there is a differential operating current, given by:

$$I_{op}^d = |\hat{i}_1 - \hat{i}_2|, \quad (5.9)$$

in which  $i_1$  is the rotor measured current and  $i_2$  is the stator measured current. In normal conditions, the operating current is null. However, in case of internal faults, this current reaches significant values. Furthermore, there is another equation related to the restraint current, which is given by:

$$I_{res}^d = \frac{|\hat{i}_1 + \hat{i}_2|}{2}. \quad (5.10)$$

The  $I_{res}^d$  is used as a condition to detect an internal fault, as follow:

$$I_{op}^d \geq K \cdot I_{res}^d, \quad (5.11)$$

$$I_{op}^d \geq I_{pickup}, \quad (5.12)$$

in which  $I_{pickup}$  is a minimum activation current and  $K$  is a relay sensitivity factor. If conditions (5.11) and (5.12) are met, it means that internal faults were detected.

The wavelet-based differential protection was proposed by de Medeiros (2014), which calculates the wavelet coefficient energy of the operation current (5.9) producing  $\epsilon_D$  and

calculates the wavelet coefficients energy of the restraint current (5.10) producing  $\epsilon_R$ . The internal fault is detected if:

$$\epsilon_D > E_D, \quad (5.13)$$

$$\epsilon_R > K_w \epsilon_R, \quad (5.14)$$

where  $K_w$  is the slope of characteristic curves and  $E_D$  is a threshold given by (de Medeiros 2014):

$$E_D = \frac{2}{k_2 - k_1 + 1} \sum_{n=k_1}^{k_2} \epsilon_D^{wb}, \quad (5.15)$$

where  $\epsilon_D^{wb}$  is the wavelet coefficient energy of the operating current with no border effect. Furthermore,  $k_1$  and  $k_2$  are an time interval.

## 5.5 Summary

In this chapter, a theoretical basis about the Fourier- and wavelet-based protections, which are used in this work, were introduced. The instantaneous overcurrent protection units were described, and the time-delay overcurrent protection was also presented with their characteristic curves. Furthermore, the undervoltage, directional and differential protection were introduced in order to briefly explain about their concepts.

---

# Chapter 6

## Methodology

---

This chapter introduces the procedures to implement the overcurrent, undervoltage, directional, and differential wavelet-based protections applied to the DFIG topology, as depicted in Figure 6.1, in which all relay units were validated through signals obtained by measurement instruments, which are potential transformers (PT) and current transformers (CT). Furthermore, a brief explanation about the protective relay localization in a DFIG assembly is also presented.

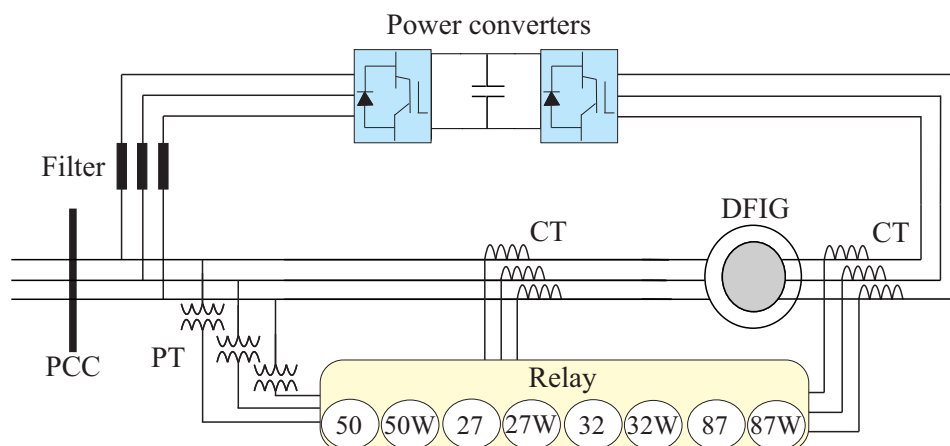


Figure 6.1: Simplified relay-based protections scheme.

### 6.1 Protection Applied in DFIG

The protection devices seek the maximum operational continuity of the electrical system. Furthermore, these devices need to guarantee reliable protection of the equipment which compose the generation system, such as the DFIG assembly. Figure 6.2 illustrates the possible localizations of the measuring instruments used by the protective relays on the DFIG topology according to Franco et al. (2017). The most used protections applied on it are the overcurrent (function 50/51) and undervoltage (function 27) protections. However, other ones are also used, such as the overvoltage (function 59) and current unbalance

(function 46).

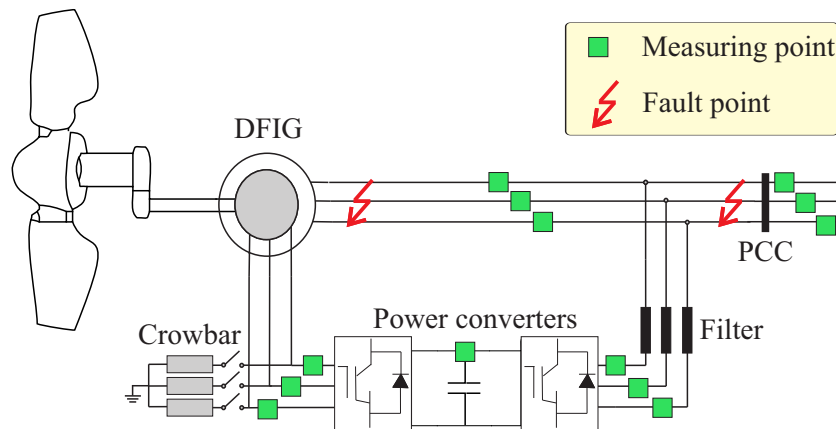


Figure 6.2: Measuring instruments location in a DFIG.

These favorable locations, for application of the measuring instruments in a DFIG, are used to detect faults on the power converters and in the rotor and stator windings or connections, as well as voltage sags or faults at the PCC in order to protect the DFIG-wind turbine and the electrical system. Generally, the detection strategies are used to trigger the LVRT categories, for instance, by means of protective circuit switches and the change of the control scheme between steady-state mode to transient-state mode. In case of internal faults, the protective relay send a trip to the machine breaker disconnecting the generator from the system in order to avoid large economic losses, electrical disturbances and protect the DFIG. Depending on the fault intensity at the PCC, the wind turbine should also be disconnected rather than triggering the LVRT categories. Therefore, this is done according to the relay setting parameters and selectivity and coordination studies.

Figure 6.2 illustrates two different fault locations. The first one is a fault between the stator winding connections and the sensors, so this point is considered as an internal fault, whereas the second point located between the sensors and the PCC is considered as an external fault point for the machine. In this work, these points were considered in all protection analysis using the real experimental data in order to assess the wavelet-based protections.

## 6.2 Implementation of the Overcurrent Protection

To analyze the overcurrent wavelet- and Fourier-based protections it is necessary to perform some procedures, as illustrated in Figure 6.3.

- Step 1 (one) is the data acquisition by current sensors, which is usually a CT. However, in case of low power generators, industrial sensors are enough. Moreover, some settings such as bandwidth and maximum overcurrent rate should be considered.



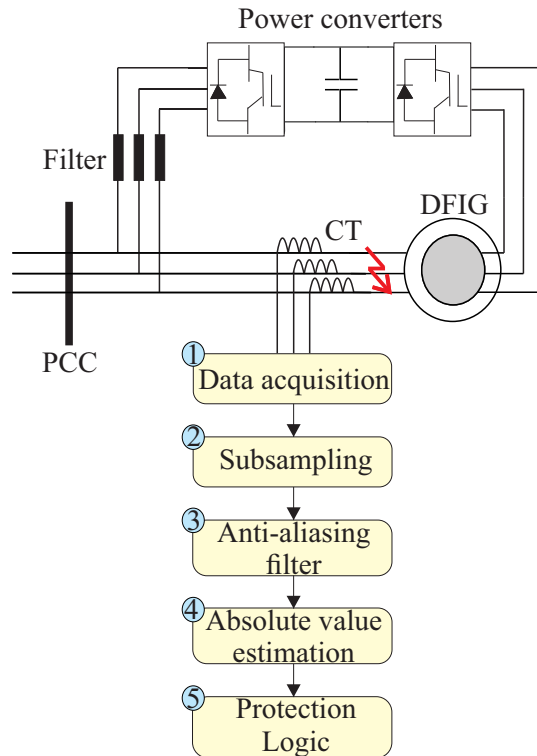


Figure 6.3: Overcurrent protection steps.

- Step 2 (two) is the sub-sampling process made for the offline analysis. The Fourier-based protection uses  $f_s = 1000$  Hz, whereas the wavelet-based protection uses  $f_s = 20000$  Hz, i.e., the sliding window are  $\Delta k \simeq 17$  and  $\Delta k \simeq 333$ , respectively. These algorithms are calculated recursively.
- Step 3 (three), the signal passes through an anti-aliasing filter with a cut-off frequency of  $f_c = 450$  Hz for the Fourier algorithm and  $f_c = 9000$  Hz for the wavelet algorithm, in which a second-order butterworth filter was used.
- Step 4 (four) represents the absolute value estimation, where the Fourier-based method uses equation (4.5) and the wavelet-based one uses equation (5.2) in order to compare both protection methods.
- Step 5 (five) is the logical protection according to section 5.1.

### 6.3 Implementation of the Directional Protection

Figure 6.4 illustrates the process to implement the directional protection (function 32).

- Step 1 (one) is a typical protection implementation stage which is made similarly to the aforementioned protection: the data acquisition, the filter process; with a cut frequency of  $f_c = 450$  Hz and  $f_c = 9000$  Hz to Fourier and wavelet algorithm, respectively; and sub-sampling stage, where the sampling frequency to the Fourier-

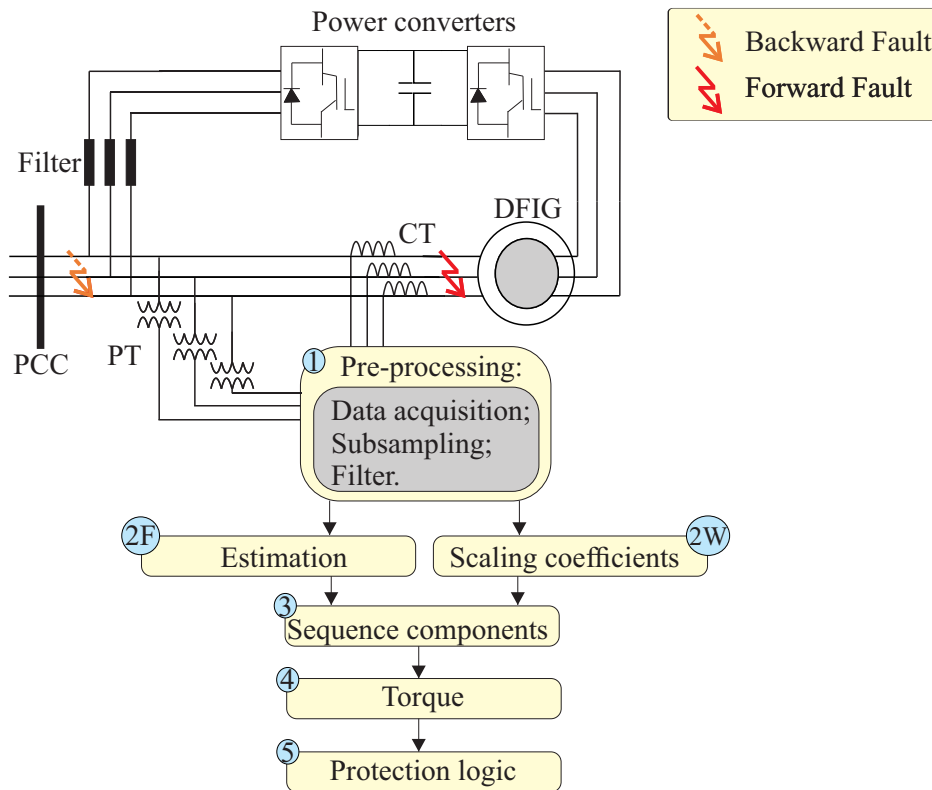


Figure 6.4: Directional protection steps.

based protection used  $f_s = 1000$  Hz and for the wavelet-based protection used  $f_s = 20000$  Hz, wherefore the sliding window are  $\Delta k \simeq 17$  and  $\Delta k \simeq 333$ , respectively.

- Step 2 (two) is divided in two different ways because the conventional directional protection using the Fourier transform to make the variables phasor estimation (2F), whereas the wavelet-based works in the time-domain and the variables scaling coefficients (2W) are calculated. These variables are the operating current ( $I_{op}$ ) and the polarizing voltage ( $V_{pol}$ ).
- Step 3 (three) is the sequence components calculation. However, this step is optional, because from step two it is possible to go directly to step four to calculate the phase torque unit. Notwithstanding, step 3 is necessary only when will be used the directional sequence units.
- Step 4 (four) is the torque calculation according to Table 5.8 for the Fourier- and Table (5.9) for the wavelet-based protections.
- Step 5 (five) is the protection logical, in which the protection trip will happen if the calculated torque is higher than an up fixed threshold for forward faults and lower than a down fixed threshold for backward faults. However, commonly, the directional protection only acts to forward faults.

## 6.4 Implementation of the Differential Protection

Figure 6.5 depicts the process to implement the differential protection (function 87).

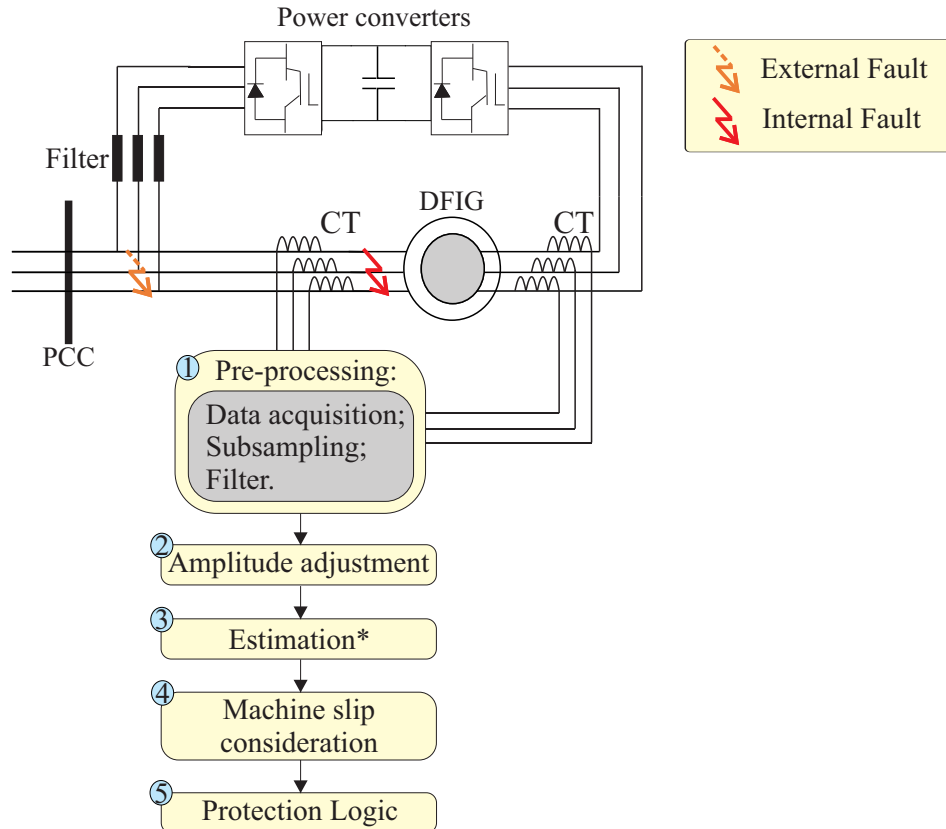


Figure 6.5: Differential protection steps.

- Step 1 (one) is a typical protection implementation stage, which is performed similarly to the aforementioned protections. In this protection type, two different currents are needed, where the first one are stator currents and the second one are rotor currents.
- Step 2 (two), the normalization of stator and rotor currents are done according to (Mansouri et al. 2016). The amplitudes of the currents are normalized considering the turns ratio of the rotor and stator. Generally, the machine windings are connected in star (Y/Y). Therefore, the angle compensation, which is done for power transform, is not applied for electrical machines. However, in case of another windings connection type, such as delta/star or star/delta, an angle compensation needs to be done.
- Step 3 (three) is done with a different process to each protection method. To the Fourier-based protection, a phasor estimation is performed according to (4.5) and (4.6), whereas to the wavelet-based protection, the energy of the wavelet coefficients is calculated according to (4.28).

- Step 4 (four) the machine slip is considered, because the differential protection makes a signal comparison and, in this work, it was considered that the rotor currents enter inside the machine whereas the stator currents leave the machine to the grid. However, this consideration is true only if the machine is operating in the sub-synchronous mode. Therefore, whether the machine is operating in the super-synchronous mode it is necessary to make a signal correction in the rotor current.
- Step 5 (five) the protection logic is done according to (5.9) until (5.12).

## 6.5 Implementation of the Undervoltage Protection

Figure 6.6 illustrates the procedures implemented to analyze the undervoltage protection.

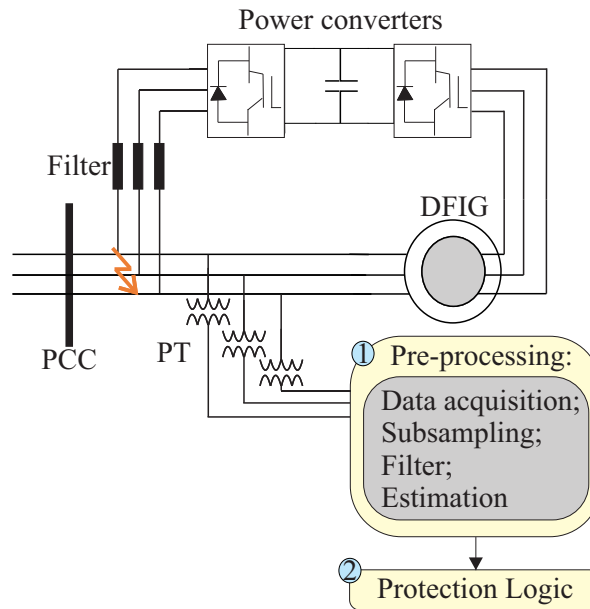


Figure 6.6: Undervoltage protection steps.

- Step 1 (one) is the pre-processing unit in which is performed the data acquisition by voltage sensors, which depending on the generator size is needed a PT (potential transformer). Notwithstanding, in case of low power generators, industrial sensors are enough. The sub-sampling process is done, where to the Fourier-based protection used  $f_s = 1000$  Hz and the wavelet-based protection used  $f_s = 20000$  Hz. Thereafter, the signal passes through an anti-aliasing filter with a cut-off frequency of  $f_c = 450$  Hz and  $f_c = 9000$  Hz to Fourier- and wavelet-based protections, respectively. Finally, the voltage absolute value estimation is obtained, where the Fourier-based method uses (4.5) and the wavelet-based method uses (5.2).
- Step 2 (two) is the logical protection according to 5.2.

## 6.6 Summary

This chapter presented the procedures to implement the Fourier- and the wavelet-based overcurrent, directional, differential, and undervoltage protections when applied in a DFIG assembly. Some protections schemes are implemented such as the conventional ones. However, others protections needs some modifications, for instance the differential protection which consider the machine slip to calculate the restraint and operating currents. In addition, the measurement instruments location were introduced.

---

# Chapter 7

## Protection and Signal Analysis

---

This chapter presents the analysis of experimental signals in a DFIG test-bench under fault situations. As a first step, the main focus is to observe the behavior of the DFIG variables, such as currents, voltages, magnetic flux, and machine slip, in the pre-fault, fault, and post-fault periods. The development and assessment of new protection methods are needed to find and validate methods which can present a better performance than the conventional ones. A good protection performance makes the system to respond better to faults at the PCC because it will make the LVRT categories act faster and protect the system as well. Therefore, experimental signals were used in order to analyze the wavelet-based overcurrent, directional, differential and Undervoltage protections and compare with the conventional ones, in order to verify which one has a better behavior in a system with DFIG.

### 7.1 Experimental Analysis

In order to analyze the experimental test bench in case of electrical faults, some analysis with the DFIG variables in case of electrical faults at the PCC were accomplished. The analyzed variables were: the grid voltage, the stator and rotor currents, the stator flux referring to the phase in fault, the machine slip, and the rotor speed. Beyond these signals, the behavior of active power, reactive power, and torque that compose this test bench is possible to be verified. The sampling frequency of the signals are  $f_s = 20000$  Hz and the fault resistance is  $r_f = 15 \Omega$  for all cases. Figure 7.1 illustrate the fault location for this experimental analysis and appendix A explain about the test-bench.

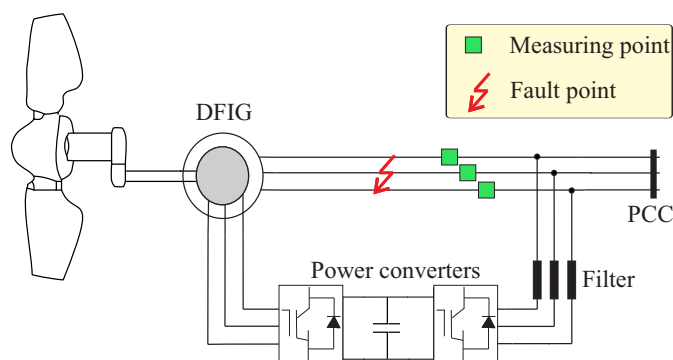


Figure 7.1: Fault location.

### 7.1.1 Single-Line-to-Neutral Fault

The first case is a single-line-to-neutral fault, as illustrated in Figure 7.2, with duration of 200 ms, where the fault started at 1.3 s and finished at 1.5 s, wherein this fault was manually removed without the support of protection schemes to trip the breaker. Figures 7.2(a) depicts the grid voltage. Notwithstanding, there is a great overcurrent, approximately four times higher than the steady-state current, in the stator windings as illustrated in Figure 7.2(b), in which the main frequency component is  $f = 60$  Hz. This overcurrent signal is useful for the overcurrent protection. The rotor speed is measured by an encoder and machine slip was calculated.

Since the machine has a small size and the applied fault have had small amplitudes, the magnetic coupling is not so expressive and the rotor currents, depicted in Figure 7.2(c), are not so affected by the electrical fault at the stator side. In addition, the rotor frequency is  $f_r \approx 9.09$  Hz in steady state. This low frequency could be a problem for differential protections in time-domain because it is needed a signal comparison, which should have the same amplitude, frequency and angular displacement.

Figures 7.2(e)-(f) depict the machine slip and the rotor speed, respectively. In steady-state the machine slip was  $s_i = 0.15$ , operating the machine in the sub-synchronous mode, with the rotor speed  $\Omega_m = 160$  rad/s. This machine was really affected by the fault, causing changes in their normal dynamic operation. Hence, events such as rotor vibration, mechanical stress, windings overheat, and machine saturation are able to occur. Therefore, some countermeasures need to be taken to avoid high machine damages, for instance, the protection actuation and control strategies. Notwithstanding, the control strategies are able only to small and medium grid disturbances according by Justo et al. (2015).

### 7.1.2 Line-to-Line-to-Neutral Fault

Figure 7.3 depicts a line-to-line-to-neutral fault at the PCC between the phase B and C. The fault clearing time was 250 ms, wherein the fault inception time was at 1.15 s and the fault clearance time was 1.4 s, approximately.

Figure 7.3(a) shows the grid voltage during the fault. However, there is no relevant voltage sag in the faulted voltages because of the imbalances present in the grid and the small voltage dip applicated. Therefore, in protection schemes which need a relation between the voltages of healthy phase and the faulted currents, such as the directional protection, this behavior could be a problem if the healthy phases will be affected by the faulted phase due to the machine magnetic coupling. Therefore, the directional torque will oscillate given a wrong protection flag. Moreover, for backward faults, the system would be not able to detect all faults occurrences, because the current level which passes through the sensor will be only according to the generator power without the grid current contribution.

Figures 7.3(c) depicts the rotor currents with a low frequency of  $f_r = 3.3$  Hz. Therefore, the machine is operating really near to the synchronous speed because the slip machine is approximately  $s_i = 0.06$  (Figure 7.3(e)). However, the machine slip and the rotor speed were scarcely affected. Figure 7.3(d) illustrates the stator flux referring to phase C, which achieve a fast and huge growth during the fault duration. Therefore, a fault detec-

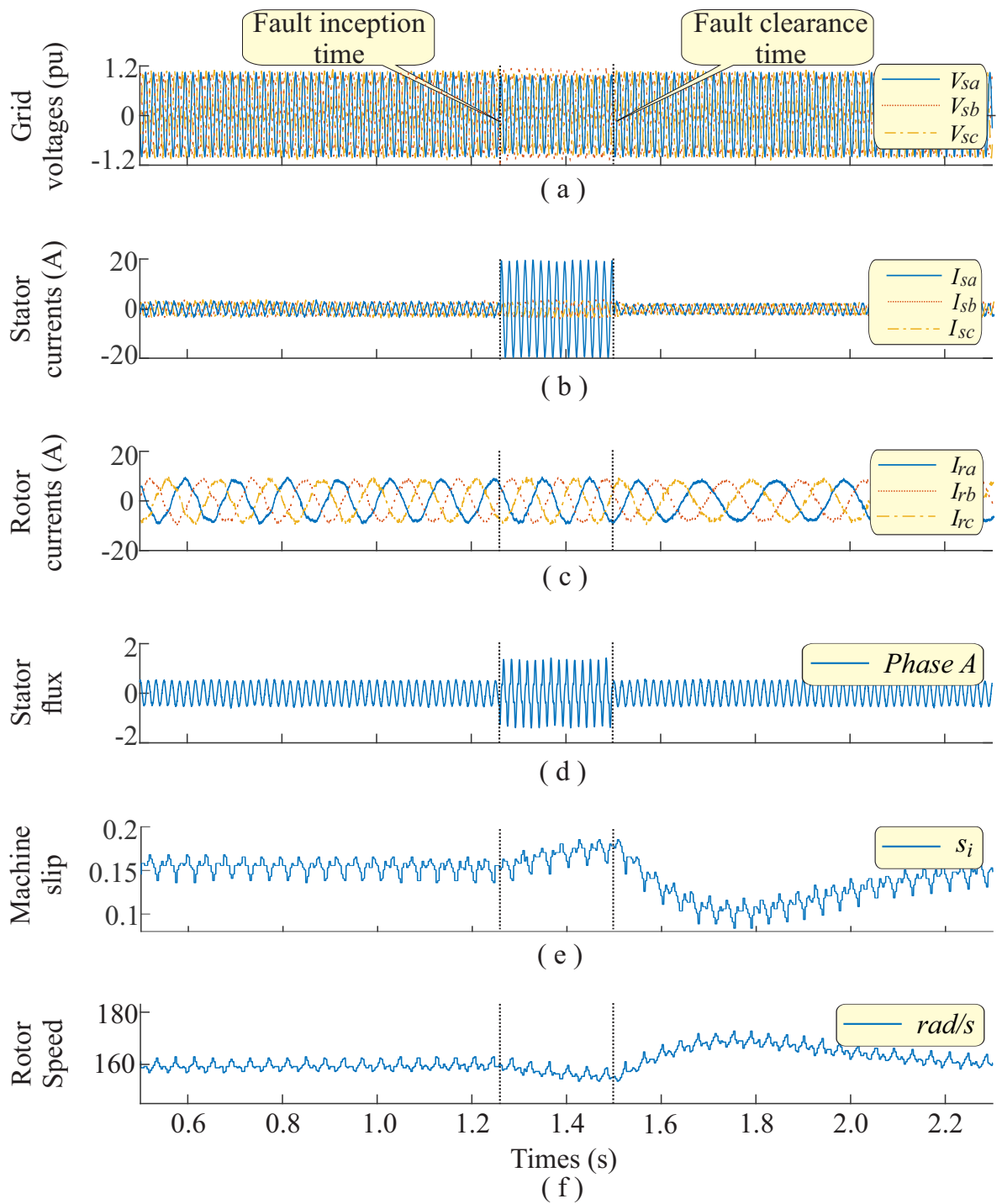


Figure 7.2: Experimental test-bench signals with a one-phase fault to neutral point: (a) Grid voltage in pu; (b) Stator currents; (c) Rotor currents; (d) Stator flux referring to phase A; (e) Machine slip; (f) Rotor speed.



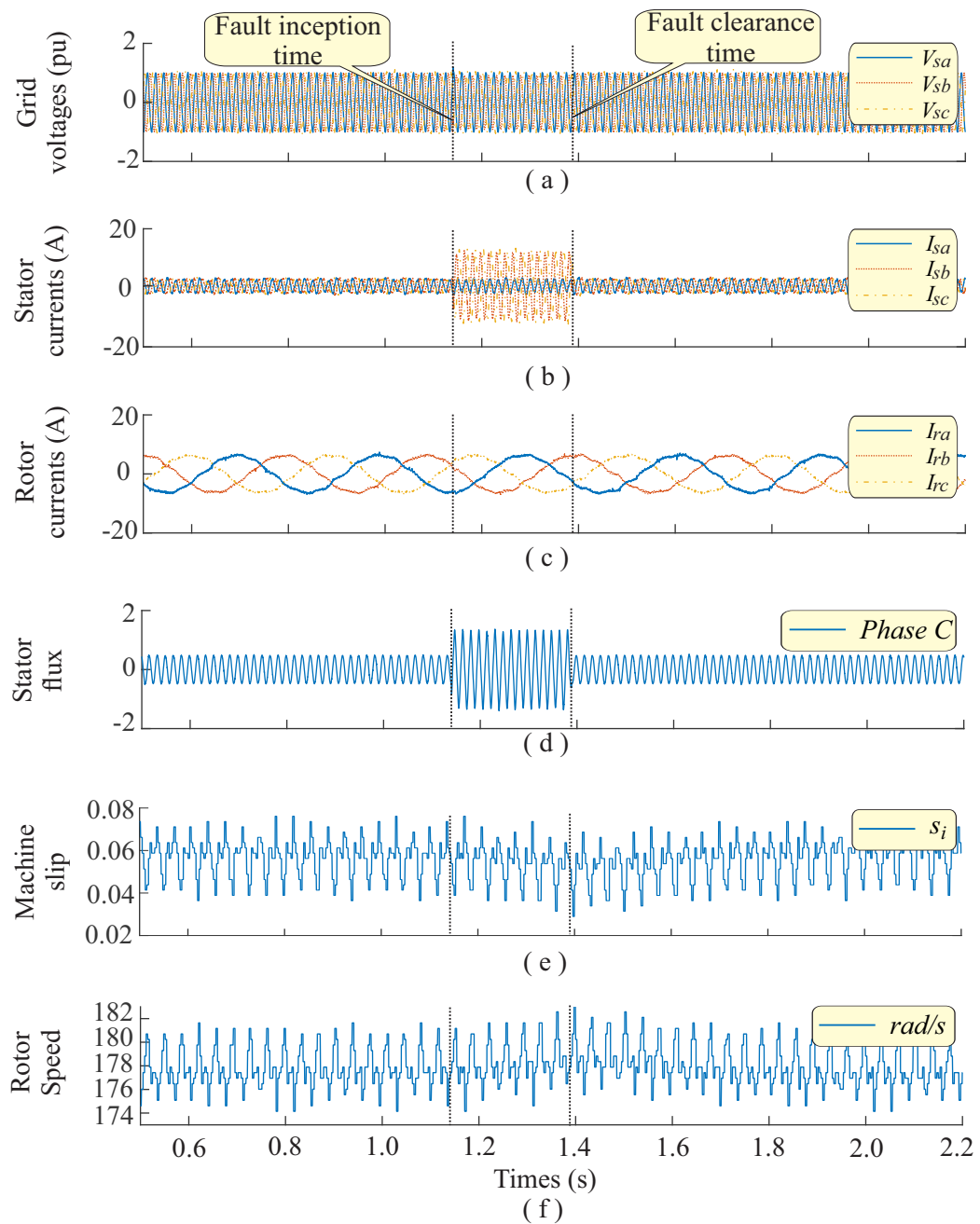


Figure 7.3: Experimental test-bench signals with a line-to-line fault to neutral point: (a) Grid voltage in pu; (b) Stator currents; (c) Rotor currents; (d) Stator flux referring to phase C; (e) Machine slip; (f) Rotor speed.

tion method is possible to be developed using this information because in case of faults this signal rapidly changes.

## 7.2 Analysis of the Overcurrent Protection

According to section 3.5, there are many challenges to be overcome when dealing with DFIG protection. Therefore, considering these challenges, in this study, two dynamic cases were examined for the experimental analyses. The first one involves a single line-to-ground (SLG) fault and the second one is a line-to-line fault. Those evaluated short-circuits occur between the sensors and the stator winding connections such as in Figure 6.3, and this location was chosen due to the presence of all characteristics inherent in DFIG, such as grid imbalance and voltage oscillations. Therefore, the results obtained at this assembly point can be replicated for all other points of DFIG topology, for instance, to the rotor side, to the power converters, and to the line filter.

The relay operating time and the percentage of correct answers were observed for all real cases for both overcurrent protection methods, as evaluation and comparison criteria. However, the time-delay overcurrent units are not applied because the time which the generator must remain connected to the grid depends on the grid codes imposed by each country for faults at the PCC or near it, for instance, in Germany the turbine needs to remain connected to the PCC for 150 ms when the voltage drops to zero. Therefore, even if the time-delay overcurrent protection sent a trip to the relay the turbine should remain connected according to the grid code (LVRT), whereas the instantaneous overcurrent protection sends a flag to the LVRT categories to the turbine remain connected at the PCC according to the grid codes, thereafter if the fault remains the turbine will be disconnected. However, this function, the time-delay overcurrent protection, would be able to be used against power converters or windings faults.

The thresholds adopted for the instantaneous overcurrent unit was  $N_{50} = 3$  and for the neutral overcurrent unit and the negative-sequence overcurrent unit were  $N_{50N} = 0.2$ ,  $N_{50Q} = 0.3$ , respectively. These thresholds were chosen in order to allow the correct protection actuation considering the steady-state current as well as the maximum overcurrent achieved by the DFIG system. The wavelet-based overcurrent protection presented was proposed by Costa et al. (2017) for a distribution system validated only by simulations. Therefore, in this work, this wavelet-based protection has been assessed by real experimental data applied in a DFIG environment.

### 7.2.1 Single Line-to-Neutral Fault Analyses

Figure 7.4 depicts a SLG fault in phase A with fault resistance of  $r_f = 15 \Omega$ .  $I_a$ ,  $I_b$ ,  $I_c$  are the currents in phases A, B, and C, respectively. In addition, the wavelet coefficient energy  $\epsilon_{ia}^{\omega}$ , Figure 7.4(b), is introduced as a trigger signal in order to be used as instantaneous fault detector. The energy of the wavelet coefficients exceeded the threshold almost instantly at the fault inception time, which is an additional information that can be used to sensitize the relay such as addressed by 5.1.

As illustrated in Figure 7.4(c), the protection based on both Fourier (function 50) and wavelet (function 50W) methods actuated correctly for this fault, where  $|I_a|$  is the absolute value of the current in phase A estimated by the Fourier method and  $\sqrt{\epsilon_i^s/\Delta k}$  is the estimation of the absolute current in phase A by the scaling wavelet coefficient energy,

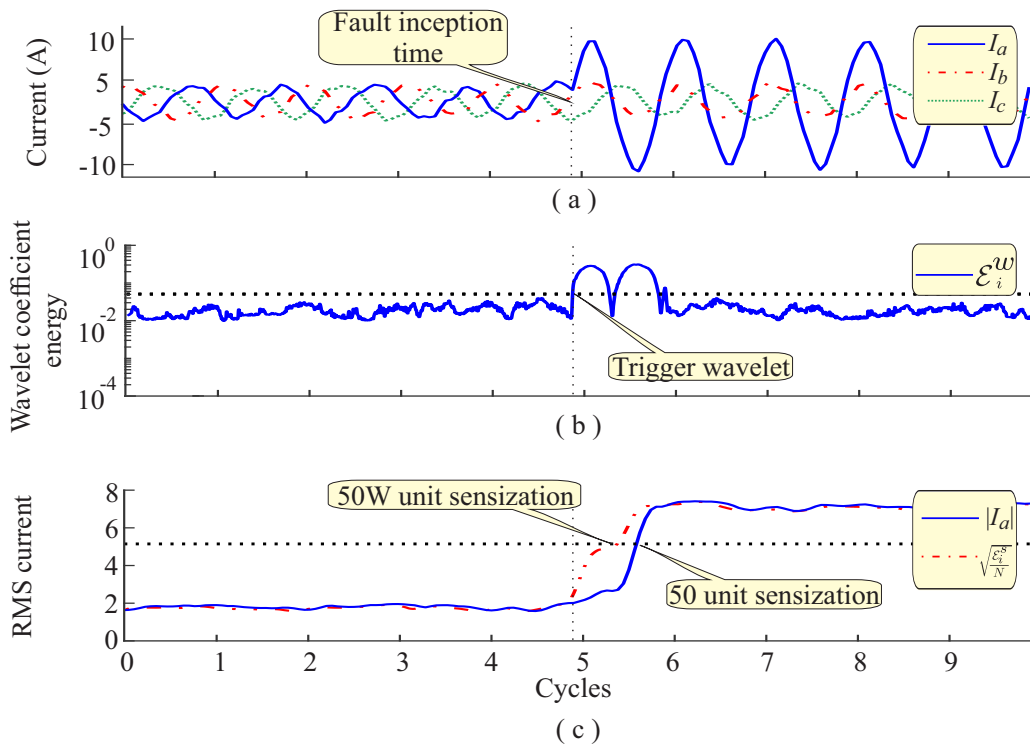


Figure 7.4: Overcurrent Protection Analyses: (a) Real signal; (b) Trigger wavelet; (c) phase units - conventional versus wavelet-based.

in which the scaling coefficient energy normalization is done in order to demonstrate the similarities of the methods. However, the wavelet-based overcurrent protection is based on the energies and not in the normalized energy, which reduces the processing time because do not require the square root operation and division by  $\Delta k$ . The relay operating time of the wavelet-based method was the fastest, in which the Fourier method act in 13 ms whereas the wavelet one act in 9.2 ms.

To analyze the robustness of the protection with different faults, a study was performed considering faults at different inception angles, because there are some critical inception angles which make the electric fault identification harder than others, which is owing to a smaller transient amount and DC component presence in accordance with the fault inception angle. Table 7.1 illustrates the obtained results. The ideal angles would be based on specifics angles of a sine wave, such as  $0^\circ$ ,  $90^\circ$ , and  $180^\circ$ . However, in this test-bench a non-ideal contactor was used providing a non-deterministic delay on the actuation time putting the fault inception in a different angle. The angles depicted in Table 7.1 was obtained by the Fourier algorithm phasor estimation.

According to Table 7.1, all protections would acted correctly for different fault inception angles. Nevertheless, this analysis confirms that the phase instantaneous unit of the wavelet-based protection would operate faster than the Fourier-based protection due to the fast response of the wavelet algorithm.

The overcurrent negative ( $|I_2|$  and  $\sqrt{\epsilon_{i2}^s/\Delta k}$ ) and zero ( $|I_0|$  and  $\sqrt{\epsilon_{i0}^s/\Delta k}$ ) sequence

Table 7.1: Relay Operating Time for Different Fault Inception Angles.

Angles	Operating time [ms]					
	50	50W	50Q	50QW	50N	50NW
27.98°	16.5	10.6	3.5	0.5	3.5	0.6
77.93°	12.5	9.3	2.5	0.4	3.5	0.5
83.59°	12.0	8.5	3.0	0.9	4.0	0.9
122.67°	14.5	11.7	4.5	2.5	5.5	2.4
224.27°	17.0	9.4	3.0	0.6	3.0	0.6
269.98°	13.5	10.4	3.5	0.9	3.5	0.9
277.38°	13.0	9.2	3.0	1.2	4.0	1.3
283.91°	13.5	10.1	3.5	1.0	3.5	0.9
<b>Average</b>	14.1	9.9	3.3	1.0	3.8	1.0

units were also tested. Figure 7.5 depicts the Fourier- and wavelet-based methods of the overcurrent negative (functions 50Q and 50QW) and zero (functionS 50N and 50NW) sequence units. According to this figure and Table 7.1, for the negative sequence (Figure 7.5(a)), the Fourier-based protection would act in 4 ms and to the wavelet-based protection would act in 1.3 ms, whereas the zero-sequence unit (Figure 7.5(b)) would act in 3 ms and 1.2 ms for Fourier- and wavelet-based protections, respectively. The Fourier- and wavelet-based overcurrent protection has performed well in all the units, with no problems to detect the fault instant. The current fault signal is depicted in Figure 7.4(a) which is the third case illustrated in Table 7.1.

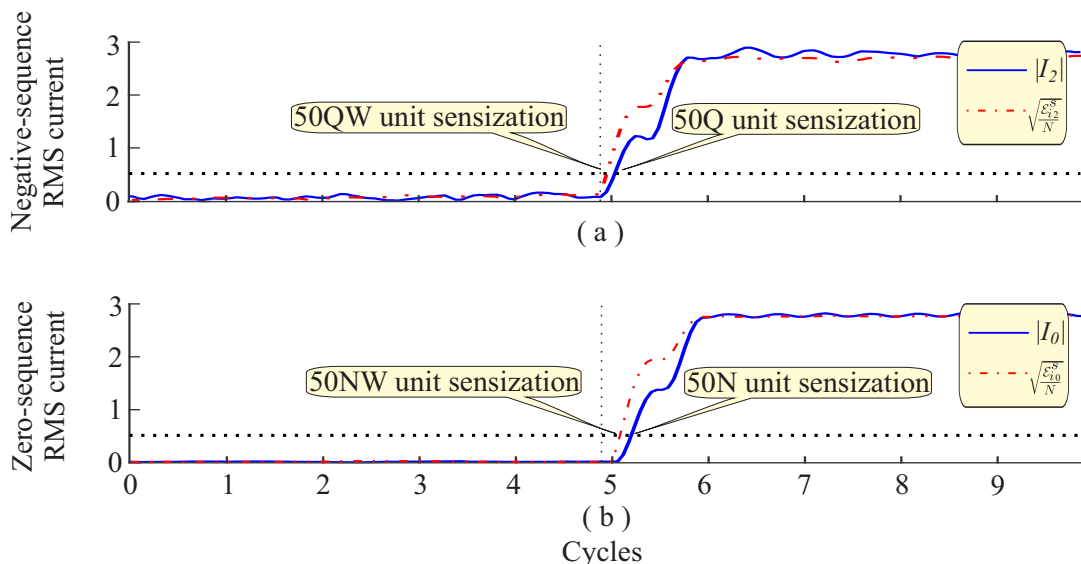


Figure 7.5: Overcurrent Protection Analyses: (a) Overcurrent protection negative sequence unit; (b) Overcurrent protection neutral sequence unit.

In general, the wavelet-based protection would provide the faster relay operating time than the Fourier-based protection for SLG faults.

## 7.2.2 Line-to-Line Fault Analysis

Figure 7.6 depicts a line-to-line fault in phases B and C, with fault resistance of  $r_f = 15 \Omega$ . Furthermore, the trigger wavelet signals in phase B ( $\epsilon_{ib}^0$ ) and in phase C ( $\epsilon_{ic}^0$ ) are presented in Figure 7.6(b) which is an additional information to sensitizes the relay in case of an electrical fault detection. In the fault inception, the wavelet coefficient energy exceeded the threshold almost instantly, acting correctly to detect the fault. Therefore, the trigger information is able to be used together with the overcurrent information to activate the LVRT categories as faster as possible.

Figure 7.6(c)-(d) illustrates the protection based on Fourier ( $|I_b|$ ,  $|I_c|$ ) and wavelet ( $\sqrt{\epsilon_{ib}^s/\Delta k}$ ,  $\sqrt{\epsilon_{ic}^s/\Delta k}$ ) transforms. Both methods actuated correctly for this fault. The acted time was of 13 ms to phase B and 12 ms to phase C for the Fourier-based, whereas to the wavelet-based was 6.1 ms and 8.1 ms for phases B and C, respectively. Therefore, the relay operating time of the wavelet-based method would be the fastest.

For the overcurrent instantaneous unit analyses, the overcurrent negative sequence unit was also analyzed. Figure 7.6(e) illustrates the negative sequence unit, wherein the Fourier-based ( $|I_2|$ ) was sensitized in 3 ms, whereas the wavelet-based ( $\sqrt{\epsilon_{i2b}^s/\Delta k}$ ,  $\sqrt{\epsilon_{i2c}^s/\Delta k}$ ) acted in 0.8 ms and 0.75 ms for phases B and C, respectively.

Similarly of the SLG fault, the wavelet-based protection presented a better relay operating time than the Fourier-based protection. Table 7.2 shows the time relation between the analyzed protections in different fault inception angles. Table 7.2 shows that the average of the wavelet-based protection was lower than the Fourier-based protection average to different fault inception angles in all overcurrent units analyzed.

Table 7.2: Relay Operating Time for Different Fault Inception Angles.

Angles*	Operating time [ms]					
	50B	50C	50BW	50CW	50Q	50QW
56.7°	13.0	12.0	6.1	8.1	3.0	0.8
69.0°	15.5	13.5	7.8	5.7	5.5	0.5
86.5°	16.0	13.0	7.9	5.6	4.0	0.4
274.6°	12.5	11.5	5.3	7.4	2.5	0.9
304.6°	15.0	13.0	7.6	5.0	4.0	0.7
328.5°	16.0	14.0	8.8	6.6	6.0	0.6
352.6°	15.5	13.5	8.3	5.8	4.5	0.7
<b>Average</b>	14.7	12.9	7.4	6.3	4.2	0.6

\*Angle referring to phase B.

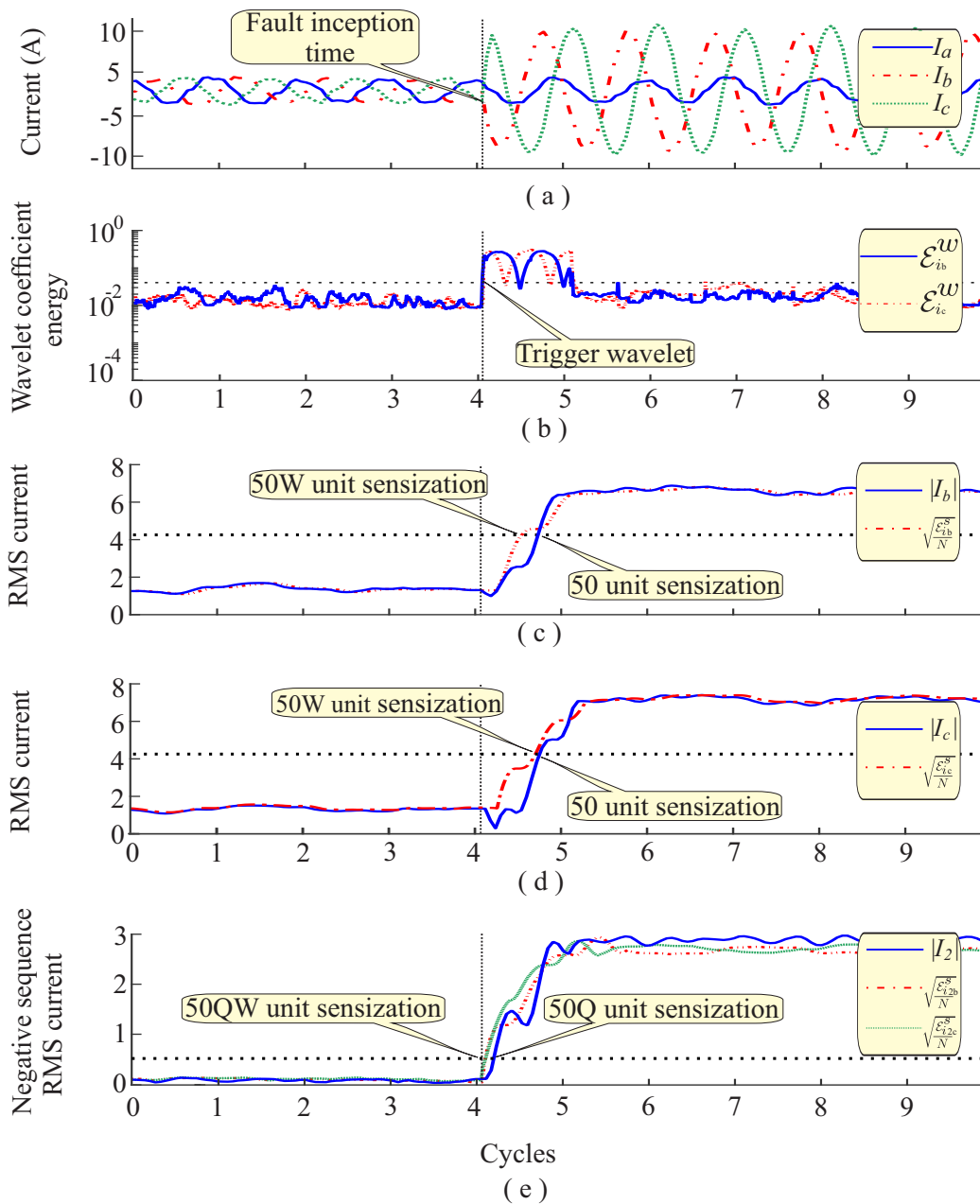


Figure 7.6: Overcurrent Protection Analyses: (a) Real signal; (b) Trigger wavelet; (c) Phase unit B; (e) Phase unit C; (f) Negative-sequence unit.

### 7.3 Analysis of the Directional Protection

In this section two dynamic cases were examined using experimental data. The first analyses involves eight SLG fault as forward fault, whereas, the second one are eight SLG fault as backward fault, both with eight different fault inception angles. The forward and backward faults are illustrated in Figure 6.4. The wavelet-based directional protection

applied in this work was proposed by Leal et al. (2019) for transmission line and this protection was validated only by simulations in the software Matlab/Simulink. Therefore, in this work, this wavelet-based protection has been assessed by real experimental data applied in a DFIG topology.

The relay operating time and the percentage of correct answers were observed for all real cases for both directional protection methods, as evaluation and comparison criteria.

### 7.3.1 Forward Fault Analyses

Figure 7.7 depicts the directional phase unit of the wavelet- and Fourier-based protections of a forward SLG fault in phase A, respectively, in which  $T_a^s$ ,  $T_b^s$ ,  $T_c^s$  are the scaling phase torque and  $T_a$ ,  $T_b$ ,  $T_c$  are the conventional phase torque, for phases ‘ABC’, respectively. The normalized directional protection was implemented to the Fourier-based method considering only the cosine from Table 5.8, whereas the wavelet-based is naturally normalized.

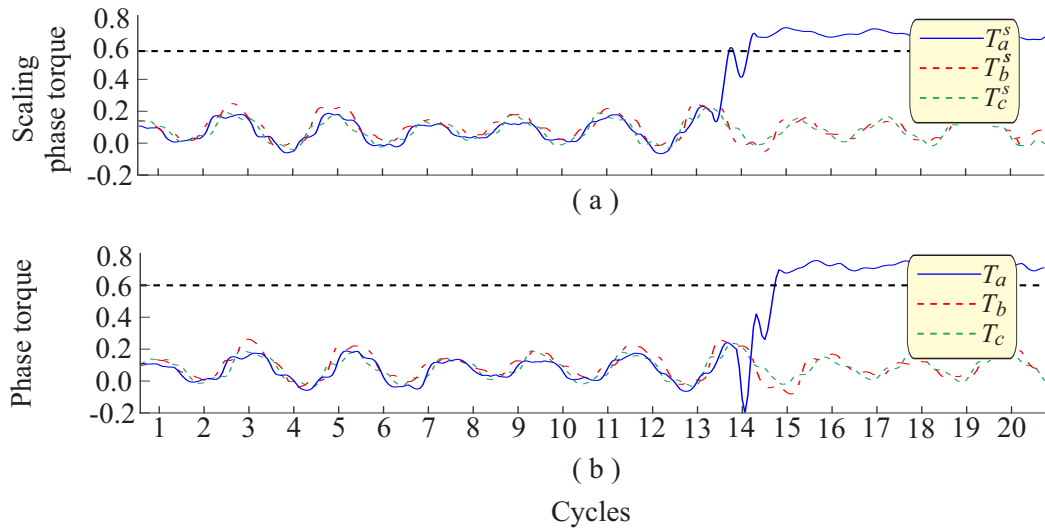


Figure 7.7: Directional protection phase unit - Forward fault: (a) Wavelet-based directional protection, (b) Fourier-based directional protection.

The threshold adopted for the directional phase unit was  $\gamma = 0.6$  to forward analysis in both protection methods. This value was chosen to avoid false directionality identification giving a wide margin of safety. For the DFIG system, the steady-state of the directional phase unit was centralized in 0.8. Therefore, an offset of 0.8 was put in order to centralize in 0.0 the steady-state. In the phase unit to forward faults, both protections achieved 100% of right answers. Notwithstanding, the wavelet-based presented the fastest response.

The directional sequence components units, negative and zero, are illustrated in Figure 7.8, respectively, in which,  $T_s^2$  and  $T^2$  are the scaling negative torque and the negative torque, respectively.  $T_s^0$  is the scaling zero torque and  $T^0$  is the zero torque. The applied thresholds were  $\gamma_Q = 0.6$  and  $\gamma_N = 0.6$  for the Fourier and wavelet algorithm. The

Fourier-based presented an oscillatory behavior in the steady-state. However, the directional protection works as a backup protection. Thus, in the steady-state, this protection is disabled only activated in case of fault detection. Therefore, the oscillatory behavior is not a problem when occurs in the steady-state. After the fault inception time, the Fourier method oscillates but in the correct direction. However, the wavelet-based method is more stable than the Fourier-based one, providing an easier study to determine the protection threshold. For this fault type, the phase, negative-sequence, and zero-sequence would act correctly to identify the fault directionality. In addition, both methods work properly.

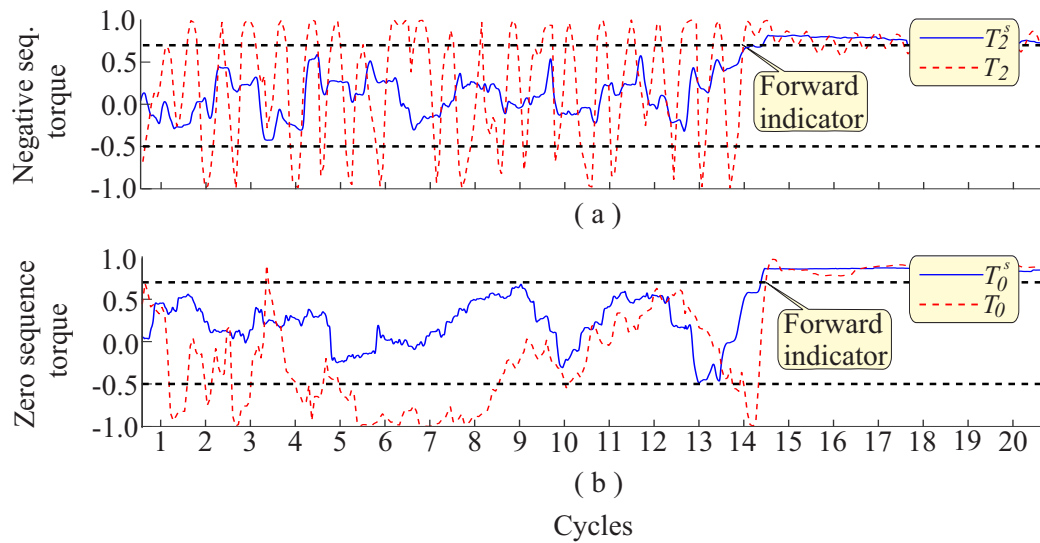


Figure 7.8: Directional protection components sequence units: (a) Directional negative sequence unit; (b) Directional zero sequence unit.

As the normalized conventional directional protection has an oscillatory behavior for the sequence components units, in this work the non-normalized Fourier-based directional protection was utilized as illustrated in Figure 7.9, where  $T_2^*$  is the non-normalized negative torque and  $T_0^*$  is the non-normalized zero torque.

The adopted threshold were  $\gamma_Q^* = 3$  and  $\gamma_N^* = 3$  for the negative and zero sequences, respectively. These threshold were chosen in order to avoid oscillatory region. However, for different systems, different threshold values need be used according to selectivity and coordination studies.

An study was performed considering some forward faults at different inception angles. Table 7.3 illustrates the obtained results showing the percentage of right answers (Hits) and the average time. However, the directional sequence component units can not be compared directly, because in the Fourier algorithm was used the non-normalized torque signals. In the sequence components units, the wavelet-based had the worst time actuation due to the half-cycle compensation in these units, as show Table 5.9. However, as the directional protection flag is a combination of all units (as a logical port 'or'), in some cases, the wavelet phase unit (32W) was faster than the Fourier units. However, in some cases, the Fourier-based method would act faster than the wavelet-based one using the



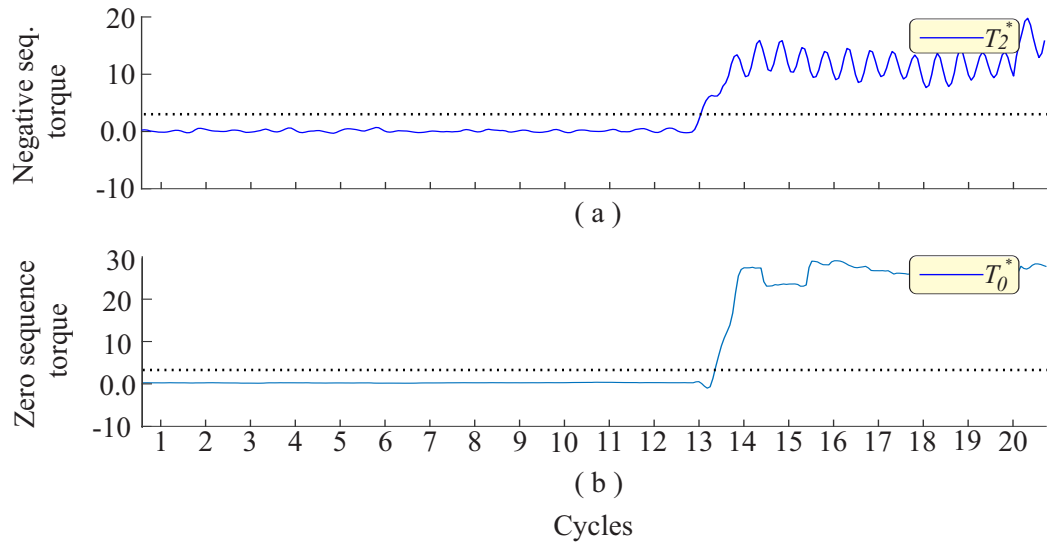


Figure 7.9: Directional protection components sequence units: (a) Directional negative sequence unit; (b) Directional zero sequence unit.

negative sequence unit (32Q).

Table 7.3: Directional protection comparison - Forward faults.

Angles	Operating time [ms]					
	32	32W	32Q	32QW	32N	32NW
27.98°	17.70	7.00	5.20	30.50	8.30	28.50
77.93°	13.50	4.50	5.20	30.50	12.50	33.00
83.59°	13.50	5.50	4.10	33.00	7.20	30.50
122.67°	5.20	3.00	6.20	39.00	6.20	31.00
224.27°	16.60	7.50	5.20	39.00	8.30	29.50
269.98°	14.50	4.00	3.10	49.50	5.20	31.00
277.38°	13.50	5.00	4.10	38.5	7.20	30.50
283.91°	4.10	3.00	9.30	33.50	10.40	31.00
<b>Average</b>	12.32	4.93	5.30	36.68	8.16	30.62
<b>Hits</b>	100%	100%	100%	100%	100%	100%

The positive sequence was analyzed in all the aforementioned cases. However, this unit demonstrates a similar behavior to the phase unit. Therefore, this unit was not depicted in this work.

### 7.3.2 Backward Fault Analyses

Figure 7.10 depicts the directional phase unit wavelet- and Fourier-based protection of a backward SLG fault in phase A. The thresholds adopted for the directional phase unit

to backward faults was  $\tau = -0.5$  in both protection methods. No one directional phase units worked properly to identify a backward fault. Probably, this occurred because the current signal which passes through the sensors was low due to be an external fault (backward) at the PCC and the sensors are configured to forward fault types. Therefore, this directionality unit is not able to be used as a backward detector fault neither a protection strategy. Nevertheless, the protection system is composed by the others directional units, such as that based on negative and the zero sequence components. To the sequence components units, negative and zero, the threshold were  $\tau_Q = -0.5$  and  $\tau_N = -0.5$  for the Fourier- and wavelet-based methods, respectively. These values were chosen in order to avoid false directionality detection.

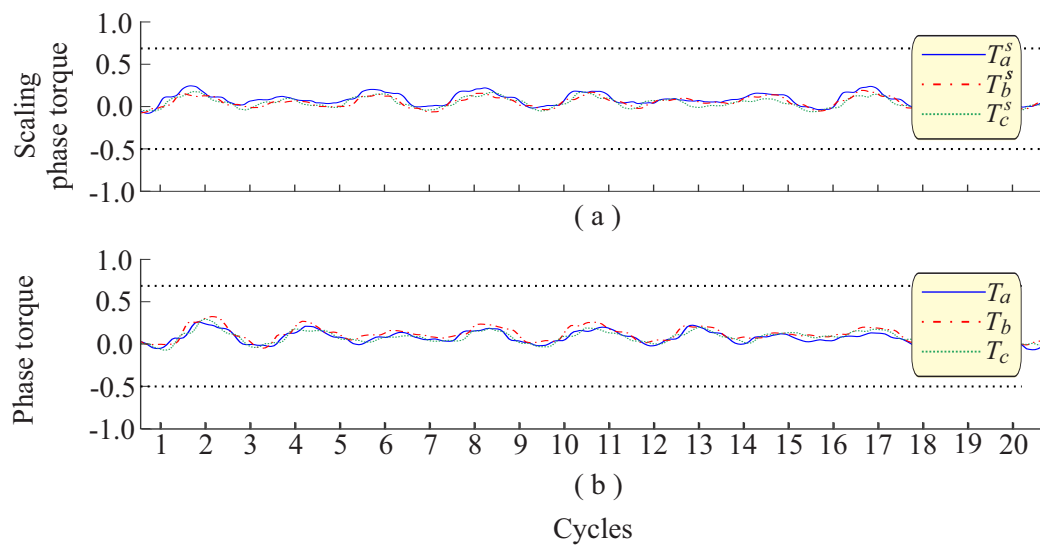


Figure 7.10: Directional protection phase unit - Backward fault: (a) Wavelet-based directional protection, (b) Fourier-based directional protection.

The sequence components were also assessed, as illustrated in Figure 7.11. However, only the zero sequence unit detected correctly the fault occurrence. The zero sequence from the Fourier-based protection was able to detect backward faults similarly to the wavelet-based method. However, when occurs a forward fault, as illustrated in Figure 7.8(b), the Fourier method could identify a false directionality identification, because the signal firstly decreases passing the threshold  $\tau_N$ . Only after a short time interval, the signal starts to converge to the right directionality. Therefore, the wavelet-based method is more stable and do not indicate a false directionality identification. In the steady-state, the directional protection is disabled. Therefore, even the Fourier-based method has been above the up threshold, as depicted in Figure 7.11(b), this is not a problem.

The non-normalized Fourier algorithm was also investigated in order to avoid the false forward fault trip, as illustrated in Figure 7.12. In the cycle 14 (fourteen) from Figure 7.12 the backward fault is recognized. However, a really small threshold is needed, on the order of  $\tau_N = -0.14$ . Nevertheless, this threshold value is impossible to be applied because in forward faults type the signal curve passes through this value before increasing,

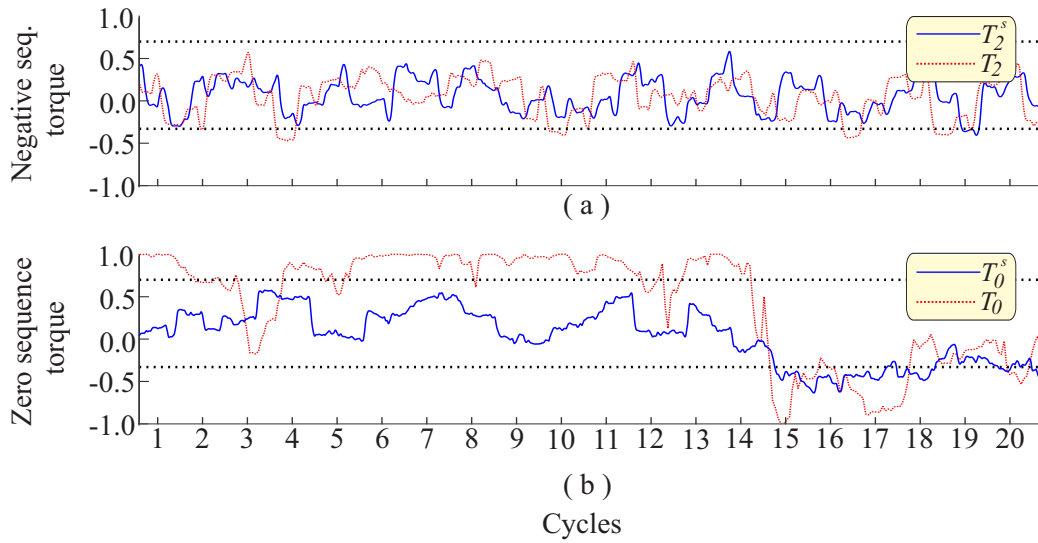


Figure 7.11: Directional protection sequence components unit - Backward fault: (a) Negative sequence unit, (b) Zero sequence unit.

giving also a false directionality identification similarly to the normalized Fourier-method version illustrated in 7.8(b). Therefore, an improved analysis needs to be done in order to identify a threshold reliable to be applied to the Fourier-based method.

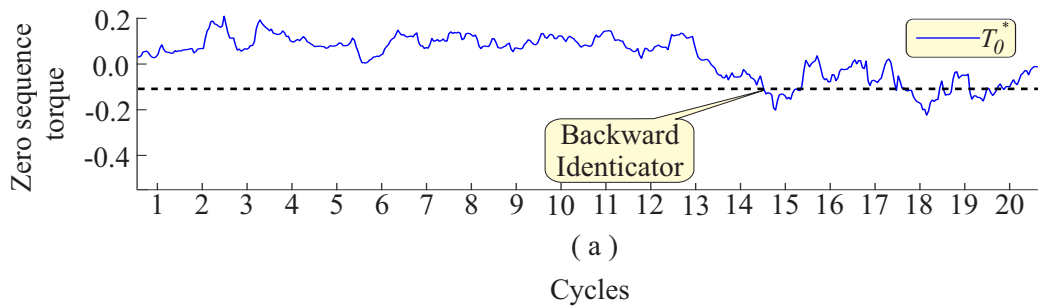


Figure 7.12: Directional protection Zero sequence unit - Fourier algorithm.

Regarding the wavelet transform, the directional wavelet zero sequence unit recognized the fault and achieved a reliable directionality identification to the backward side. This information could be used to trigger the LVRT categories in case of faults at the PCC. Table 7.4 depicts the average time of fault recognition, the percentage of fault recognition from each method, and the correct identification. The 'fault recognition' class means the percentage of electrical fault detected by the zero sequence component in each protection method with a threshold which notifies a false flag to forward faults. In addition, this class was been hard to identify faults with the inception angle near to the zero-crossing voltage. The 'correct identification' class, depicted in Table 7.4, shows the percentage of protection directionality flag achieved by the threshold adopted in this analysis. The

Fourier-based method (unit 32N) is with 0% in this class because the adopted threshold was not sensitized to notify a relay flag. Furthermore, to use another threshold to the backward directional protection was impracticable because a false protection flag would occur. Therefore, a forward fault would be detected as a backward fault with a threshold changing to detect correctly the backward faults.

Table 7.4: Directional protection comparison - Backward faults.

Angles	Operating Times [ms]	
	32N	32NW
27.98°	-	-
77.93°	-	70.00
83.59°	28.12	159.00
122.67°	83.33	97.00
224.27°	67.70	62.00
269.98°	13.54	56.50
277.38°	34.30	22.00
283.91°	11.45	27.00
<b>Average [ms]</b>	39.74	70.50
<b>Fault recognition</b>	75.00%	87.50%
<b>Correct identification</b>	0.00%	75.00%

## 7.4 Analysis of the Differential Protection

Two dynamic cases were examined using experimental data. The first analysis involves an internal SLG fault, whereas in the second one considers an external SLG fault, as illustrated in Figure 6.5. The wavelet-based differential protection applied in this work was proposed by Medeiros and Costa (2018) and de Medeiros (2014) for power transform and this protection was validated only by simulations using the ATP software. Therefore, in this work, this wavelet-based differential protection has been assessed by real experimental data applied in a DFIG topology. The conventional differential protection applied in DFIG was proposed by Mansouri et al. (2016).

### 7.4.1 Internal Fault Analyses

Figure 7.13 illustrates the differential wavelet- and Fourier-based protection of an internal SLG fault in phase A, respectively, where  $\epsilon_d$  is the wavelet operating energy and  $\epsilon_r$  is the wavelet restraint energy, whereas  $I_d$  is the operating current and  $I_r$  is the restraint current. The differential protection is sensitized when the operating current or energy is higher than the restraint current or energy and a predefined threshold. However, only the Fourier-based protection would work properly obeying the two criteria, whereas the wavelet-based differential protection would achieve the correct protection behavior only

with uses the predefined threshold by (5.15) because the operating energy is higher than the restraint energy even in the steady-state.

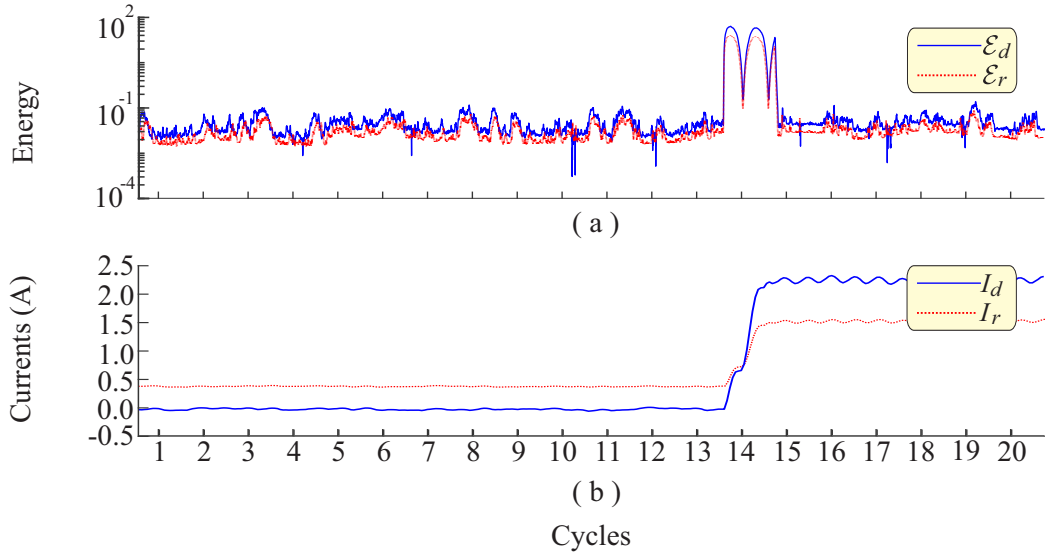


Figure 7.13: Differential protection: (a) wavelet-based; (b) Fourier-based.

This wavelet-based protection problem was already expected because the frequencies of the rotor and stator current signals are different. The Fourier algorithm uses the absolute value estimation, so this frequency difference did not change the final result. However, the wavelet algorithm works in the time-domain. Therefore, the current/energy differential protection principle is broken because the current/energy comparison criteria operate with different current/energy amplitudes in the same time instant. Therefore, one possible solution to this problem is to applying the Park transformation for synchronizing the stator and rotor current vectors. However, disregarding the steady-state and considering an appropriate threshold to the wavelet-based differential protection, this protection would operate properly.

Figure 7.14 illustrates the differential graphic ( $I_r \times I_d$ ) and ( $\epsilon_r \times \epsilon_d$ ) generated by the Fourier and wavelet algorithm, respectively. The  $I_{pickup} = 0.5$  and  $k = 0.7$  were chosen in order to avoid false fault identification. Figure 7.14(a)-(b) illustrates two different areas, the internal fault area and the external fault/steady-state area, in which in the steady-state the signal remains in the correct place, whereas in the fault inception time, the signal passes through the threshold and achieve the fault region.

## 7.4.2 External Fault Analyses

Figure 7.15 illustrates the differential wavelet- and Fourier-based protections for an external SLG fault in phase A, respectively. Figure 7.15(a) illustrates that the wavelet algorithm would not recognize an internal fault in the DFIG because the operating energy is above the restraint energy during all analyzed period. However, Figure 7.15(a) illustrates a signal different behavior during the fault inception time. Furthermore, the operating

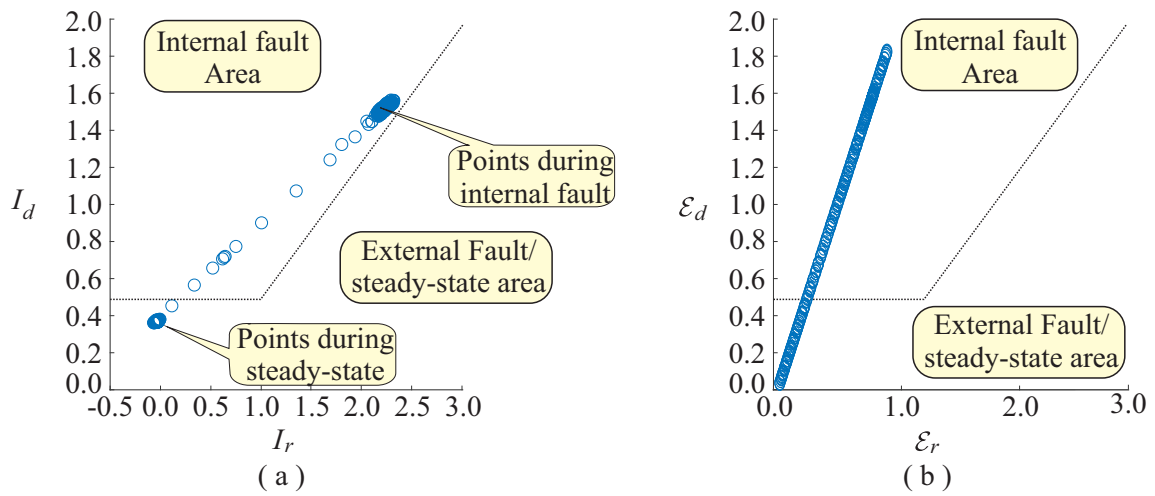


Figure 7.14: Differential graphic - Internal fault: a) Fourier method b) Wavelet method (normalized).

current ( $I_d$ ) illustrated in Figure 7.15(b) increased a small value in the fault inception time (in the fourteen cycle).

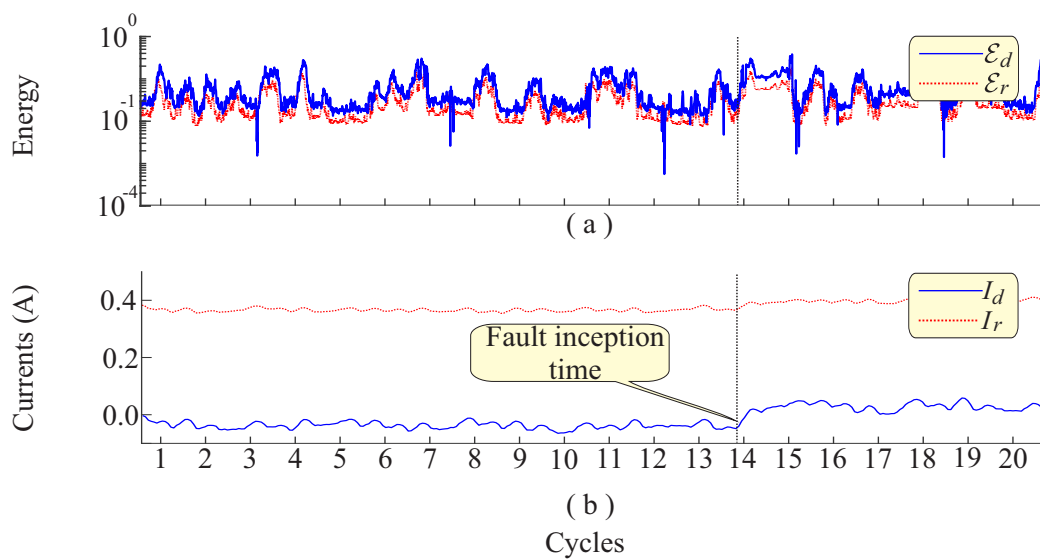


Figure 7.15: Differential protection - External fault: (a) wavelet-based; (b) Fourier-based.

Figure 7.16 depicts the differential graphic from an external fault of the the Fourier- and wavelet-based method. Therefore, both protection differential methods had good behavior without a false trip occurrence. In the future, different cases such as machine saturation, inter-turns faults, and energizing, need to be analyzed by real experimental data and simulations to observe whether will remain this behavior.

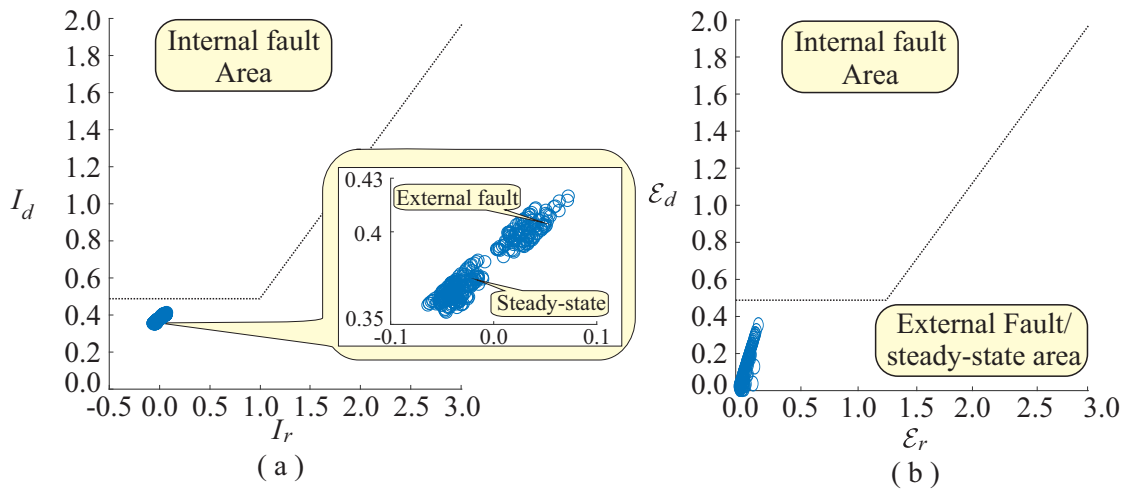


Figure 7.16: Differential graphic - External fault: a) Fourier method b) Wavelet method.

## 7.5 Analysis of the Undervoltage Protection

In this study two dynamic cases were examined for the experimental analyses. The first involves a SLG fault representing a one-phase voltage sag, whereas the second one is a line-to-line fault representing a two-phase voltage sag. Those evaluated voltage sags occurred between the sensors and the PCC as illustrated in Figure 6.6. In addition, internal faults between the sensors and the stator windings connections were also verified. The wavelet-based undervoltage protection applied in this work was based on Costa and Driesen (2013) in which an assessment of the RMS voltage was proposed to be applied in energy quality studies applied in a transmission line and in de Cavalcante Paiva (2015).

This protection has a predefined threshold according to Table 5.6 to the Fourier algorithm and Table 5.7 to the wavelet algorithm.

In contrast to the overcurrent protection, in which the thresholds are chosen according to selectivity and coordination studies, in the undervoltage protection a fixed threshold is established by the norm which is used in this protection scheme. However, in others systems, a selectivity and coordination aspects needs to be considered. In this work, it was not considered these elements because the intention is to validate the new protection in a scenario with different characteristics of the normal ones, such as the DFIG presence.

### 7.5.1 Voltage Sag Analyses

Figure 7.17 depicts a voltage sag at phase A in pu and  $\sqrt{\varepsilon_v^s/\Delta k}$  is the estimation of the voltage amplitude in phase A by the scaling coefficient energy and  $V_a$  is the voltage amplitude in phase A estimated by the Fourier algorithm. In this protection, the wavelet coefficient energy was not used as a trigger signal to the protection act faster because this protection type has a predefined time actuation according to IEEE (2003). Therefore, for a voltage sag equal or higher than 12% the system should act in 2 s, whereas voltage sags upper than 50% the system should act in 0.16 s.

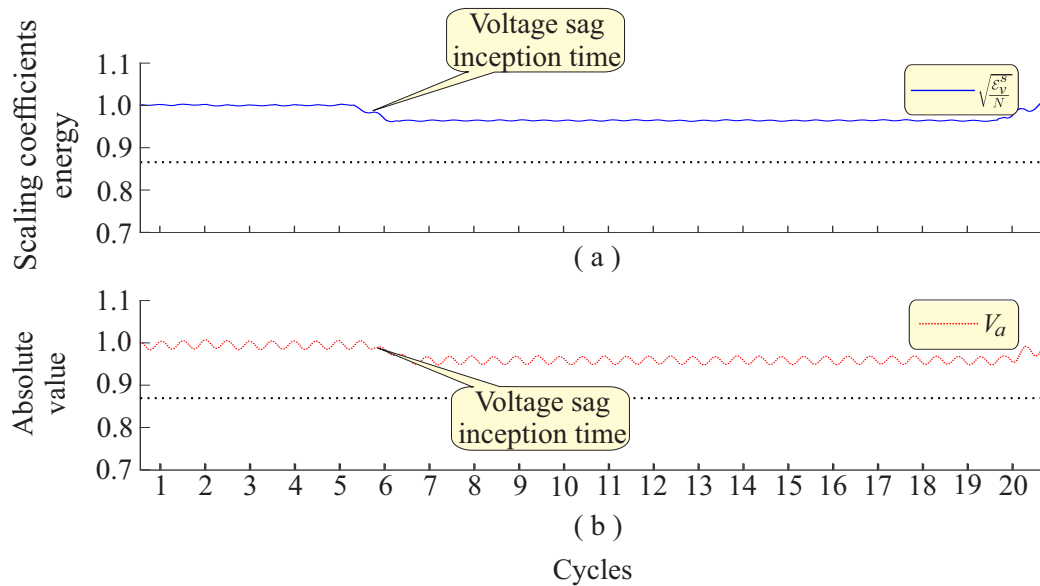


Figure 7.17: Undervoltage protection: (a) wavelet-based; (b) Fourier-based.

Figure 7.17 shows that there is not a fault detection due to severe voltage sag. In order to preserve the elements of the experimental test bench, severe voltage sags were inadequate to be applied in the system. However, the signal behavior illustrates that both algorithms would recognize correctly the start and end point of the voltage sag.

This protection had good behavior in both voltage sag occurrences; when the voltage sag occurs between the PCC and the voltage sensors, and between the voltage sensors and the stator winding connections. In contrast to the measurements made by current sensors where the position of the sensors is extremely important for the different types of faults.

## 7.6 Discussion

After the analysis of the Fourier- and wavelet-based protection notice that for the overcurrent protection both protection methods would work properly for all fault cases verified in this dissertation. However, the wavelet-based algorithm would demonstrate a better time response to detect and act during the faults. Therefore, this behavior is necessary to activate the LVRT categories and protect the generator elements. Notwithstanding, this protection type would not be able to detect faults as internal or external ones.

The undervoltage protection would operate accordingly to the specific regulatory standard. Therefore, a faster sensitization does not affect so much the system behavior, since there is a pre-defined time to this protection actuation. In this sense, both protection would have the same advantages in a general perspective.

Both directional protections would provide good performance. However, in some units, the Fourier-based protection would demonstrate a high oscillatory behavior impairing the correct fault directionality indication, whereas the wavelet-based protection would



achieve a more stable and constant behavior. This protection would be able to detect the backward fault directionality correctly by the zero sequence unit. Therefore, as this fault type is the most common in the electrical system, this unit can be used as a preliminary fault detection method to detect internal and external faults in the DFIG topology. Although, a deeper investigation is needed in order to develop a robust method capable to recognize even faults in the machine windings. Therefore, some scenarios, such as inter-turn, turn-to-turn, and coil-to-coil faults need a directionality investigation in future works. Thus, after this studies, a concrete fault detection method against forward faults would be developed.

The differential wavelet-based protection would work properly when applied to the DFIG assembly when considered a predefined threshold. In addition, the wavelet operating energy ( $\varepsilon_d$ ) would act almost instantly in the fault inception time in Figure 7.13(a). Therefore, this element probably can be used as a fault detector due to its fast response to detect the internal fault events. However, some analysis such as inter-turn, turn-to-turn, coil-to-coil faults, machine saturation, and machine starting need to be done to ensure this feasibility.

## 7.7 Summary

In this chapter, the DFIG variables signals in case of electrical faults were presented and analyzed. Furthermore, analysis using the wavelet-based overcurrent, directional, differential, and undervoltage protections compared with the conventional ones were presented, in order to assess these protections applied in an WECS scenario. Some of these protections are commonly applied in transmission lines, power transformers, and distribution systems. However, in this work was applied in a DFIG, where some of them demonstrates a good performance in this environment.

---

# Chapter 8

## Conclusion

---

### 8.1 General Conclusions

This master dissertation presented the performance analysis of how the wavelet- and Fourier-based overcurrent, directional, differential and undervoltage protections would work in a scenario with a DFIG connected to the power grid. These analyzes were accomplished considering data from an experimental test bench. Some different fault types were analyzed, such as internal and external faults with different voltage inception angles.

Although all challenges present in this system, the analyzed overcurrent protection was correctly sensitized for all cases studied with real experimental data, obtained by a DFIG experimental test-bench, in which the wavelet-based method acts faster than the Fourier-based one for this protection type in all units. This fast sensitization would be useful to protect the machine against internal faults and as an LVRT categories trigger.

Both the wavelet- and conventional-based directional protections would presented a similar behavior in the evaluated scenarios. However, to backward faults, the wavelet-based method would be better to identify the backward faults through the zero sequence component unit. Furthermore, the wavelet-based method demonstrates a lower oscillatory behavior in the sequence components units, which can provide a more reliable directionality detection.

The differential wavelet-based protection, as implemented, would achieve a good performance to detect internal faults whether considered a predefined threshold. In addition, the fault inception time was correctly recognized to all analyzed cases almost instantly but the operating wavelet energy even in the steady state remained above the restraint wavelet energy which would give a false relay trip in a real-time application when the predefined threshold is not considered. The Fourier-based algorithm would achieve the best results. Many challenges still need to be overcome to achieve the expected results for the wavelet-based method, such as the frequency difference of the rotor and the stator windings.

Both the wavelet- and Fourier-based undervoltage protection obtained a similar performance, because this protection uses a pre-defined threshold with a pre-defined time by norm to sensitize the relay. Therefore, the trigger wavelet, which can identify faults almost instantly, is not so expressive when applied in this protection type.

The current literature about this theme shows that there is no standardization to internal protection applied in DFIGs. Therefore, this generator depends on conventional

methods to detect and avoid all internal faults types, which are not reliable enough to give an accurate and efficient protection. In this fashion, the analyzed wavelet-based methods provided indication to be a reliable tool which can identify faults in the stator winding connections faster than the conventional methods. Furthermore, in future, these wavelet-based strategies can be improved to be applied for detect inter-turn and coil-to-coil faults. Therefore, the promising analyzes by using the wavelet transform evidences the feasibility of applying this mathematical tool for the development of specific detection methods for this application.

## 8.2 Future Works

Based on the presented research, the following tasks are proposed to be developed in future works:

1. To apply more varieties of active faults in the DFIG system as well as compare the fault analysis and protections to simulated cases.
2. To propose and implement the wavelet-based overcurrent, directional, differential and undervoltage protection in hardware to be assess in a real experimental DFIG.
3. To integrate all wavelet-based protections to be a complete WECS electrical protection.
4. Development of a wavelet-based internal fault detection method capable to recognize all internal fault types in the rotor and stator windings.
5. Enhancement of the control techniques during faults to achieve the LVRT requirements in conjunction with the protection system.

## 8.3 Publications

At this moment, this research resulted in the following papers:

Table 8.1: Papers resulted from the development of this work.

Event/Journal	Title	Authors
Simpósio Brasileiro de Sistemas Elétricos - SBSE 2018	An experimental test bench for evaluation of techniques to enhance the wind generator integration to the grid*	M. R. Marques, F. E. V. Taveiros, F. B. Costa and L. S. Barros
3rd Workshop on Communication Networks and Power Systems - WCNPS 2018	Assessment of Wavelet-based Directional Overcurrent Protection in a Distribution System with DFIG*	Max Marques, Mônica Leal, Flavio Costa and Luciano Barros
3rd Workshop on Communication Networks and Power Systems - WCNPS 2018	Performance of the Doubly-fed Induction Generator During a Voltage Sag*	Filipe Taveiros, Max Marques, Luciano Barros and Flavio Costa

\* Published.

---

# Bibliography

---

- Abad, Gonzalo, Jesús López, Miguel Rodríguez, Luis Marroyo and Grzegorz Iwanski (2011), *Doubly Fed Induction Machine: Modeling and Control for Wind Energy Generation Applications*, IEEE.  
**URL:** <https://ieeexplore.ieee.org/xpl/articleDetails.jsp?arnumber=6047768>
- Abadi, M. B., S. M. A. Cruz, A. P. Gonçalves, P. F. C. Gonçalves, A. M. S. Mendes, A. Ribeiro and F. Silva (2014), Detection of stator and rotor faults in a dfig based on the stator reactive power analysis, *em* 'IECON 2014 - 40th Annual Conference of the IEEE Industrial Electronics Society', pp. 2037–2043.
- Abdelemam, A. M. M., A. M. El-Rifaie and S. M. Moussa (2017), Discrete wavelet transform based protection for a wind farm double fed induction generator, *em* '2017 IEEE International Conference on Environment and Electrical Engineering and 2017 IEEE Industrial and Commercial Power Systems Europe (EEEIC / I CPS Europe)', pp. 1–6.
- Ackermann, T. (2005), *Wind Power in Power System*, Stockholm, Sweden: John Wiley & Sons Ltd.
- Arun G. Phadke, James S. Thorp (2008), *Synchronized Phasor Measurements and Their Applications*, SIAM.
- BAGE (2017), *Boletim Anual de Geração Eólica 2017*, ABEEólica - Associação Brasileira de Energia Eólica.
- Boutoubat, M., L. Mokrani and A. Zegaoui (2017), Power quality improvement by controlling the grid side converter of a wind system based on a dfig, *em* '2017 6th International Conference on Systems and Control (ICSC)', pp. 360–365.
- Comech, María Paz, Miguel García-Gracia, Susana Martín Arroyo and Miguel Ángel Martínez Guillén (2011), Wind farms and grid codes, *em* G.Krause, ed., 'From Turbine to Wind Farms', IntechOpen, Rijeka, capítulo 2.  
**URL:** <https://doi.org/10.5772/14873>
- Concordia, C., S. B. Crary and G. Kron (1942), 'The doubly fed machine', *Transactions of the American Institute of Electrical Engineers* **61**(5), 286–289.
- Costa, F. B. (2014), 'Fault-induced transient detection based on real-time analysis of the wavelet coefficient energy', *IEEE Transactions on Power Delivery* **29**(1), 140–153.

- Costa, F. B., A. Monti and S. C. Paiva (2017), ‘Overcurrent protection in distribution systems with distributed generation based on the real-time boundary wavelet transform’, *IEEE Transactions on Power Delivery* **32**(1), 462–473.
- Costa, F. B. and J. Driesen (2013), ‘Assessment of voltage sag indices based on scaling and wavelet coefficient energy analysis’, *IEEE Transactions on Power Delivery* **28**(1), 336–346.
- Costa, F.B., B. A. D. Souza and N. S. D. Brito (2010), ‘Detection and classification of transient disturbances in power systems’, *IEEJ Transactions on Power and Energy* **130**, 910–916.
- Dambhare, S., S. A. Soman and M. C. Chandorkar (2009), ‘Adaptive current differential protection schemes for transmission-line protection’, *IEEE Transactions on Power Delivery* **24**(4), 1832–1841.
- Daubechies, Ingrid (1992), *Ten lectures on wavelets. Philadelphia: CBMS-NSF Regional Conference Series*, Springer.
- de Cavalcante Paiva, Sâmara (2015), Proteção em sistemas elétricos com geração distribuída utilizando a transformada wavelet, Dissertação de mestrado, Universidade Federal do Rio Grande do Norte.
- de Medeiros, Rodrigo Prado (2014), Proteção diferencial de transformadores de potência utilizando a transformada wavelet, Dissertação de mestrado, Universidade Federal do Rio Grande do Norte.
- Douglas, H., P. Pillay and P. Barendse (2005), The detection of interturn stator faults in doubly-fed induction generators, *em* ‘Fortieth IAS Annual Meeting. Conference Record of the 2005 Industry Applications Conference, 2005.’, Vol. 2, pp. 1097–1102 Vol. 2.
- Franco, Flavio A. L., Fabio C. N. Caetano, Luan A. Sousa, Renato M. Monaro and Silvio G. Di Santo (2017), Estudo das protecoes de geradores eolicos duplamente alimentados em ambiente de co-simulacao embarcada, *em* ‘The 12th Latin-American Congress on Electricity Generation and Transmission’, pp. 1–6.
- Grossmann, A. and J. Morlet (1984), ‘Decomposition of hardy functions into square integrable wavelets of constant shape’, *SIAM journal on mathematical analysis* **15**(4), 331–371.
- Guo, W., G. Zhang, J. Zhang, N. Song, Z. Gao, X. Xu, L. Jing, Y. Teng, Z. Zhu and L. Xiao (2018), ‘Development of a 1-mva/1-mj superconducting fault current limiter–magnetic energy storage system for lrvt capability enhancement and wind power smoothing’, *IEEE Transactions on Applied Superconductivity* **28**(4), 1–5.
- Guo, W., L. Xiao and S. Dai (2016), ‘Fault current limiter-battery energy storage system for the doubly-fed induction generator: analysis and experimental verification’, *IET Generation, Transmission Distribution* **10**(3), 653–660.

GWS (2017), *Global Wind Statistic 2017*, Global Wind Energy Council.

Haar, Alfred (1910), *Zur Theorie der orthogonalen Funktionensysteme*, *Mathematische Annalen*, Springer.

Hansen, Anca D., Gabriele Michalke, Poul Sørensen, Torsten Lund and Florin Iov (2007), 'Co-ordinated voltage control of dfig wind turbines in uninterrupted operation during grid faults', *Wind Energy* **10**(1), 51–68.

**URL:** <http://https://doi.org/10.1002/we.207>

IEEE (2003), 'Ieee standard for interconnecting distributed resources with electric power systems', *IEEE Std 1547-2003* pp. 1–28.

*IEEE Standard Inverse-Time Characteristic Equations for Overcurrent Relays* (1996), *IEEE Std C37.112-1996* pp. 1–20.

Ioannides, M. G. and J. A. Tegopoulos (1988), 'Optimal efficiency slip-power recovery drive', *IEEE Transactions on Energy Conversion* **3**(2), 342–348.

Ioannidou, M. G. and J. A. Tegopoulos (1987), 'Performance of a doubly-fed induction motor with controlled rotor voltage magnitude and phase angle', *IEEE Transactions on Energy Conversion* **EC-2**(2), 301–307.

Jun-qing, Li, Wang Dong and He Long (2013), Study of rotor winding inter-turn short circuit fault in doubly fed induction generator based on current signal spectrum analysis, *em '2013 International Conference on Electrical Machines and Systems (ICEMS)'*, pp. 789–792.

Junqing, Li, He Long and Wang Dong (2013), Rotor winding inter-turn fault analysis of doubly-fed induction generator based on negative sequence component, *em '2013 International Conference on Electrical Machines and Systems (ICEMS)'*, pp. 785–788.

Justo, Jackson John, Francis Mwasilu and Jin-Woo Jung (2015), 'Doubly-fed induction generator based wind turbines: A comprehensive review of fault ride-through strategies', *Renewable and Sustainable Energy Reviews* **45**, 447 – 467.

**URL:** <http://www.sciencedirect.com/science/article/pii/S136403211500074X>

Kang, Y. C., H. G. Kang, J. H. Lee, T. Y. Zheng, B. E. Lee and G. C. Park (2009), Protection algorithm for the windings of a doubly-fed induction generator using the d-q equivalent circuits, *em '2009 Transmission Distribution Conference Exposition: Asia and Pacific'*, pp. 1–4.

Kasztenny, Bogdan, Dave Sharples, Bruce Campbell and Marzio Pozzuoli (2000), Fast ground directional overcurrent protection—limitations and solutions, *em 'Proceedings of the 27th Annual Western Protective Relay Conference'*, pp. 24–26.

- Kia, M. Y., M. Khedri, H. R. Najafi and M. A. Shamsi Nejad (2013), 'Hybrid modelling of doubly fed induction generators with inter-turn stator fault and its detection method using wavelet analysis', *IET Generation, Transmission Distribution* **7**(9), 982–990.
- Leal, Mônica Maria, Flavio Bezerra Costa and João Tiago Loureiro Sousa Campos (2019), 'Improved traditional directional protection by using the stationary wavelet transform', *International Journal of Electrical Power and Energy Systems* **105**, 59 – 69.
- Li, H. and Z. Chen (2008), 'Overview of different wind generator systems and their comparisons', *IET Renewable Power Generation* **2**(2), 123–138.
- Liwschitz, M. M. (1941), 'Damping and synchronizing torque of the double-fed asynchronous machine', *Transactions of the American Institute of Electrical Engineers* **60**(10), 923–924.
- Mallat, S. G. (1989), 'A theory for multiresolution signal decomposition: the wavelet representation', *IEEE Transactions on Pattern Analysis and Machine Intelligence* **11**(7), 674–693.
- Mansouri, M. Mahdi, Majid Nayeripour and Michael Negnevitsky (2016), Internal electrical protection of wind turbine with doubly fed induction generator, *em 'Renewable and Sustainable Energy Reviews'*, Vol. 55, pp. 840 – 855.
- Marques, M. R., F. E. V. Taveiros, F. B. Costa and L. S. Barros (2018), An experimental test bench for evaluation of techniques to enhance the wind generator integration to the grid, *em '2018 Simposio Brasileiro de Sistemas Eletricos (SBSE)'*, pp. 1–6.
- Medeiros, R. P. and F. B. Costa (2018), 'A wavelet-based transformer differential protection: Internal fault detection during inrush conditions', *IEEE Transactions on Power Delivery* pp. 1–1.
- Muller, S., M. Deicke and R. W. De Doncker (2002), 'Doubly fed induction generator systems for wind turbines', *IEEE Industry Applications Magazine* **8**(3), 26–33.
- Noureldeen, O. and I. Hamdan (2017), An efficient anfis crowbar protection for dfig wind turbines during faults, *em '2017 Nineteenth International Middle East Power Systems Conference (MEPCON)'*, pp. 263–269.
- Okedu, K. E. (2016), 'Enhancing dfig wind turbine during three-phase fault using parallel interleaved converters and dynamic resistor', *IET Renewable Power Generation* **10**(8), 1211–1219.
- Okedu, K. E., S. M. Muyeen, R. Takahashi and J. Tamura (2012), 'Wind farms fault ride through using dfig with new protection scheme', *IEEE Transactions on Sustainable Energy* **3**(2), 242–254.

- Pena, R., J. C. Clare and G. M. Asher (1996), 'Doubly fed induction generator using back-to-back pwm converters and its application to variable-speed wind-energy generation', *IEE Proceedings - Electric Power Applications* **143**(3), 231–241.
- Percival, Donald B. and Andrew T. Walden (2000), *Wavelet Methods for Time Series Analysis*, Cambridge Series in Statistical and Probabilistic Mathematics, Cambridge University Press.
- Polikar, Robi (1996), *The wavelet tutorial*, Rowan University.
- Popa, L. M., B. B. Jensen, E. Ritchie and I. Boldea (2003), Condition monitoring of wind generators, *em '38th IAS Annual Meeting on Conference Record of the Industry Applications Conference, 2003.'*, Vol. 3, pp. 1839–1846 vol.3.
- Quéval, L. and H. Ohsaki (2012), Back-to-back converter design and control for synchronous generator-based wind turbines, *em '2012 International Conference on Renewable Energy Research and Applications (ICRERA)'*, pp. 1–6.
- Rahim, A. H. M. A. (1988), 'Stabilizing controls for a doubly fed synchronous-induction machine', *IEEE Transactions on Energy Conversion* **3**(4), 799–805.
- Roberts, Jeff and Armando Guzman (1994), Directional element design and evaluation.
- Roshanfekar, R. and A. Jalilian (2016), 'Wavelet-based index to discriminate between minor inter-turn short-circuit and resistive asymmetrical faults in stator windings of doubly fed induction generators: a simulation study', *IET Generation, Transmission Distribution* **10**(2), 374–381.
- Serrano-González, Javier and Roberto Lacal-Aránzategui (2016), 'Technological evolution of onshore wind turbines—a market-based analysis', *Wind Energy* **19**(12), 2171–2187.  
**URL:** <https://onlinelibrary.wiley.com/doi/abs/10.1002/we.1974>
- Shah, D., S. Nandi and P. Neti (2009), 'Stator-interturn-fault detection of doubly fed induction generators using rotor-current and search-coil-voltage signature analysis', *IEEE Transactions on Industry Applications* **45**(5), 1831–1842.
- Shen, Y., D. Ke, W. Qiao, Y. Sun, D. S. Kirschen and C. Wei (2015), 'Transient reconfiguration and coordinated control for power converters to enhance the lVRT of a DFIG wind turbine with an energy storage device', *IEEE Transactions on Energy Conversion* **30**(4), 1679–1690.
- Stefani, A., A. Yazidi, C. Rossi, F. Filippetti, D. Casadei and G. Capolino (2008), 'Doubly fed induction machines diagnosis based on signature analysis of rotor modulating signals', *IEEE Transactions on Industry Applications* **44**(6), 1711–1721.
- Stojčić, G., K. Pašanbegović and T. M. Wolbank (2014), 'Detecting faults in doubly fed induction generator by rotor side transient current measurement', *IEEE Transactions on Industry Applications* **50**(5), 3494–3502.



- Taveiros, F. E. V., L. S. Barros and F. Bezerra Costa (2013), Wind turbine torque-speed feature emulator using a dc motor, *em* '2013 Brazilian Power Electronics Conference', pp. 480–486.
- Taveiros, Filipe Emanuel Vieira (2014), Sistema de conversão de energia eólica baseado no gerador de indução duplamente alimentado: análise e contribuição ao controle da máquina, Dissertação de mestrado, Universidade Federal do Rio Grande do Norte.
- Taveiros, Filipe Emanuel Vieira (2018), A Novel Control Structure to Enhance the DFIG-based Wind Energy Conversion System Integration to the Grid, Tese de doutorado, Universidade Federal do Rio Grande do Norte.
- Tremblay, E., A. Chandra and P. J. Lagace (2006), Grid-side converter control of dfig wind turbines to enhance power quality of distribution network, *em* '2006 IEEE Power Engineering Society General Meeting', pp. 6 pp.–.
- Vrionis, T. D., X. I. Koutiva and N. A. Vovos (2014), 'A genetic algorithm-based low voltage ride-through control strategy for grid connected doubly fed induction wind generators', *IEEE Transactions on Power Systems* **29**(3), 1325–1334.
- Wu, Bin, Yongqiang Lang, Navid Zargari and Samir Kouro (2011), *Power Conversion and Control of Wind Energy Systems*, IEEE.  
**URL:** <https://ieeexplore.ieee.org/xpl/articleDetails.jsp?arnumber=6047690>
- Xiao, X., R. Yang, X. Chen and Z. Zheng (2018), 'Integrated dfig protection with a modified smes-fcl under symmetrical and asymmetrical faults', *IEEE Transactions on Applied Superconductivity* **28**(4), 1–6.
- Yaramasu, V., B. Wu, P. C. Sen, S. Kouro and M. Narimani (2015), 'High-power wind energy conversion systems: State-of-the-art and emerging technologies', *Proceedings of the IEEE* **103**(5), 740–788.
- Yazdani, A. and R. Iravani (2006), 'A neutral-point clamped converter system for direct-drive variable-speed wind power unit', *IEEE Transactions on Energy Conversion* **21**(2), 596–607.
- Zarei, M. E., C. A. Platero, C. Vezanzones and J. R. Arribas (2018), New differential protection for variable speed doubly fed induction machines, *em* '2018 XIII International Conference on Electrical Machines (ICEM)', pp. 1906–1911.
- Zou, Z., X. Xiao, Y. Liu, Y. Zhang and Y. Wang (2016), 'Integrated protection of dfig-based wind turbine with a resistive-type sfcl under symmetrical and asymmetrical faults', *IEEE Transactions on Applied Superconductivity* **26**(7), 1–5.

---

# Appendix A

## Experimental Test-bench

---

### A.1 The Experimental Test-Bench

Figure A.1 illustrates the DFIG experimental test-bench used to obtain real data to the analysis of DFIG signals, which is essential for the development of new protection and control strategies capable to enhance the DFIG employment in wind farms. This experimental test bench was developed in Taveiros (2018).

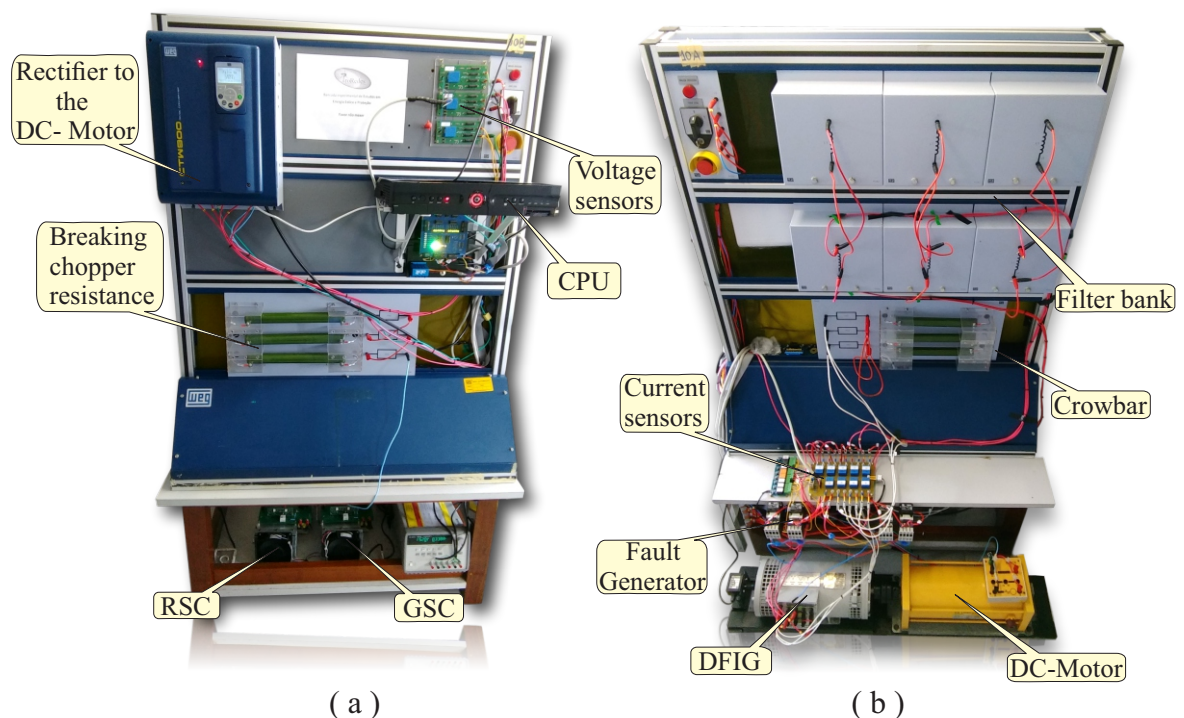


Figure A.1: Experimental test bench: (a) Front; (b) Back.

The real DFIG parameters are specified in Table A.1, which are the main variables used to design the system controls and perform the model simulations with a DFIG topology.

Table A.1: Experimental DFIG Parameters.

Parameters	Value	Description
$V_s$	220 [V]	Stator voltage
$P_n$	1.5 [kW]	Rated Power
$f$	60 [Hz]	Electrical frequency
$p$	2	Pole pairs
$W_n$	1800[rpm]	Synchronous speed
$R_s$	0.993[Ω]	Stator resistance
$R_r$	0.877[Ω]	Rotor resistance
$L_{s\sigma}$	0.00286[H]	Stator leakage inductance
$L_{r\sigma}$	0.00697[H]	Rotor leakage inductance
$L_m$	0.0863[H]	Magnetizing inductance
$J$	0.0265 [V]	Inertia
$C$	470 [μC]	DC-link capacitor
$R_f$	0.4 [Ω]	Filter resistance
$L_f$	75 [mH]	Filter inductance
$n$	3.0	Turns ratio

The experimental test bench is implemented with a DFIG, a back-to-back power converter, a power rectifier, electric contactors, a DC-motor coupled to the generator used to emulate the wind by a hardware-in-the-loop (HIL) wind turbine emulator system (Taveiros et al. 2013) (Marques et al. 2018). Furthermore, the scheme for the maximum power point tracking (MPPT) used in the test bench was based on the ideal torque control because it does not need the anemometer and the torque can be controlled directly by the quadrature axis rotor current.

The component called CPU in Figure A.1(a) has all the processing units of the system, which is controlled by the Single-board Reconfigurable Input-Output (sb-RIO) system from National Instruments. In addition, there is the wind turbine model with the wind characteristics and the MPPT embedded in an FPGA as well. There is the fault-generator unit responsible for the external and internal faults application. Furthermore, the GSC and the RSC that compose the back-to-back converter are controlled by the conventional PI cascade control in ‘dq’ reference frame.

Figure A.1(b) illustrates the DC motor which emulates the wind characteristic behavior controlled by a thyristor rectifier, as proposed in Taveiros et al. (2013). Furthermore, some important elements, such as the crowbar, current sensors, filter bank and the fault generator are also depicted. The disturbances generated by the fault generator are made employing a load of  $r_f = 15 \Omega$  to one or more phases of the machine connection points.

Figure A.2 shows the electric diagram and the CPU component of the experimental test bench. Figure A.2(a) illustrates the CPU unit with all processing components, which are the RSC control, GSC control, MPPT characteristics and the wind turbine model, all implemented in the Sb-RIO. However, the DC motor control is implemented in the rectifier CTW 900 WEG. Figure A.2(b) shows the electric diagram of the experimental

test bench.

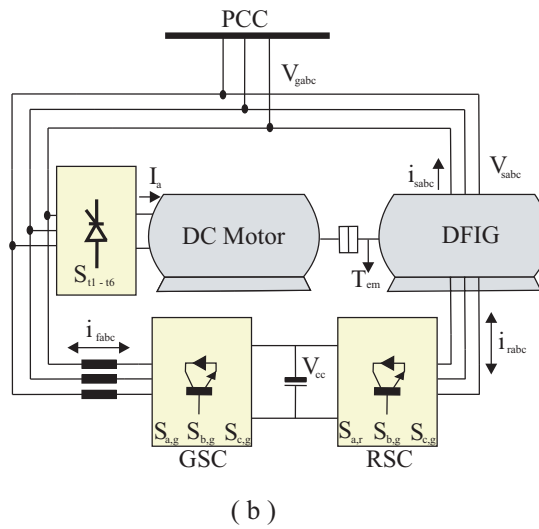
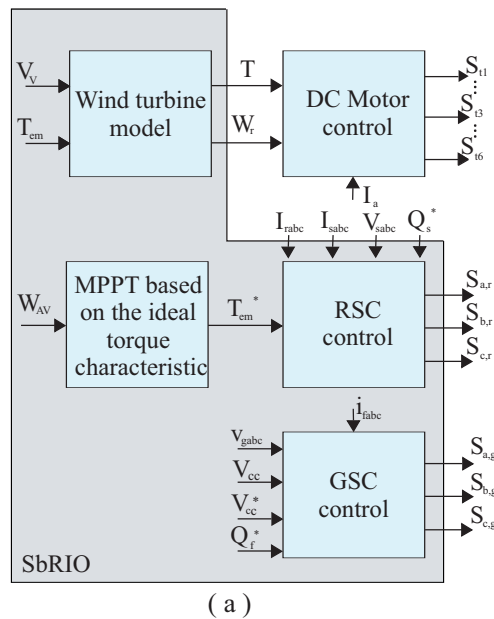


Figure A.2: Experimental test bench: (a) CPU unit; (b) Electrical diagram (Adapted from Marques et al. (2018)).

There is a supervisory system used to connect the software with the hardware devices, which was implemented at the labview software in the G programming language. On this interface, it is possible to set manually or automatically the machine and the control parameters, as well as capture and plot the transducer signals in real time, making it a user-friendly interface.

All DFIG signals data are able to be exported to the Matlab software. Therefore, all signals collected can be processed in offline mode for different studies, which makes it possible to process signals without the need to operate the system simultaneously because

all data has already been stored in a database. Moreover, the system interface commands the online application of electrical faults.

The support for faults and voltage sags has been gaining a lot of attention nowadays because there is an increasing number of WECS connected to the electrical grid. Therefore, one of the most main requirements imposed by the system operators is the ability of wind turbines to remain connected to the grid in cases of disturbances. In order to meet this requirement, the experimental test bench emulates some electrical disturbances, for instance, single-line, line-to-line faults or open-circuit events. Moreover, voltage sags are able to be simulated. This tool is indispensable for conducting analyzes and studies about innovative control, fault detection, and protection methods capable of allowing the generator to remain connected or not to the grid at the moment of electrical disturbances.